Three-Dimensional Radiative Transfer Modeling of Tropospheric Atmospheres

By

David H. Tofsted
Sean G. O'Brien

Computational and Informational Sciences Directorate
Battlefield Environment Division

REPORT DOCUMENTATION PAGE

Public reporting burden for this collection of information is estimated to average 1 hour per response, including the time for reviewing instructions, searching existing data sources, gathering and maintaining the data needed, and completing and reviewing the collection of information. Send comments regarding this burden estimate or any other aspect of this collection of information, including suggestions for reducing the burden, to Washington Headquarters Services, Directorate for information Operations and reports, 1215 Jefferson Davis Highway, Suite 1204, Arlington, VA 22202-4302 and to the Office of Management and Budget, Paperwork Reduction Project (0704-0188), Washington, DC 20503.

1. AGENCY USE ONLY (*Leave Blank*)	2. REPORT DATE March 1998	3. REPORT TYPE AND DATES COVERED Final	

4. TITLE AND SUBTITLE
Three-Dimensional Radiative Transfer Modeling of Tropospheric Atmospheres

5. FUNDING NUMBERS

6. AUTHOR(S)

David Tofsted
Sean O'Brien

7. PERFORMING ORGANIZATION NAME(S) AND ADDRESS(ES)

U.S. Army Research Laboratory
Computational & Information Sciences Directorate
Battlefield Environment Division
ATTN: AMSRL-IS-EW
White Sands Missile Range, NM 88002-5501

8. PERFORMING ORGANIZATION REPORT NUMBER

ARL-TR-1629

9. SPONSORING/MONITORING AGENCY NAME(S) AND ADDRESS(ES)

U.S. Army Research Laboratory
2800 Powder Mill Road
Adelphi, MD 20783-1145

10. SPONSORING/MONITORING AGENCY REPORT NUMBER

ARL-TR-1629

11. SUPPLEMENTARY NOTES

12a. DISTRIBUTION/AVAILABILITY STATEMENT

Approved for public release; distribution unlimited.

12b. DISTRIBUTION CODE

A

13. ABSTRACT (Maximum 200 words)

Physically accurate visualizations of tropospheric atmospheres require three-dimensional radiative transfer (RT) codes capable of simulating scattering and absorption effects in and around natural clouds. This report describes an adaptation of the discrete ordinates technique for handling both thin (haze) and thick (natural cloud) optical media in a consistent manner.

Media are modeled via uniform density cubical scattering cells assuming that incident diffuse streams have uniform radiance over each input face. These assumptions allow the analytic evaluation of transmission factors and volume-averaged unscattered illumination across a cell in evaluating scattered streaming energies at each cell exit face. This initial analysis leads to an energy accounting technique which replaces energy not accounted for via transmission and diffuse single scattering with a surface scattering effect. Solar/lunar direct irradiance and gray-body radiation are also considered.

Monte Carlo analyses were used to determine the accuracy of the proposed methods. Path point-to-point calculations are described that adapt the outputs of the RT code to provide limiting path radiance information for visualization purposes. Extensions of the point-to-point technique allow for visualization of cloud fields. An analysis of the scattering properties of aerosols as scale transformed Legendre polynomial expansions is also provided.

14. SUBJECT TERMS

radiative transfer, transmission, scattering

15. NUMBER OF PAGES
133

16. PRICE CODE

17. SECURITY CLASSIFICATION OF THIS REPORT UNCLASSIFIED	18. SECURITY CLASSIFICATION OF THIS PAGE UNCLASSIFIED	19. SECURITY CLASSIFICATION OF ABSTRACT UNCLASSIFIED	20. LIMITATION OF ABSTRACT SAR

Preface

The modeling of atmospheric illumination and radiance as it affects Army systems has had a long and curious history. One of the main aspects of this area has been the lack of progress in solving some of the main difficulties in assessing the influence of clouds and hazes in complex geometries. The example of the man hunting for keys beneath the street lamp comes to mind. He searched where there was light, but his keys were lost someplace else. Often in the atmospheric sciences we can fall victim to this temptation because the difficulty of some real problems is beyond current theory and applications.

In this case, however, we believe that some light has been shed on the area of three-dimensional modeling of radiances in cloud fields. And while this may sound esoteric, the issue should be of major concern to the Army community. A large fraction of Army systems rely on direct line of sight (LOS) optics for engaging, detecting, and/or tracking enemy activity. And since the Army frequently operates beneath a cloud deck, it is highly likely that clouds will impact the performance of Army systems. In particular, illumination effects modify the ability of an observer to detect a target against a natural background. Also, in the past the illumination and optical properties along lines of sight had been treated as uniform, or, in the best models, assumed to have simple scaling laws for use in slant-path evaluation techniques. But, in three-dimensional modeling, the radiance field changes with position and direction requiring path dependent LOS calculations. This allows what-if questions to be asked concerning into-sun/out-of-the-sun scenarios and the evaluation of cloud shadowing effects. Solar illumination also affects the energy loading of surfaces for thermal signature calculations.

The Atmospheric Illumination Module (AIM) codes are designed to permit analysis of surface illumination and volumetric radiance calculations within a scattering/absorbing/emitting atmosphere beginning at the Earth's surface and extending upward through the cloud-filled portion of the troposphere. The principal features of this set of models consist of a three-dimensional radiative transfer model capable of treating thin to extremely thick media, a modeling methodology for representing the Legendre expansion of the aerosol scattering properties of cloud aerosols and hazes, and a visualization model for depicting the appearances of clouds.

It is hoped the visualization model discussed herein will some day lead to the real time use of the data sets produced by AIM in simulations of various systems.

Acknowledgements

Contents

Figures

Tables

Executive Summary

Introduction

The Atmospheric Illumination Module (`AIM`) is designed to facilitate the assessment of radiance in the atmosphere (surface through 4, 8, or 12 km). Numerous Army systems employ passive electro-optical devices designed to detect and acquire objects in their image fields, both those directly illuminated (visible) and those detectable through indirect effects due to solar loading. But the atmosphere affects the appearance of viewed scenes both through spatial and spectral modifications of the illumination pattern and through path transmission and radiance modifications of the scene energy. In this series of codes, we currently provide a means of visualizing and quantifying the effects of the atmosphere at visible wavelengths.

Background

The primary impact of the atmosphere on target acquisition in the visible band is contrast transmission. This depends on both the density of the medium (affecting transmittance) and the influence of illumination on atmospheric constituents (affecting path radiance). The general expression

$$C = \frac{C_0}{1 + S_g(T^{-1} - 1)} \tag{1}$$

is often used, where C is the transmitted contrast, C_0 is the initial contrast at zero range, S_g is the sky-to-ground ratio, and T is the transmission. $T = \exp(-\sigma R)$, where σ is the wavelength-dependent extinction coefficient and R is the range to target. The sky-to-ground ratio is the ratio of the limiting path radiance (often judged based on the brightness of the horizon sky) to the brightness of the background terrain near the target.

While there are numerous complications that apply when using this equation, as discussed in the main text, the primary point is that limiting path radiance, terrain brightness, and an extinction coefficient are necessary for any analysis of atmospheric effects. Providing these quantities is the motivation behind the `AIM` models.

Overview

The body of this report explains the methods developed for producing the volumetric radiances necessary to assess sky and terrain brightnesses. We consider the means of generating suitable model inputs by converting liquid water content information provided by the Air Force's Cloud Scene Simulation Model (CSSM) into extinction coefficient and scattering property data required by the radiative transfer (RT) model.

Assessing brightness entails the RT modeling of a simulated atmospheric volume in contact with the Earth's surface and extending several kilometers vertically to incorporate typical cloud layers for surface shadow calculation purposes. The scenario volume is extended horizontally to treat a volume large enough to be significant for line of sight (LOS) engagements (around 8×8 km^2).

The RT model developed here features techniques for treating dense clouds within a Discrete Ordinates Method (DOM) paradigm. This is accomplished by altering the traditional DOM technique. The traditional technique emphasizes cell-centered calculations and extrapolations to cell-wall values. The modified technique determines cell-wall-averaged radiances and extrapolates results to cell-volume-averaged radiances for purposes of calculating volumetric diffuse scattering effects. After these volume-based methods were developed, analysis showed that energy was being lost due to the single-scattering assumption. To compensate, a surface-based scattering event has been introduced, based on a volumetric energy accounting calculation. Validations of the RT code have been accomplished through comparison with Monte Carlo scenario results. These comparisons involved developing a series of three-dimensional scattering cases, which in one limit matched existing literature results for uniform density cubical volumes.

Following development of the RT technique, we consider the usages of these results in LOS effects computations, visualization codes, and compact formats useful for network distribution of data. In the appendix we show the means of representing aerosol scattering properties within the Legendre expansion framework applicable to the DOM.

Conclusions

Methods used in developing radiance mappings and visualization techniques for the near-surface atmosphere for the visible band are described. The RT model developed is shown to predict model fluxes with 0.999 correlation to the Monte Carlo cases run. The visualization code developed is shown to produce realistic images that are also quantitatively correct. We believe these models represent the state of the art in physics-based radiance modeling of the boundary layer atmosphere.

1. Introduction

The performance of any electro-optical imaging system depends on the medium through which signals are received. As optical systems are continually being upgraded for special purposes, it is reasonable to augment system design by studying the impact of environment on system performance. One means of studying this problem is to simulate the system along with its environment in such a way that system-controlling parameters can be modified and tested against a variety of adverse situations. The optimal performance can then be determined as that combination of parameters providing the best functionality under the conditions tested.

1.1 Target Acquisition Considerations

From a systems viewpoint, the primary effect of the atmosphere is the loss of contrast between a target and its background. An Army adage says, "if it can be seen it can be killed." But what does it mean for something to be seen using a visible waveband system?

Middleton (1952) presented the classic study indicating the human vision system has a limiting contrast threshold of approximately 2 percent under daylight conditions. Contrast is usually defined as

$$C(R) = \frac{L_T(R) - L_B(R)}{L_B(R)}, \tag{2}$$

where C is the contrast and L_T and L_B are the propagated brightnesses (radiances) of the target (object) and its background, all at range R. When $C(R)$ falls below 0.02, the object becomes indistinguishable from its background to a human observer.

Standard analysis of Eq. (2) involves defining C_0 as the contrast at zero range and σ as the wavelength-dependent extinction coefficient (assumed constant over the optical path to the observer). The initial radiance of the target is reduced by scattering and absorption along the optical path by a factor $T(R) = \exp(-\sigma R)$ called the transmittance. In addition, a quantity $(L_P(R))$ known as the path radiance (scattering and emission of energy into the LOS) is added to both the attenuated target and background radiances:

$$L_T(R) = T(R)L_T(0) + L_P(R); \qquad L_B(R) = T(R)L_B(0) + L_P(R). \tag{3}$$

In the traditional analysis, the path radiance is related to the quantity called the limiting path radiance or sky radiance (L_L), which is the radiance produced if one could look through an infinitely long atmosphere in a given direction. The relationship between the path radiance and the limiting path radiance is:

$$L_P(R) = L_L\left[1 - T(R)\right]. \tag{4}$$

Introducing Eqs. (2) and (3) into (1), we obtain the form,

$$C(R) = \frac{T(R)[L_T(0) - L_B(0)]}{T(R)L_B(0) + L_L\left[1 - T(R)\right]}. \tag{5}$$

Dividing numerator and denominator by $T(R)L_B(0)$, and using the terms sky-to-ground ratio ($S_g = L_L/L_B(0)$) and inherent contrast ($C_0 = [L_T(0) - L_B(0)]/L_B(0)$), one obtains,

$$C(R) = \frac{C_0}{1 + S_g(T(R)^{-1} - 1)}, \tag{6}$$

which is the contrast transmission equation. This equation has important consequences in assessing atmospheric effects on target acquisition and thus has been incorporated into numerous combat simulations. The influence of transmittance is obvious. The influence of sky-to-ground ratio is less direct, but not negligible. Lee and LaMotte (1991) have shown how variations in S_g influence the loss exchange ratios in combat simulations.

But there are several difficulties in the use of this simple expression in describing the effects of the atmosphere. First, C_0 is by no means 'inherent' in the sense that it is an invariant property of a given target against a given background. The appearance of an object against its background will depend on the available direct (solar/lunar) and diffuse illumination's interactions with an object or background's bi-directional reflectance distribution function (BRDF) (Davis (1987); Weiss and Scoggins (1987)), or even its facetized representation in more complex modeling schemes. These characteristics may also be spectrally (color) dependent (e. g., Gerhart *et al.* (1995)).

Second, transmittance is not a simple function of range. Slant path geometries through the atmosphere can involve vertically variable extinction coefficients through haze (Fiegel 1994) or fully three-dimensional (3D) variability when considering clouds.

Third, the sky brightness or limiting path radiance is a function of not only position and wavelength but also of look direction (Davis 1986) due to non-isotropic scattering. Further, dense volume segments will create dark and bright shadow regions in the volume, invalidating the simple form for the path radiance calculation. To properly evaluate a radiative environment, then, one needs a fully 3D spectral/directional model.

1.2 The Modeling Environment

These same observations are made in various studies (Welch and Wielicki (1984); Kobayashi (1991); Haferman *et al.* (1993); Li *et al.* (1994); Byrne *et al.* (1996)) which consider the ambient radiances present within the tropospheric atmosphere and atmospheric layer reflectivities of partly cloudy atmospheres. These studies concluded that one cannot adequately model partly cloudy skies using plane-parallel atmospheric models, where typically partly cloudy results are interpolated from results of overcast and clear-sky cases. These studies thus infer the implicit weaknesses of plane-parallel models to determine target acquisition capabilities within the Earth's cloud-filled atmosphere. Yet plane-parallel models still have numerous applications. For example, plane-parallel radiative transfer treatments heavily influence considerations of vertical remote sensing through cloud free atmospheres (Nakajima and Tanaka 1988) and high accuracy one-dimensional (1D) radiative transfer (RT) codes (Stamnes and Swanson (1981); Stamnes *et al.* (1988)) have been developed expressly for analysis of these problems.

While 1D-RT codes are clearly valuable for certain applications, robust analysis of systems performance within a realistic earth atmosphere requires a 3D-RT code. Of the numerous 3D-RT techniques described in the literature, several are generally recognized, including Fourier methods, analytical models, diffusion approximation models, Monte Carlo models, and Discrete Ordinates Methods (DOM) models. Fourier method studies are typified by Priesendorfer and Stephens (1984), Stephens (1986, 1988), Kobayashi (1991), and Li *et al.* (1994b). Analytical methods have been developed by Davies (1978), used by van de Hulst (1980a, 1980b), and developed for special cases more recently by Li *et al.* (1994a). Diffusion methods were pursued by Gube *et al.* (1980) and Zardecki *et al.* (1986). Monte Carlo methods were used by McKee and Cox (1974) and Welch and Wielicki (1984). Yet another approach involves the small-angle-approximation (SAA). This method is often used to study systems effects due to forward scattering of aerosols. But, we are considering only general illumination and visualization of scenes and the resulting dynamic range effects. In effect, we are ignoring the forward scatter problem, which is a separate topic, and thus will ignore the SAA approach here.

For this work we have selected the discrete-ordinates technique as the most appropriate vehicle. This focus is prompted by several factors. First, diffusion methods are inherently limited to relatively isotropically scattering media. Moreover, this media must be optically thick and have extinction effects that are dominated by scattering. The atmosphere viewed by sensors does not fit this description in general; while diffusion processes may dominate in extremely thick regions (clouds) of the atmosphere, they have no applicability to non-cloud regions. But, any general model must be able to treat both thin and thick regions.

Monte Carlo techniques are currently impractical, or at best unwieldy, given current limited computer resources. In order to characterize paths through the volume, one must produce a radiance picture of the whole volume, and Monte Carlo methods do not work well at characterizing all locations in all directions. Similar considerations restrict the usage of Fourier methods, where large matrices must be inverted to produce a solution. Typical studies such as those by Kobayashi (1991) and Li *et al.* (1994b) restrict the positional or angular variation of the analysis space in order to limit the size of the matrix to be inverted. For the size of our sample volume, at a resolution that characterizes typical natural cloud dimensions, the size of matrix necessary becomes impossibly large. For example, Fiveland (1987) indicates at least a 24-stream solution is required to provide reasonable directional information on radiant intensity for visualization purposes. To achieve this resolution for our typical 32^3-cell spatial model using a Fourier method, one would need to invert a matrix of $(32^3 \times 24)^2 = 786,432^2 = 6.2 \times 10^{11}$ elements. This approach appears highly impractical. Other analytical methods appear to be as restricted in application as the Fourier methods. These considerations led to the selection of the DOM in 3D using a finite-element approach.

DOM was originally developed by Chandrasekhar (1960), from which two parallel courses were pursued. The first, primarily useful in astronomical and satellite applications, focused on 1D modeling (Liou (1973), Stamnes and Swanson (1981), Stamnes *et al.* (1988)), culminating in the development of the DISORT (DIScrete Ordinates Radiative Transfer) routine, a standard in the field. The second effort focused on 3D modeling, with applications primarily in furnace technology and nuclear scattering. The basic theory for this application was the so-called Finite Element (FE) DOM (Carlson and Lathrop 1968). Improvements to this theory included better simulation of scattering via the scaling group transformation (McKellar and Box 1981), as commonly implemented through Wiscombe's (1977) δ-M method. Numerous applications of the DOM include study of radiative interaction with the Earth's surface (Zardecki *et al.* (1983), Gerstl and Zardecki (1985a, 1985b)), furnace technology (Fiveland (1985, 1987)), and foliated canopies (Myneni *et al.* (1990, 1991)). But, problems still remain with handling dense media under DOM. Some attempts have been made to correct these problems (Wakil and Sakadura (1992), Chai et al. (1994)), but these have mainly been patches to the basic theory.

The development described here has its roots in neutron scattering work of the 70's. We use a level symmetric even quadrature set (Lathrop and Carlson (1965); Fiveland (1991)) proposed by Lewis and Miller (1984). More recently, Zardecki and Davis (1991) and Wetmore and Zardecki (1993) developed the immediate predecessor of the model described herein: the Boundary Layer Illumination and Radiative Balance model (`BLIRB`).

Unfortunately `BLIRB` attempted to model 3D effects using traditional FE DOM, leading to the use of the so-called negative flux fixup patch. The problem of negative fluxes (Fiveland (1985); Gerstl and Zardecki (1985a); Wakil and

Sakadura (1992)), occurs when the optical thickness across model cells exceeds a threshold value. Then, the computational method for evaluating stream radiance exiting the cell can result in negative values. Under the traditional approach, the only means of avoiding this problem is to limit the maximum optical depth of a cell by limiting the cell dimensions or through use of an auxiliary method of compensation known as the negative flux fixup. This coding patch artificially allows denser media within a simulation, but it does not alleviate the consequent lack of accuracy of the model results. That is, how do you establish what the right value should be if your estimate is a negative number?

Although alternative corrections have been suggested (Wakil and Sacadura 1992), a general FE DOM for arbitrary media density has heretofore been lacking. Moreover, DOM techniques have often employed flux renormalizations to conserve energy (Myneni *et al.* 1990). But since the negative flux fixup produces cloud regions that are artificially darkened, renormalization attempts then merely tend to overbrighten regions between clouds without properly restoring cloud brightness.

In section 2, a methodology for alleviating this modeling deficiency is presented where a surface-based DOM computation technique is proposed. In section 3, a Monte Carlo model is described and compared with standard literature results (McKee and Cox 1974). In section 4, this Monte Carlo model is used to evaluate the results of the proposed method, using the McKee and Cox scenarios and 3D extensions to these scenarios. In section 5, the results of the radiative transfer code are utilized in a cloud rendering technique, and the formats of standard outputs are described for use in other applications.

1.3 Support

This software was developed as a consequence of funding under several joint programs mentioned in the acknowledgements section. Currently, products from this software are provided through the Master Environmental Library project, a joint DoD program sponsored by the Defense Modeling and Simulation Office. Support for this software can be obtained by contacting:

1.3.1 Mailing Address

U.S. Army Research Laboratory
ATTN: AMSRL-IS-EW (D. Tofsted)
White Sands Missile Range, NM 88002-5501

1.3.2 Phone Numbers and E-Mail Addresses

Radiative transfer models and derived output products:
COM:(505) 678-3039
 FAX:(505) 678-3385
 DSN: 258-3039
email:dtofsted@arl.mil

Visualization products and LOS integrations using RT code outputs:
COM:(505) 678-1570
 FAX:(505) 678-3385
 DSN: 258-1570
email:sobrien@psl.nmsu.edu

2. DOMRT

2.1 The Radiative Transfer Equation

The Discrete-Ordinate Method approach to Radiative Transfer (DOMRT) is a standard technique used in numerically solving the equation of radiative transfer. We begin by describing the traditional approach.

In the initial step, the scattering volume is divided into a collection of gridded cells. Each cell is assumed to exhibit uniform scattering properties throughout. The method then determines the radiance properties of diffuse radiation flowing within each cell in a series of directions. In deriving the standard equation used, one begins with the equation of radiative transfer,

$$\hat{\Omega} \cdot \nabla I(\vec{r}, \hat{\Omega}) + \sigma \, I(\vec{r}, \hat{\Omega}) = \sigma_s \int_{4\pi} I(\vec{r}, \hat{\Omega}') \, P(\hat{\Omega}, \hat{\Omega}') \, d\hat{\Omega}' + (\sigma - \sigma_s) b(T(\vec{r}), \, \lambda), \quad (7)$$

where, $I(\vec{r}, \hat{\Omega})$ is the streaming radiance at position $\vec{r}$ and in direction $\hat{\Omega}$. $\hat{\Omega}$ is a unit vector composed of direction cosines μ, η, and ξ along the x, y, and z axes, respectively. $P(\hat{\Omega}, \hat{\Omega}')$ is referred to as the phase function, representing the probability of scattering of a photon between incident and departing directions ($\hat{\Omega}'$ and $\hat{\Omega}$, respectively), given that a scattering occurs. The normalization condition for $P(\hat{\Omega}, \hat{\Omega}')$ is that integration over all possible scattering directions equals unity:

$$\int_{4\pi} P(\hat{\Omega}, \, \hat{\Omega}') \, d\hat{\Omega}' = 1. \tag{8}$$

Also, due to the principle of reciprocity (Van de Hulst 1980a), one must have

$$P(\hat{\Omega}, \, \hat{\Omega}') = P(\hat{\Omega}', \, \hat{\Omega}). \tag{9}$$

The first term on the left in Eq. (7) represents the differential change in the streaming radiance, I, along direction $\hat{\Omega}$. The second term on the left represents combined extinction losses in the stream radiance due to absorption and scattering. The right-hand side (RHS) consists of contributions to the stream radiance due to scattering and graybody emissions within the medium (first and second terms, respectively). In the scattering integral, $d\hat{\Omega}'$ is a differential

solid angle, σ is the extinction coefficient, σ_s is the scattering coefficient, and $b(T(\vec{r}), \lambda)$ is the blackbody emission function.

Let us now simplify the writing of Eq. (7) through the use of the terms J and B, where J is the scattering source term,

$$J(\hat{\Omega}, \vec{r}) = \varpi(\vec{r}) \int_{4\pi} I(\vec{r}, \hat{\Omega}') P(\hat{\Omega}, \hat{\Omega}') d\hat{\Omega}', \tag{10}$$

and B is the emissive source term,

$$B(\vec{r}, \lambda) = (1 - \varpi(\vec{r})) b(K(\vec{r}), \lambda), \tag{11}$$

where λ is the radiation wavelength (expressed here in μm), and K is the temperature (in Kelvin) of the medium, as a function of position. The coefficient ϖ is the single scattering albedo, representing the probability that a collision of a photon with a particle will result in a scattering event. The assumption of local thermodynamic equilibrium dictates that the probability of an emission event is proportional to $(1 - \varpi)$. Hence, $\sigma - \sigma_s = (1 - \varpi)\sigma = \sigma_a$ is the absorption coefficient. Together, the sum of J and B equals the limiting path radiance, L.

The blackbody emission function may be written as,

$$b(T(\vec{r}), \lambda) = \frac{1.19106 \times 10^8 \, \lambda^{-5}}{\exp[14,388/(\lambda T)] - 1}, \tag{12}$$

producing a result with units of W/m^2-sr-μm. (All results of this derivation represent spectral radiances, but the frequency dependence hereafter will be suppressed.)

Using these definitions, the radiative transfer equation reduces to,

$$\hat{\Omega} \cdot \nabla I(\vec{r}, \hat{\Omega}) + \sigma \, I(\vec{r}, \hat{\Omega}) = \sigma \left[J(\vec{r}, \hat{\Omega}) + B(\vec{r}) \right]. \tag{13}$$

If the medium is now discretized such that T, σ, ϖ, and the scattering source integral are assumed constant over the span of a cell, then the RHS of Eq. (13) is constant, and one can introduce the variable Υ, defined as,

$$\Upsilon(\hat{\Omega}, \vec{r}) = I(\hat{\Omega}, \vec{r}) - L(\hat{\Omega}, \vec{r}) = I(\hat{\Omega}, \vec{r}) - J(\hat{\Omega}, \vec{r}) - B(\vec{r}, \lambda). \tag{14}$$

Introducing this variable in Eq. (13) we find,

$$\hat{\Omega} \cdot \nabla \Upsilon(\vec{r}, \hat{\Omega}) + \sigma \, \Upsilon(\vec{r}, \hat{\Omega}) = 0. \tag{15}$$

This equation can be solved if we make two more assumptions. First, we assume that the input stream values to a cell are constant over each input face. Second, we evaluate the scattering source term J by taking an average of the unscattered stream energy over the volume of each cell. We then evaluate the average radiance of a given stream exiting a given cell face by averaging the output results over that face. This average then forms the basis for use as an incident value in the next adjacent cell.

2.2 Level Symmetry Quadrature Sets

Before continuing with this train of thought, though, we must consider the heart of the discrete ordinates approach. Under this approach, all integrations over solid angle are approximated by summations over a specially selected set of sample directions, $\hat{\Omega}_m$. (Sets of sample directions are available at increasing numbers of sample stream points.) As higher order ordinate expansions are used, the method becomes progressively better. In our study, level symmetric sets of ordinates using Gaussian quadrature have been chosen (Lewis and Miller 1984). While these sets have certain limitations regarding flux integration (Fiveland 1991), we minimize the error associated with these integrations in the approach developed.

A level symmetry set means that the diffuse stream directions $\hat{\Omega}_m$ are characterized by combinations of a single set of component values χ_i which are symmetric about the zero planes in x, y, and z.

Each order of approximation is denoted by the symbol S_N, where S indicates a level symmetry and N represents the order of approximation. The values for N are even integers ranging upward from 2. For a given order of approximation N, there will be $N \times (N + 2) = M$ streams. Thus S_2 is an 8-stream approximation, S_4 is a 24-stream model, and S_6 is a 48-stream model. For the time being we will focus on the S_2 and S_4 cases, though extensions to higher orders are readily available.

To understand how the number of streams are related to the order of approximation, consider that each streaming direction $\hat{\Omega}_m$ can be described by a set of three integers i, j, k, where $\mu = \chi_i$, $\eta = \chi_j$, $\xi = \chi_k$, such that

$$\chi_i^2 + \chi_j^2 + \chi_k^2 = 1. \tag{16}$$

There are $N/2 - 1$ unique triplets for level symmetric set S_N. Lathrop and Carlson (1965) have shown that only one degree of freedom remains in choosing the direction cosines, using the relation:

$$\chi_j^2 = \chi_1^2 + 2\frac{j-1}{N-2}(1 - 3\chi_1^2). \tag{17}$$

Of course, when $N = 2$ there are no degrees of freedom, since, necessarily, $\chi_1 = \sqrt{1/3}$; $\chi_2 = -\chi_1$. In the derivation of Eq. (17) the last term is assumed positive, which requires $0 \le \chi_1^2 \le 1/3$ (Fiveland 1991).

For the S_2 and S_4 approximations considered in this paper, the χ_i's are $-\sqrt{1/3}$ and $\sqrt{1/3}$ in the 8-stream approximation, and equal to -0.8688903, -0.3500212, 0.3500212, and 0.8688903 in the 24-stream model. Thus, for S_2, there is only one combination of χ values possible for an $\hat{\Omega}$ vector in the first octant, or eight possible directions when all octants are considered. For S_4, there are three possibilities for vectors in the first octant: let $\chi_1 = 0.3500212$ and $\chi_2 = 0.8688903$. Then, $\hat{\Omega}_1 = (\chi_2, \chi_1, \chi_1)$; $\hat{\Omega}_2 = (\chi_1, \chi_2, \chi_1)$; $\hat{\Omega}_3 = (\chi_1, \chi_1, \chi_2)$. Similar permutations occur in each of the other seven octants, resulting in 24 streams total.

2.3 Angular Integration

The value of the discrete ordinates approach is that scattered energy at any angle can be interpolated to the degree of resolution of the approximation used. Thus, there is always a means of expressing radiance in all directions, as opposed to methods such as Monte Carlo, where the means of interpolating intermediate directions can be ambiguous.

The general equation for performing angular integrations under the discrete ordinates approach is via the approximation:

$$\frac{1}{4\pi} \int_{4\pi} f(\hat{\Omega}) \, d\hat{\Omega} \approx \frac{1}{8} \sum_{m=1}^{M} w_m \, f(\hat{\Omega}_m). \tag{18}$$

where $\hat{\Omega}_m$ are the discrete ordinate directions, which depend on the particular order of approximation and ordinate direction selection scheme chosen, and the w_m are weighting coefficients. In essence, the w_m measure the fraction of an octant of solid angle that is being occupied (influenced) by that ordinate; in particular, $w_m = 1$ in the 8-stream model and $w_m = 1/3$ in the 24-stream model.

The DOM using Gaussian quadrature is useful when dealing with RT problems in that the choice of directions can be closely matched to the means of expressing the scattering phase function as a low order Legendre expansion. In general, the level of detail in a discrete ordinate method is directly related to the level of detail desired in the Legendre expansion of the phase function. That is, using the discrete ordinates technique, one approximates the phase function $(P(\mu))$ by a finite sum of a series of weighted Legendre polynomials as

$$P(\mu) \approx \tilde{P}(\mu) = \sum_{\ell=0}^{N} \alpha_\ell \, X_\ell \, P_\ell(\mu), \quad X_\ell = 2\pi \int_{-1}^{1} P(\mu') \, P_\ell(\mu') \, d\mu', \quad \alpha_\ell = \frac{2\ell+1}{4\pi}. \tag{19}$$

where $P_\ell(\mu)$ is ℓth Legendre polynomial,

$$P_\ell(\mu) = \frac{1}{2^\ell \ell!} \frac{d^\ell}{d\mu^\ell} (\mu^2 - 1)^\ell, \tag{20}$$

and μ is the cosine of the angle between incident and scattered directions.

For a given discrete ordinates model (S_N), the limit (N) of the summation $\tilde{P}(\mu)$ is the same as the limit of the stream model N value used. This ensures the adequate precision of angular integrals. However, the summation $\tilde{P}(\mu)$ is seldom used in the raw form seen above. Instead, the scaling transformation is used to modify the Legendre polynomial weighting constants X_ℓ to remove the forward peak of the phase function. The appendix describes a modified version of the scaling transformation approach that optimizes the choice of Legendre weighting

coefficients. This approach also results in changes to the coefficients σ and ϖ used in the scattering computations on a cell-by-cell basis. In the development that follows, this step has been assumed completed such that the resulting phase function has no forward peak.

From our discrete ordinates approach, then, the scattering source function J_m for propagation direction $\hat{\Omega}_m$ is

$$J_m(\vec{r}) = \varpi(\vec{r}) \frac{4\pi w}{8} \sum_{m'=1}^{M} P(\hat{\Omega}_m, \hat{\Omega}_{m'}) I_{m'}(\vec{r}). \qquad (21)$$

2.4 Low-Density DOMRT

Armed with this understanding of the discrete ordinates approach to angular integration, from first principles we proceed to generate a set of equations for all diffuse streams and to determine the net radiation flowing in any direction at any position within the scattering volume.

Let s be a distance variable in the direction of propagation $\hat{\Omega}_m$. Then Eq. (15) can be written as a function of distance s across the cell,

$$\frac{d\Upsilon_{\hat{\Omega}_m}(s)}{ds} + \sigma\, \Upsilon_{\hat{\Omega}_m}(s) = 0, \qquad (22)$$

which has the explicit solution,

$$\Upsilon_{\hat{\Omega}_m}(s) = \Upsilon_{\hat{\Omega}_m}(0)\, \exp(-\sigma\, s), \qquad (23)$$

where σs is an optical depth measure, and $\exp(-\sigma s)$ is a transmittance.

Converting back to the original variables, we find a solution for the streaming radiance over a single cell,

$$I_{\hat{\Omega}_m}(s) = I_{\hat{\Omega}_m}(0)\, \exp(-\sigma\, s) + L_{\hat{\Omega}_m}\, [1 - \exp(-\sigma\, s)], \qquad (24)$$

where $L_{\hat{\Omega}_m} = L_{\hat{\Omega}_m}(0) = L_{\hat{\Omega}_m}(s)$ is the sum of the source contributions to radiance, assumed constant within the cell (c.f., Lewis and Miller 1984).

2.4.1 Propagation Equation Terms

Under traditional DOM, the transmission factor is linearized, whereby

$$\exp(-\sigma\, s) \approx [s^{-1}/(s^{-1} + \sigma\,)]. \qquad (25)$$

Figure 1 compares this approximation with the actual negative exponential function via a plot of $\exp(-\sigma s)/[s^{-1}/(s^{-1} + \sigma\,)]$. As the figure illustrates, this approximate function is only valid for very small optical depths. For
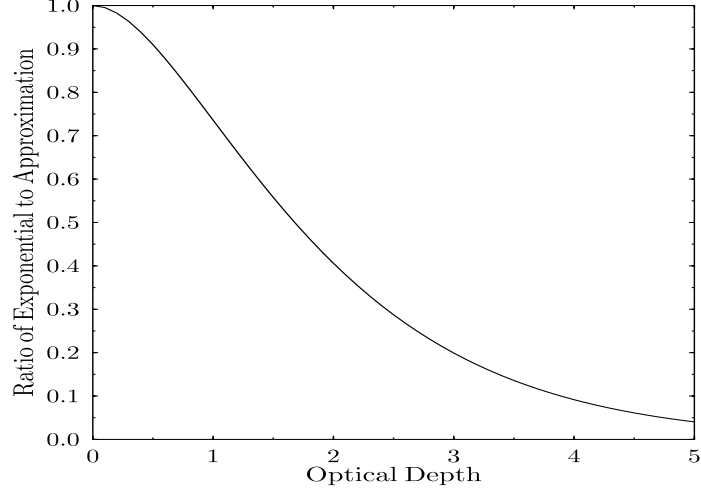
Figure 1. Ratio of the negative exponential function $\exp(-\sigma s)$ to the approximation curve $[s^{-1}/(s^{-1} + \sigma)]$. The two functions are only roughly equal around an optical depth of zero. (Optical depth is $\tau = \sigma s$.)

larger optical depths the approximate transmittance far exceeds the actual transmittance function.

Introducing Eq. (25) into Eq. (24) produces the result,

$$I_{\hat{\Omega}_m}(s) = \frac{s^{-1} I_{\hat{\Omega}_m}(0) + \sigma L_{\hat{\Omega}_m}}{s^{-1} + \sigma}, \qquad (26)$$

where s is usually replaced by the distance to the center of the cell.

In standard texts describing this approach, the streaming energy is discretized such that a stream directed in the $\hat{\Omega}_m$ direction at position $(x_i,\ y_j,\ z_k)$ is assigned a value $I_{(m,i,j,k)}$. Stream radiances at walls are identified by the use of half indices. For example, for a stream flowing into the first octant, there would be surface-based stream values at the x $(I_{(m,i-1/2,j,k)})$, y $(I_{(m,i,j-1/2,k)})$, and z $(I_{(m,i,j,k-1/2)})$ input faces. On each of these input faces, the modeled net energy crossing the face is proportional to $\mu \Delta_y \Delta_z$ on the x input face, $\eta \Delta_x \Delta_z$ on the y input face, and $\xi \Delta_x \Delta_y$ on the z input face, where the Δ's are the cell lengths along the respective subscripted axes.

Thus, in each case, the net energy crossing the input face of the cell is proportional to the cosine of the stream with the input face multiplied by the surface area of the face itself. The mean source radiance at the cell edge can therefore be expressed as a surface average over the three input surfaces:

$$I_{\hat{\Omega}_m}(0) \approx \frac{\mu \Delta_y \Delta_z I_{(m,i-1/2,j,k)} + \eta \Delta_x \Delta_z I_{(m,i,j-1/2,k)} + \xi \Delta_x \Delta_y I_{(m,i,j,k-1/2)}}{\mu \Delta_y \Delta_z + \eta \Delta_x \Delta_z + \xi \Delta_x \Delta_y}.$$

$$(27)$$

24

Dividing numerator and denominator by $\Delta_x \Delta_y \Delta_z / 2$ we obtain,

$$I_{\hat{\Omega}_m}(0) \approx \frac{2\mu I_{(m,i-1/2,j,k)}/\Delta_x + 2\eta I_{(m,i,j-1/2,k)}/\Delta_y + 2\xi I_{(m,i,j,k-1/2)}/\Delta_z}{2\mu/\Delta_x + 2\eta/\Delta_y + 2\xi/\Delta_z}.$$
(28)

$I_{\hat{\Omega}_m}(0)$ thus represents a weighted average of the projected intensities on the three input faces of the volume of interest. This mean initial value for the stream is the first unknown on the RHS of Eq. (26). The second unknown is the choice of the distance parameter s measuring the distance to the center of the cell. In the standard approach s is normally determined as,

$$\frac{1}{s} = \frac{2\mu}{\Delta_x} + \frac{2\eta}{\Delta_y} + \frac{2\xi}{\Delta_z},$$
(29)

where $\Delta_x/2\mu$ would be the total distance travelled by a ray crossing a plane-parallel slab of thickness $\Delta_x/2$ that makes a cosine of μ with the slab normal.

The $L_{\hat{\Omega}_m}$ represents the volume centered limiting path radiance based on the $I_{(m,i,j,k)}$ values obtained from a previous iteration of the model, the direct illumination for that cell, and the cell centered temperature $T_{(i,j,k)}$.

2.4.2 Low-Density Limitations

Though variations on the above described approach have been investigated, one essential point remains: the intensity projected for the opposite side of the cell is typically derived via extrapolation of its value at the cell center. One particular choice for this extrapolation is known as the diamond difference technique. To illustrate this technique, let I_- be the initial value of the stream at the near edge of the cell (previously $I_{\hat{\Omega}_m}(0)$), let $I_\circ$ be the cell-centered value ($I_{\hat{\Omega}_m}(s)$), and let I_+ be the estimate for the stream at the far side of the cell ($I_{\hat{\Omega}_m}(2s)$). Under the diamond difference, the central stream value is simply approximated as the mean of the stream values at the opposite sides of the cell ($I_\circ = \frac{1}{2}(I_- + I_+)$). To estimate the stream value at the far side of the cell, this equation is simply inverted to produce:

$$I_+ = 2I_\circ - I_- = 2\frac{s^{-1}I_- + \sigma L_{\hat{\Omega}}}{s^{-1} + \sigma} - I_- = \frac{s^{-1}I_- + \sigma(2L_{\hat{\Omega}} - I_-)}{s^{-1} + \sigma}.$$
(30)

Difficulties arise whenever $2L_{\hat{\Omega}} < I_-$ because the numerator has the potential to become negative for large optical depths. For example, what happens when modeling a cloud covering more than one cell? Normally, models begin by setting all radiances initially to zero. Hence, on the first pass, $L_{\hat{\Omega}} \equiv 0$. Figure 2 shows
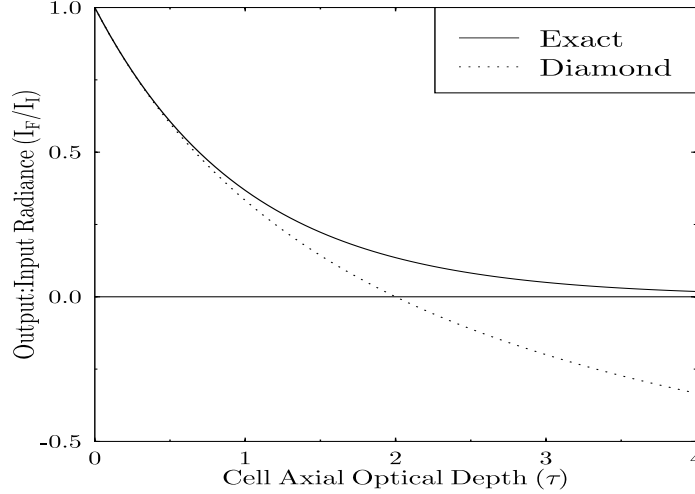
Figure 2. Negative flux consequences of the diamond difference equation.

the behavior of I_+ in this case as σ increases. This indicates that for cell optical depths greater than 2, the flux will be estimated as negative.

This problem must be patched in order to hope for a reasonable solution. One patch, the so-called negative flux fixup, yields a numerically stable algorithm whereby all negative fluxes are simply reset to zero. However, the result of using this fix produces difficulties in interpreting the appropriate brightness of regions where these negative values persist throughout successive iterations of the modeled volume. In the case mentioned above, where a cloud spans more than one model cell, the zero values produced on outer cells may never allow energy to propagate into the volume to reach an inner cell. The algorithm then predicts black regions that are physically unreasonable in terms of typical cloud scattering properties. Some better means of treating optically dense clouds is thus sought here.

Other authors have proposed modifications of the standard discrete ordinate method (c.f. Wakil and Sacadura (1992) and Chai *et al.* (1994)). However, these modifications retain the usage of a cell-centered computation of the limiting path radiance and still require renormalization to produce energy balance. In the next section, a theoretical discussion of a discrete ordinates radiative transfer solution is presented which extends the traditional volume-based concepts to a surface-based method. It is shown that this reworking of the discrete ordinates approach improves the performance of the discrete ordinates results for dense media and can support a system which automatically conserves energy.

26

2.5 Surface-Based DOM

In this section, an approach is developed to track available diffuse energy sources using surface-based input and output stream radiances over an individual scattering cell. We first discuss transmission across the cell between input and output faces. We then focus on evaluating the volume averaged unscattered radiation due to energy entering the cell through a single cell wall along a single streaming direction. Using this result, and assuming the diffuse energy available in a given streaming direction is constant across a given input surface, one can determine the influence of that stream on the path radiance of any stream as it exits the volume through a given surface element. Also, from the standpoint of an output face, the average transmission through the volume for a given stream exiting a given face can be determined. From this information, one can compute the average contribution of volume-based path radiance to an output stream from all input streams. This information can then be combined to determine the net fractional energy accounted for due to volume-based transmission, absorption, and diffuse scattering processes for energy entering a given face via a given stream. It is argued that the remaining energy can be accounted for by a surface scattering/absorption procedure.

Since all results must be expressed in terms of output surface radiances, this is best accomplished by averaging Eq. (24) over an output face,

$$\langle I_{\hat{\Omega}_m}(s) \rangle = \left\langle I_{\hat{\Omega}_m}(0) \, \exp(-\sigma \, s) \right\rangle + \left\langle L_{\hat{\Omega}_m} \left[1 - \exp(-\sigma \, s) \right] \right\rangle . \tag{31}$$

Note that $L_{\hat{\Omega}_m}$ already represents a volume average; what remains are evaluations of the output face averaged transmission factor and the expectation value of the product factor, which is the first term on the RHS of Eq. (31). In this calculation, we are aided by the assumption that all input radiances are constant over each input face. This first term thus is reëxpressed as a weighted sum of terms as explained in the following sections.

2.5.1 Cell Geometry

In describing these expectation values, we begin by representing the directional vector $\hat{\Omega}$ by its three directional cosines (μ, η, ξ) in x, y, and z directions, respectively. Because the cells have a cubical geometry, we can assign a 'standard' stream chosen to flow **into** the first octant, principally in the ξ direction. Hence, $\xi \geq \mu > 0$; $\xi \geq \eta > 0$. The appearance of the cell with respect to the incident stream is illustrated in figure 3 as it appears to an incident stream. In the figure, the z axis extends **into** the page, and the origin is labeled **O**, near the lower left corner.

For any stream, there will always be three input faces and three output faces. We identify the various faces of the volume using a sign (+/-) and letter (X, Y, Z) convention. In the standard scenario, because ξ, μ, and η are all greater than zero, the input faces will be identified as the -X, -Y, and -Z faces; the output
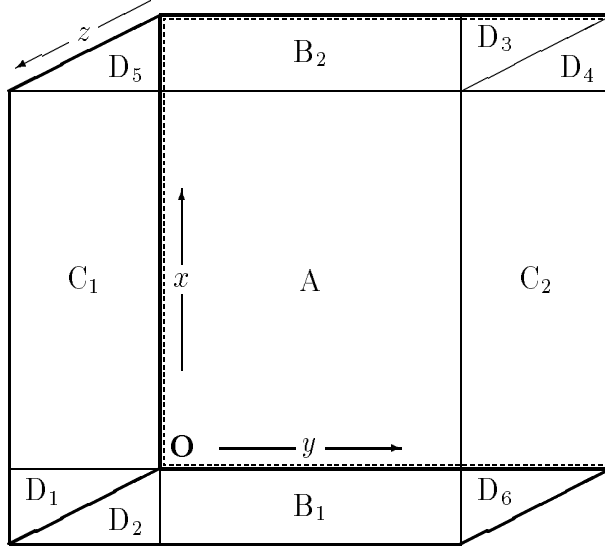
Figure 3. Division of a cell for transmission purposes. Face-on view as seen by energy in the incident stream.

faces will be the +X, +Y, and +Z faces. We subdivide each of the 3 input faces into a set of rectangular and triangular faceted subareas as shown in figure 3. There are four types of such subareas, labeled with letters A, B, C, and D.

To better understand the subdivision of the cell input faces into these different facets, we provide two additional figures. Figure 4 shows the cell segmenting system as the stream enters and exits the cell from a rotated viewing position. Figure 5 shows the same stream and segmenting system; dashed lines have been added to show the hidden boundaries of the segmented portions within the volume. In addition, letters in figure 5 denote the corners of the volume segments.

In table 1, the descriptions of the input and output faces of each volume segment are given to clarify the connection between figure 3 and figures 4 and 5. The designation of the appropriate input and output faces with which each segment is associated, along with the appropriate corner point labels, are given to help understand the 3D nature of the volume and its segments.

In the type A area, the optical depth is constant at each point over the rectangular input face. In figure 5, this corresponds to an optical depth experienced over the path from input point **a** to output point **n**. Geometrically, this volume is a parallelepiped. For type B and C input regions, the geometry is that of a wedge: the optical depth is constant along one axis and linearly increasing along the second. Type D areas represent the bases of trigonal pyramids, with a maximum optical depth along the edge bordering the A region, and have optical depth decreasing linearly down to zero on the opposite side.

28

Figure 4. Subdivided cell revealing input and output surfaces in a rotated view for the same stream used in figure 3.

Figure 5. Subdivided cell showing hidden edges bordering different volume segments in a rotated view.
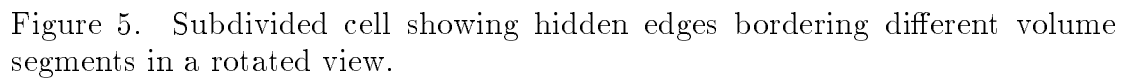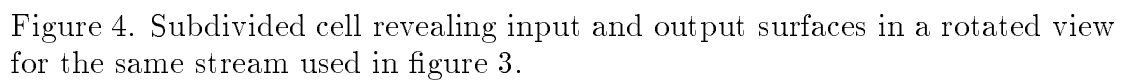
Table 1. Input and output face designations for surface facets

Region	Input Face	Input Surface Corners	Output Face	Output Surface Corners
A	-Z	a,b,d,e	+Z	n,o,q,r
B_1	-X	a,b,k,l	+Z	k,l,n,o
B_2	-Z	d,e,g,h	+X	g,h,q,r
C_1	-Y	a,d,m,q	+Z	m,n,p,q
C_2	-Z	b,c,e,f	+Y	c,f,o,r
D_1	-Y	a,j,m	+Z	j,m,n
D_2	-X	a,j,k	+Z	j,k,n
D_3	-Z	e,h,i	+X	h,i,r
D_4	-Z	e,f,i	+Y	f,i,r
D_5	-Y	d,g,p	+X	g,p,q
D_6	-X	b,c,l	+Y	c,l,o

2.5.2 Facet Transmittances

From the standpoint of the discrete ordinates method, **all** the energy in a given stream is considered to be traveling in the same direction ($\hat{\Omega}_m$), even though it is applied over a specific solid angle during integration. Second, the geometry of all cells is assumed cubic. Thus, every cell in the scattering volume is characterized by a single cell-width parameter Δ. Energy entering a cube through the area labeled A experiences a total optical depth, τ, equal to $\sigma \Delta / \xi$, as it crosses the volume. So the area-averaged mean transmittance for flux entering the volume through area A is

$$\bar{T}_A = \exp(-\tau). \tag{32}$$

Area types B, C, and D have more complicated forms for the transmittance equations due to their modified geometries.

For type B and C areas, the mean transmittance can be computed by taking the integral of the point-to-point transmittance at each point on the surface and dividing by the total surface area to produce:

$$\bar{T}_B = \bar{T}_C = \int_0^1 \exp(-\tau u)\, du = \frac{e^{-\tau} - 1}{-\tau}. \tag{33}$$

Notice that this result depends on $\tau = \sigma \Delta / \xi$, but not on the exact length and width of the region, since it is surface averaged.

For type D areas, the mean transmittance is again determined by integration:

$$\bar{T}_D = 2 \int\limits_0^1 du \int\limits_0^u dv \, \exp(-\tau v) = \frac{e^{-\tau} - (1 - \tau)}{\tau^2/2}. \tag{34}$$

Here, division by the area normalization factor $(1/2)$ results in the factor 2 appearing in front of the integral.

For the sake of brevity, these results can be described using an apparently new class of related functions:

$$G_i(\tau) = \frac{\left[e^{-\tau} - \sum_{j=0}^{i-1} \left[(-\tau)^j / j! \right] \right]}{(-\tau)^i/i!} = \sum_{j=0}^{\infty} \frac{i!}{(i+j)!}(-\tau)^j. \tag{35}$$

Thus, we can represent the average transmittances for cell wall regions A, B, C, and D as $\bar{T}_A = G_0(\tau)$, $\bar{T}_B = \bar{T}_C = G_1(\tau)$, and $\bar{T}_D = G_2(\tau)$. Comparisons of the G functions are given in figures 6 and 7. The first of these illustrates the basic behaviors of these functions. (We extend these results up to $G_3(\tau)$ because this functional form is relevant in further calculations.) Figure 7 illustrates the normalized behaviors of this class of functions. Note that successive functions have limiting behaviors $G_i(\tau) \approx 1 - \tau/(i+1)$ for small τ. But, even after normalizing these functions according to their limiting behavior around zero, higher order G functions are always greater than lower order functions. This illustrates the fact that energy passing through a cell between adjacent walls experiences far less attenuation than is predicted by the negative exponential function, and partially explains why the classical FE DOMRT methods fail.
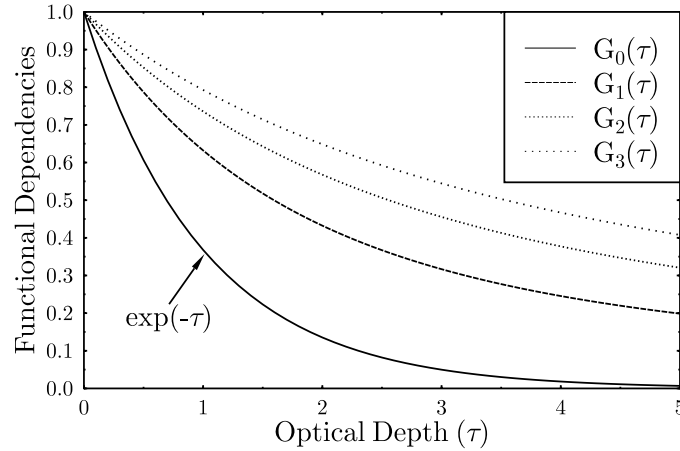
Figure 6. Comparison of transmittance functions $G_i(\tau)$ for i values ranging from 0 to 3.
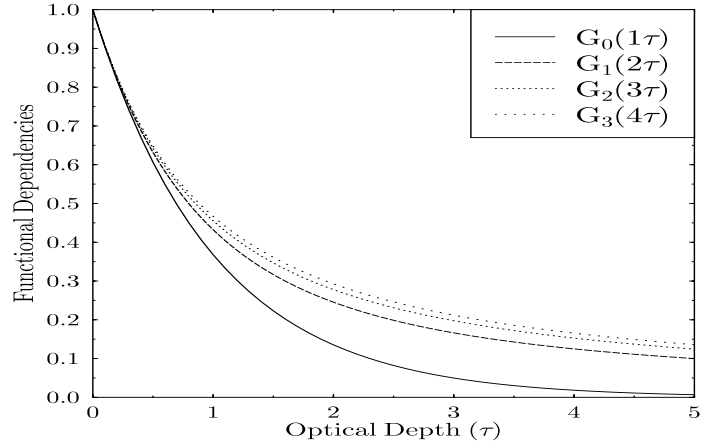
Figure 7. Comparison of transmittance functions $G_i(\tau)$ normalized according to their limiting behavior around $\tau = 0$.

2.5.3 Face-to-Face Transmittances

Using these results, one may describe the mean transmittance of energy flowing from one input face to a given output face through weighted averages of the transmittances of its different facets.

To produce these transmission functions, the parameters $\alpha = |\mu/\xi| \leq 1$, and $\beta = |\eta/\xi| \leq 1$, are introduced. We also introduce area measurements that are determined via projections onto a plane containing the -Z face (figure 3). The projected areas subtended by the various surface portions with respect to this plane are given in table 2.

Table 2. Region area values for subcomponents of input surfaces

Region Type	Region Area
A	$(1-\alpha)(1-\beta)\Delta^2$
B	$\alpha(1-\beta)\Delta^2$
C	$(1-\alpha)\beta\Delta^2$
D	$\alpha\beta\Delta^2/2$

One can then determine the average transmittance from a given input wall to a given output wall by forming a weighted average of the transmittances of the various facets of each input wall connecting to each output wall. These

calculations form a matrix with components detailed as follows: The -Z and +Z walls only connect through the type A area. Hence,

$$T_{-Z,+Z} = G_0(\tau).$$ (36)

The X and Z walls connect via a D-type and a B-type volume segment. Let A_B and A_D be the projected areas of these walls respectively. Thus,

$$T_{-Z,+X} = T_{-X,+Z} = \frac{A_B \bar{T}_B + A_D \bar{T}_D}{A_B + A_D},$$ (37)

which results in,

$$T_{-Z,+X} = T_{-X,+Z} = \frac{2G_1(\tau) - \beta[2G_1(\tau) - G_2(\tau)]}{2 - \beta},$$ (38)

where the α factor cancels out of the numerator and denominator. A similar development can be performed for the connectivity between Z and Y-type surfaces,

$$T_{-Z,+Y} = T_{-Y,+Z} = \frac{2G_1(\tau) - \alpha[2G_1(\tau) - G_2(\tau)]}{2 - \alpha}.$$ (39)

The X and Y faces only connect through single facets (D_5 and D_6) and thus are characterized by,

$$T_{-X,+Y} = T_{-Y,+X} = G_2(\tau).$$ (40)

Lastly, neither the X nor Y faces connect directly between their input and output faces:

$$T_{-Y,+Y} = T_{-X,+X} = 0.$$ (41)

Subscripts in these equations indicate the face connections. The resulting matrix is diagonally symmetric.

In addition to the foregoing transmittance factors connecting input and output surfaces for the standard scenario, we may also determine the mean transmittance factors to each output face ($+X$, $+Y$, and $+Z$) to all connected input faces. These calculations are accomplished by constructing a weighted sum of the previous transmittance factors, where the weights are determined according to the fraction of the output face connecting to each input face. For an X-type output face, the energy is passing through 2 D-type facets and 1 B-type facet. Thus,

$$\bar{T}_X = \frac{A_B \bar{T}_B + 2 A_D \bar{T}_D}{A_B + 2 A_D},$$ (42)

which results in,

$$\bar{T}_X = G_1(\tau) - \beta[G_1(\tau) - G_2(\tau)].$$ (43)

A similar result is obtained for Y-type faces,

$$\bar{T}_Y = G_1(\tau) - \alpha[G_1(\tau) - G_2(\tau)].$$ (44)

For Z-type faces, the summation averages the results over an A-, a B-, a C-, and two D-type facets, leading to the result,

$$\bar{T}_Z = \gamma\delta G_0(\tau) + (\alpha\delta + \gamma\beta)G_1(\tau) + \alpha\beta G_2(\tau), \tag{45}$$

where $\gamma = 1 - \alpha$ and $\delta = 1 - \beta$.

Due to the symmetries of the problem, Eqs. (43) through (45) also represent the average transmittance through the volume **from** a given input face of the same type. That is, $\bar{T}_Z$ is both the mean transmittance of energy entering the volume through a Z-type input face and the average transmittance of energy exiting the volume through a Z-type output face.

These computations allow us to determine both the total amount of flux lost due to scattering and absorption from the stream as it enters a given face, and also allow for an emission term to be evaluated on a similarly labeled output face. For example, if the average transmission through the volume **to** a given output face is labeled T_Q, then $(1 - T_Q)$ represents a source factor in the emittance portion of the radiative transfer solution for that output face.

Therefore, let us return to Eq. (31), where as we already noted, the factor $L_{\hat{\Omega}_m}$ already represents a volume average result. Thus, this factor may be removed from the expectation operator, resulting in,

$$\langle I_{\hat{\Omega}_m}(s)\rangle = \left\langle I_{\hat{\Omega}_m}(0)\exp(-\sigma\,s)\right\rangle + L_{\hat{\Omega}_m}\left[1 - \langle\exp(-\sigma\,s)\rangle\right]. \tag{46}$$

The quantity within expectation operator in the second term on the RHS of the equation is just the T_Q terms we have just derived.

Further, with our current understanding of the transmission factors between different cell faces, we can evaluate the first term on the RHS directly. Recall that one of our assumptions was that the input radiances were assumed constant over each input face. We therefore introduce the terms I_X, I_Y, and I_Z for our standard scenario X, Y, and Z input face radiances, respectively. The first term on the right, under our constant input assumption, becomes a weighted sum of the area of a given facet times the input radiance applicable for that facet times the average transmission factor for that facet. For example, for an X-type output face we have,

$$\begin{aligned}\left\langle I_{\hat{\Omega}_m}(0)\exp(-\sigma\,s)\right\rangle_X &= \frac{A_D\,\bar{T}_D\,I_Y + (A_B\,\bar{T}_B + A_D\,\bar{T}_D)\,I_Z}{A_D + A_B + A_D}\\ &= \frac{\beta}{2}\,T_{-Y,+X}\,I_Y + \left(1 - \frac{\beta}{2}\right)T_{-Z,+X}\,I_Z,\end{aligned} \tag{47}$$

where the quantities $\beta/2$ and $(1-\beta/2)$ are fractional area weighting factors that sum to unity and represent the contributions of the input faces to the output from a given output face. The weights for each output face are given as a function of the appropriate standard scenario input faces in table 3. Of course, transformations must be made to translate these results into terms useable for non-standard scenarios.

Table 3. Input face weight values for the standard scenario

Output Face Type	X Input Weight	Y Input Weight	Z Input Weight
X	0	$\beta/2$	$(1-\beta/2)$
Y	$\alpha/2$	0	$(1-\alpha/2)$
Z	$\alpha(1-\beta/2)$	$\beta(1-\alpha/2)$	$(1-\alpha)(1-\beta)$

2.5.4 Mean Illumination Factors

We have thus far developed a mechanism for evaluating all the terms in the average equation of transfer between input and output faces except for the volume-averaged limiting path radiance, $L_{\hat{\Omega}_m}$. The limiting path radiance (L) is the sum of blackbody (B), scattering source (J), and direct contributions. In considering the computations needed to evaluate the radiative transfer equation, we first acknowledge that J, as given in Eq. (10), is a positionally varying quantity. But, I is not known except as wall-average values. We are thus limited according to the granularity of the volume resolution used. Further, since the phase function reflects the results of single scattering, rather than posit a complicated model for I's behavior within the volume, to first order it is postulated that the scattering due to a given input stream is dependent on only the mean unscattered illumination provided by that stream and the medium within a given cell. The determination of this mean value requires a set of integrals similar to those used to determine the mean transmittances. These quantities are produced by integrating over the scattering volume swept by energy passing through geometries identical to those considered during the transmittance discussion.

For each type region, the unscattered illumination present at a certain depth within the material is equal to $\exp(-\tau w)$, where τ is the maximum optical depth across the cell for that material and for that stream, and where w is the fractional distance of that point into the material compared with the maximum optical depth presented by that material for that stream.

For region A, the mean illumination can be related to an integral over a cubic region where the optical depth is measured into the material along a single axis. A unit volume is used because the optical depth along the w axis is measured such that at distance 1 the maximum optical depth is reached. Along the other axes, the averaging process eliminates any dependence on actual region size. Additionally, this geometric integral is possible due to the assumption of uniform initial radiance of the incident stream across the input face. These

considerations lead to the formula,

$$, A = \frac{\int\limits_0^1 du \int\limits_0^1 dv \int\limits_0^1 \exp(-\tau w)\, dw}{\int\limits_0^1 du \int\limits_0^1 dv \int\limits_0^1 dw} = \frac{e^{-\tau} - 1}{-\tau} = G_1(\tau). \tag{48}$$

For B and C type areas, the following integral can be used. In this integration, the u axis denotes the direction of decreasing wedge thickness.

$$, B = , C = \frac{\int\limits_0^1 du \int\limits_0^1 dv \int\limits_0^{1-u} \exp(-\tau w)\, dw}{\int\limits_0^1 du \int\limits_0^1 dv \int\limits_0^{1-u} dw} = \frac{e^{-\tau} - (1 - \tau)}{\tau^2/2} = G_2(\tau), \tag{49}$$

For type D areas, the integral is performed over a pyramidal shaped volume. The thickest portion of this region is at $u = 0$, $v = 0$ in the following integral.

$$, D = \frac{\int\limits_0^1 du \int\limits_0^u dv \int\limits_0^{1-u} \exp(-\tau w)\, dw}{\int\limits_0^1 du \int\limits_0^u dv \int\limits_0^{1-u} dw} = \frac{e^{-\tau} - (1 - \tau + \tau^2/2)}{-\tau^3/6} = G_3(\tau), \tag{50}$$

These , functions are unitless and relate to the relative mean illumination (radiance) provided by flux entering the volume segment of interest. To produce overall average illumination in the cell due to flux flowing across a given input face, the 'standard' model is again referred to. We denote the relevant volumetric mean illuminations due to incident radiances I_X, I_Y, and I_Z (passing through the standard input faces X, Y, and Z of the volume, respectively) by the quantities $\overline{I_X}$, $\overline{I_Y}$, and $\overline{I_Z}$. These means are computed based on weighted averages of the mean illumination of the volume type illuminated [Eqs. (48) through (50)], multiplied by the fraction of the total volume contained within each volume segment. The segment volumes associated with each of the region types are given in table 4.

Table 4. Segment volumes for subcomponents of input region types

Region Type	Region Volume
A	$(1 - \alpha)(1 - \beta)\Delta^3$
B	$\alpha(1 - \beta)\Delta^3/2$
C	$(1 - \alpha)\beta\Delta^3/2$
D	$\alpha\beta\Delta^3/3$

For the resulting mean illuminations, one then obtains (after dividing by the total volume Δ^3):

$$\overline{I_X} = ,_X I_X = \alpha \left\{ \delta \frac{G_2(\tau)}{2} + \beta \frac{G_3(\tau)}{3} \right\} I_X, \tag{51}$$

$$\overline{I_Y} = ,_Y I_Y = \beta \left\{ \gamma \frac{G_2(\tau)}{2} + \alpha \frac{G_3(\tau)}{3} \right\} I_Y, \tag{52}$$

and

$$\overline{I_Z} = ,_Z I_Z = \left\{ \gamma \, \delta \, G_1(\tau) + [\beta \, \gamma + \alpha \, \delta] \frac{G_2(\tau)}{2} + \alpha \beta \frac{G_3(\tau)}{3} \right\} I_Z. \tag{53}$$

The total mean illumination within the scattering volume for a given stream is then just the sum of the mean illuminations over the appropriate three input faces for that stream. Due to the symmetrical structure of the streams in different octants, it is possible to generate $,_X$, $,_Y$, and $,_Z$ values according to stream type and make appropriate transformations to convert the input stream information from the proper input faces into the mean illumination statistics for the cell.

Based on the mean illumination for a given stream, we may then determine the amount of flux subsequently scattered into each stream leaving the volume from each face, and thus assess the total flux leaving the cell due to volumetric scattering.

2.5.5 8-Stream Example

To illustrate the development to this point, consider an 8-stream DOM model. In this model, $|\mu| = |\eta| = |\xi| = 1/\sqrt{3}$. Hence, $\alpha = \beta = 1$. Because of model symmetries, all eight streams can be characterized by transformations on the one unique standard stream direction in the first octant.

As each input stream enters through a particular input face, a portion of the entering flux will transmit directly to two output faces, to each of which half the streaming flux is directed. The transmittance to each output face is $G_2(\tau)$, where $\tau = \sqrt{3}\sigma\Delta$. On each output face, Q, four streams are directed outward through it. Each of these output streams has a mean emittance factor of $(1 - T_Q) = [1 - G_2(\tau)]$. Thus, the single scattered flux emitted by a particular stream on a given face is proportional to $[1 - G_2(\tau)]$.

For each stream m, the volume averaged radiance is

$$\overline{I_m} = G_3(\tau) \frac{(I_X + I_Y + I_Z)}{3}. \tag{54}$$

Each input stream scatters flux into all eight output streams. Each stream makes a cosine of 1 with itself, -1 with the stream in the opposite octant, 1/3

with three streams, and -1/3 with the three remaining streams. Let these cosines be represented by the variable μ_{ms} (cosine of the scattering angle), and represent the modeled phase function value for this scattering angle by $\tilde{P}(\mu_{ms})$. For the moment ignoring emissive effects, the influence of input stream m on a specific outward flowing stream s is computed using the volume averaged radiance and the phase function value. Now, if we designate the scattering source in this direction as J_{ms}, then from Eq. (21) we have,

$$J_{ms} = \varpi \, \frac{4\pi w}{8} \, \tilde{P}(\mu_{ms}) \, \overline{I}_m.$$ (55)

Here, the angular weight factor w equals 1 for all 8-stream cases. This source term can then be used to determine input stream m's effect on all scattered flux exiting the three output faces corresponding to stream s. Let E_{ms} be the net flux exiting the volume due to J_{ms}:

$$E_{ms} = 3 \frac{1}{\sqrt{3}} \frac{4\pi w}{8} [1 - G_2(\tau)] \Delta^2 \, J_{ms},$$ (56)

where the 3 represents the contributions on the three output faces, $1/\sqrt{3}$ is each output stream's cosine with each output face normal, $4\pi w/8$ appears due to the integration over solid angle on the output face, and $[1 - G_2(\tau)]$ is the emittance factor. The units of E_{ms} are $W/\mu m$. Summing over all exiting streams, the total flux streaming out of the volume due to scattering source J_{ms} is:

$$E_S = \sum_s E_{ms} = \frac{3}{\sqrt{3}} \frac{4\pi}{8} [1 - G_2(\tau)] \Delta^2 \, \varpi \, G_3(\tau) \overline{I_m} \sum_s \frac{4\pi}{8} P(\mu_{ms}).$$ (57)

Due to the discrete ordinates method chosen, the sum over scattering angles can be divided into individual sums over each Legendre component. These sums cancel for all but the isotropic term, which sums to unity. Thus through cancellation we obtain:

$$E_S = \varpi \, \Delta^2 \, \frac{1}{\sqrt{3}} \frac{4\pi}{8} [1 - G_2(\tau)] G_3(\tau) (I_X + I_Y + I_Z).$$ (58)

Similar computations can be made for the total transmitted (E_T) and total incident fluxes (E_I) due to this stream (again taking account for the finite solid angles associated with the streams as they enter and exit the volume):

$$E_T = \Delta^2 \, \frac{1}{\sqrt{3}} \frac{4\pi}{8} G_2(\tau) (I_X + I_Y + I_Z),$$ (59)

and

$$E_I = \Delta^2 \, \frac{1}{\sqrt{3}} \frac{4\pi}{8} (I_X + I_Y + I_Z).$$ (60)

38

To evaluate the fractional flux accounted for via transmittance and volumetric scattering and absorption, E_S is divided by the single scattering albedo to account for absorbed and scattered radiation. This result is added to E_T, and the sum is divided by the incident flux. The result is:

$$\Lambda(\tau) = \frac{E_S/\varpi + E_T}{E_I} = G_2(\tau) + G_3(\tau) - G_2(\tau)G_3(\tau)$$
$$= 1 - [1 - G_2(\tau)][1 - G_3(\tau)]. \tag{61}$$

This function is plotted in figures 8 and 9. These figures show the behavior of $\Lambda(\tau)$ as a function of increasing cube axial optical depth ($\sigma\Delta$). From the plots, it is clear that the volume based equations are reasonably accurate for $\tau \ll 1$, since in the limit of $\tau = 0$ the curve has slope zero and equals unity, accounting for all the flux. For large τ the approximation is progressively more lossy.
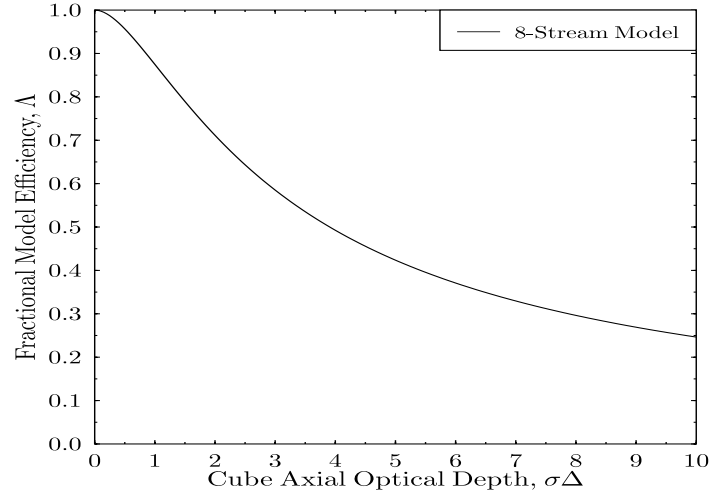
Figure 8. Fractional flux accounted for in 8-stream model using volumetric effects.

The main point to keep in mind, though, is not that these calculations indicate that there are problems for high optical depth – indeed there are problems – but these are problems that are common to every strictly volume-based equation set. The conclusion is that volume-based equations alone cannot account for all the scattered and transmitted energy.

Cases of higher order quadrature sets exhibit similar behavior to the 8-stream curve shown here, since the limitation is not in the number of streams but due to the single scattering approach taken to model the scattering phenomenon. Nevertheless, these results can be shown to preserve more accuracy than the low-density approach since the transmittance factors are at least being computed
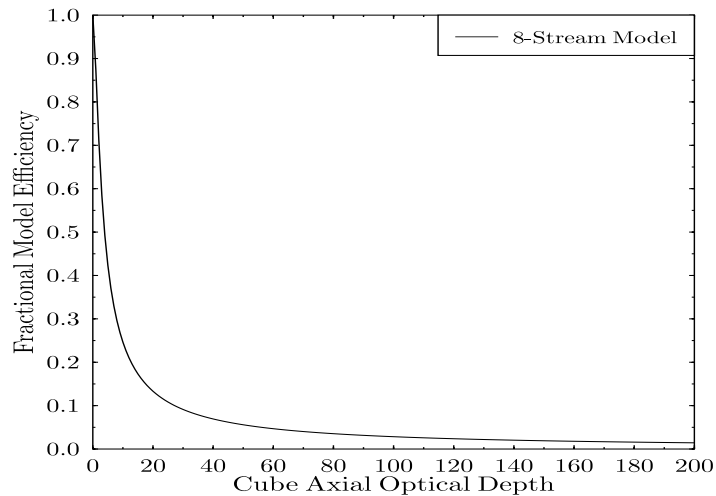
Figure 9. Fractional flux accounted for in 8-stream model using volumetric effects. Plot of high optical depths.

exactly, and we are making our single scattering calculation based on a true volume average of the radiance for each stream. The low-density equations fail by approximately 1 optical depth. These equations perform well up to and exceeding 1 optical depth, but they do not fair well beyond about 4 optical depths.

Hence, the most critical factor limiting the use of the pure volumetric approach obtained thus far is due to the nature of the atmosphere itself: at visible wavelengths natural cloud optical depths are often hundreds of optical depths thick. For a 3D-RT simulation of an atmospheric volume containing even a simple cumulus cloud, the method described to this point would still require millions of cells to adequately maintain flux balance via purely volumetric effects.

2.5.6 Surfacelike Interactions

To augment the technique developed thus far enabling it to treat large optical depth conditions, it is postulated that any missing energy can be accounted for by using surface-like scattering and absorption events. This hypothesis can be justified based on the following two empirical arguments. First, consider a stream of energy directed perpendicular to a face of entry into a volume element. At high optical depths, negligible energy propagates unscattered through the volume, and the mean unscattered radiance rapidly approaches zero as one moves further into the volume. Physically, this means that virtually all the energy is interacting with the media within a short distance of the input face. This scenario would produce near-zero transmission and illumination factors (resulting in a near-zero volumetric efficiency factor Λ), and virtually all the energy would be scattered or absorbed at or near the surface. In a second

thought experiment, consider a stream that enters the volume at an incidence angle which is nearly tangent to the input face. In this case, we do not care how thick the media is, but only consider the cell averaged illumination produced. Because the cosine of the incident stream is so small, the fractional volume illuminated by the stream is very small, and thus whatever scattering does occur must occur within a short distance of the entry face. In either case, then, a volumetric scattering model is inappropriate. Thus, it is argued that any energy not seen when accounting for transmittance and volumetric diffuse scattering and absorption can be modeled with a surfacelike scattering/absorption process.

To characterize the amount of energy to be recovered due to surface effects in the 8-stream example, we would need to allow fractional energy in the amount $[1 - G_2(\tau)][1 - G_3(\tau)]$ to interact at the surface of the medium for each incident stream. Let us characterize this fractional surface interaction with the parameter $S(\tau) = [1 - \Lambda(\tau)]$. For stream models beyond S_2 the form of these S expressions will also depend on the stream index and the particular input face being considered. However, for the 8-stream model we have a simple expression that is the same for all streams and all faces. For a more complicated scattering model, we turn to the next most complicated case, the 24-stream S_4 quadrature.

2.5.7 24-Stream Example

For the S_4 case using the LSE quadrature (Fiveland (1991); Lewis and Miller (1984)), each stream is composed of two components with magnitudes of $a = 0.3500212$, each, and one component with magnitude $b = 0.8688903$. Thus, $\alpha = a/b = 0.4028370 = \beta$. This results in a slightly more complex equation set than produced for the S_2 set. Let us define $\gamma = 1 - \alpha = 0.5971630$. Then, (suppressing G function dependencies on τ),

$$\overline{I}_m = \left[\alpha\gamma\frac{G_2}{2} + \alpha^2\frac{G_3}{3}\right](I_X + I_Y) + \left[\gamma^2 G_1 + 2\alpha\gamma\frac{G_2}{2} + \alpha^2\frac{G_3}{3}\right]I_Z. \qquad (62)$$

The scattering source term (J_{ms}) for this case is the same as given in Eq. (55), except that $w = 1/3$ for each stream under S_4. It then remains to determine the energy exiting all three output faces for this stream. Notice that two of the output faces have stream cosines of a and a mean transmittance value that is different from that for the third output face. These considerations lead to the expression,

$$E_{ms} = b\frac{\pi}{6}L(\tau)\varpi\,\Delta^2\,\frac{\pi}{6}\,\tilde{P}(\mu_{ms})\overline{I}_m, \qquad (63)$$

where

$$L(\tau) = 1 + 2\alpha - \gamma^2 G_0(\tau) - 4\alpha\gamma G_1(\tau) - 3\alpha^2 G_2(\tau). \qquad (64)$$

Due to the symmetries of the S_4 case, the scattered energy as a function of direction only depends on $\tilde{P}(\mu_{ms})\overline{I}_m$, since the remaining factors are only dependent on τ. Thus, again, E_{ms} is summed over all scattering directions, and as before, only the zero-th order Legendre polynomial has a nonzero

contribution, such that the total volumetric diffuse scattering produces an output energy of,

$$E_S = \Delta^2 b \frac{\pi}{6} L(\tau) \varpi \overline{I} = \Delta^2 b \frac{\pi}{6} \left[L(\tau) \varpi \overline{I} \right], \tag{65}$$

which depends on only the incident energy and the optical depth of the medium. Similarly, the incident energy and the transmitted energies only depend on the optical depth, as,

$$E_I = \Delta^2 b \frac{\pi}{6} \left[\alpha \left(I_X + I_Y \right) + I_Z \right], \tag{66}$$

$$E_T = \Delta^2 b \frac{\pi}{6} \left[T_a(\tau) \alpha \left(I_X + I_Y \right) + T_b(\tau) I_Z \right], \tag{67}$$

where

$$T_a(\tau) = \gamma G_1(\tau) + \alpha G_2(\tau); \tag{68}$$

$$T_b(\tau) = \gamma^2 G_0(\tau) + 2\alpha\gamma G_1(\tau) + \alpha^2 G_2(\tau). \tag{69}$$

Combining terms, the net energy unaccounted for via transmission and volumetric scattering can be expressed as,

$$E_I - E_T - E_S/\varpi = \Delta^2 b \frac{\pi}{6} \left[\alpha \left(I_X + I_Y \right) \left[1 - \Lambda_a(\tau) \right] + I_Z \left[1 - \Lambda_b(\tau) \right] \right], \tag{70}$$

$$\Lambda_a(\tau) = L(\tau) \left[\gamma \frac{G_2(\tau)}{2} + \alpha \frac{G_3(\tau)}{3} \right] + T_a(\tau), \tag{71}$$

$$\Lambda_b(\tau) = L(\tau) \left[\gamma^2 G_1(\tau) + 2\alpha\gamma \frac{G_2(\tau)}{2} + \alpha^2 \frac{G_3(\tau)}{3} \right] + T_b(\tau). \tag{72}$$

The terms $\Lambda_a(\tau)$ and $\Lambda_b(\tau)$ represent the fractional efficiencies of the scattering model, as plotted in figure 10. Standard input X- and Y-type faces (those where the cosine of incidence is a) are handled using $S_a = 1 - \Lambda_a(\tau)$, and Z-type input faces (those with a cosine of incidence of b) are treated using $S_b = 1 - \Lambda_b(\tau)$, where these S factors are used as the fractional amount of energy arriving at a surface that must be scattered/absorbed in a surfacelike event to maintain energy conservation.

The different scattering efficiencies arise because the cosine of incidence results in different mean path lengths through the media depending on the surface of entry. For the 24-stream case, one of two angles of incidence are possible. For the 'b' case, there is a greater average illumination within the volume, but this is offset by the lower average transmittance. The net result is that $\Lambda_b(\tau)$ has a uniformly lower efficiency than the result obtained for the S_2 order case. This result is obtained even after accounting for the larger τ in the S_2 case ($\tau_2 = \sqrt{3}\sigma\Delta$ versus $\tau_4 = \sigma\Delta/0.8688903$).

Interestingly, the $\Lambda_a(\tau)$ curve resembles the behavior of the single S_2 case curve. Perhaps because the Λ_a curve represents a smaller cosine with the entry surface, while the transmittance is increased, the path radiance is reduced, and the overall performance roughly tracks that of the S_2 order case. The net effect is a similar behavior (in terms of overall efficiency) of the 24-stream case to the 8-stream case.
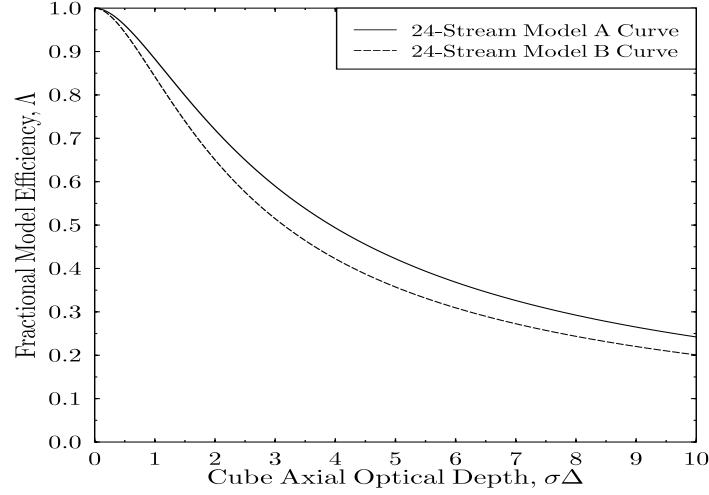
Figure 10. Fractional efficiencies of the 24-stream model using volumetric effects. The 'A' curve represents the Λ_a function, while the 'B' curve is the Λ_b function.

2.5.8 48-Stream Case and Beyond

Beyond the 24-stream case, there are increasing numbers of equations required to account for the efficiencies of each scattering stream. For the 48-stream approximation there will be four independent accounting expressions: two for each of the two unique weighting structures. In the 80-stream case there are three unique weighting structures. The first of these has two unique curves; the second has three unique curves since each component is a different weight; and in the third case there is one unique curve, since all components are equal. There are thus a total of six formulas to evaluate. Obviously, any economies to be gained through symmetry would be rather limited compared to the added complexity of the handling routines once a high order Legendre expansion model is chosen.

2.5.9 Accounting for the Missing Flux

Given that the means of accounting for missing flux is through surfacelike interactions, how should one approach the problem of correcting the radiance values to restore the missing flux? As a sample case, let us consider radiance arriving at an X-type interface in the 24-stream case (cosine of incidence with the surface normal is $\mu_m = a$).

We have already decided that the amount of flux to be scattered at such a surface ($E_{SX,m}$) should be proportional to $S_a(\tau)$ and the incident flux. We also know that the scattering process itself is proportional to the single scattering phase function $\tilde{P}(\mu_{ms})$, since we are working in a single scattering paradigm. And recall that $\hat{\Omega}_m$ and $\hat{\Omega}_s$ are the incident and scattered radiance

43

propagation vectors, respectively. Also we assume that $E_{SX,m}$ can be related to some fraction, $\vartheta_{X,m}$, of the overall radiance falling on that surface. These considerations lead to the equation:

$$E_{SX,m} = \frac{4\pi w_m}{8} |\mu_m| \Delta^2 \vartheta_{X,m} I_{X,m}, \tag{73}$$

where $I_{X,m}$ is the mean incident radiance at that face for stream m.

Since we assume the surface scattered radiance ($I_{SS,s,m}$) at this interface equals

$$I_{SS,s,m} = \varpi \, \vartheta_{X,m} \, I_{X,m} \, (4\pi w_m/8) \, \tilde{P}(\mu_{ms}), \tag{74}$$

then the total flux scattered at the surface due to stream m will be,

$$E_{SS,m} = \Delta^2 \sum_s \frac{4\pi w_s}{8} |\mu_s| I_{SS,s,m} = \varpi \frac{E_{SX,m}}{|\mu_m|} \sum_s |\mu_s| \frac{\pi w_s}{2} \tilde{P}(\mu_{ms}). \tag{75}$$

One can easily verify that this result actually does disperse the correct amount of flux in the 8-stream conservative isotropic scattering case (where $\tilde{P}(\mu_{ms}) = (4\pi)^{-1}$) case. Here we have $w_m = w_s = 1$, $|\mu_m| = |\mu_s| = \mu$, $\varpi = 1$, $s = 1 \ldots 8$. The result of the summation in Eq. (75) is then just μ, and the net equation shows that $E_{SS,m} = E_{SX,m}$.

In general, the results can be characterized by,

$$E_{SS,m} = \varpi \, E_{SX,m} \sum_s \frac{|\mu_s|}{|\mu_m|} \frac{4\pi w_s}{8} P(\mu_{ms}) = \varpi \, K_{X,m} \, E_{SX,m}. \tag{76}$$

The terms $K_{X,m}$ thus represent an integration efficiency over the input face,

$$K_{X,m} = \sum_s \frac{|\mu_s|}{|\mu_m|} \frac{4\pi w_s}{8} P(\mu_{ms}). \tag{77}$$

Similar coefficients will exist for Y-type and Z-type surfaces. Optimally, one would expect the $K_{X,m}$, $K_{Y,m}$, and $K_{Z,m}$ terms all to equal unity, but due to the choice of the symmetry set and peculiarities of the phase function representation itself, suboptimal conditions may exist. In our example, then, the total flux dispersed at the X-type interface is modeled as $K_{X,m} E_{SX,m}$.

Returning now to the calculation of flux unaccounted for due to volumetric effects, let us generalize equations such as Eqs. (71-72) and (61), where we let (for example) $1 - \Lambda_{X,m}$ be the fractional flux on input face type X of stream m that must be accounted for via surface effects. Comparison between the development above and results such as Eq. (71) shows we must have $\vartheta_{X,m} K_{X,m} = 1 - \Lambda_{X,m}$; that is,

$$\vartheta_{X,m} = \frac{1 - \Lambda_{X,m}}{K_{X,m}}. \tag{78}$$

The net result is that at a given output surface and for a particular output stream, the total surface scattering contribution to that stream is determined by summing over all streams at that surface. The fractional contribution of each stream will depend on the $\Lambda_{X,m}$ value for each input stream. Continuing the X-type surface example we have,

$$\delta I_{S,X,s} = \sum_m \varpi_m \frac{4\pi w_m}{8} \vartheta_{X,m} \tilde{P}_m(\mu_{ms}) I_{X,m}. \tag{79}$$

This surface incremental portion is then added to the transmitted and volumetric scattered flux computed via the methodology described previously. Note that ϖ is considered a function of the stream (as are ϑ and P) because the behavior of a given stream at a given surface depends on the direction in which the input stream is flowing across the surface (which volume element the stream is entering), regardless of the directionality of the output stream.

2.6 Direct Radiation Considerations

The previous section assumed the radiance of diffuse streams was constant over any input face of interest. This assumption allowed the 'simple' forms for transmission, emittance, and surface scattering fraction to be derived analytically in the cases studied.

However, this assumption may not be reasonable for direct (solar/lunar) radiation, due to the relative dominance of direct sources of energy at visible wavelengths. Typical boundary conditions for a 4-km high atmospheric volume yield direct spectral irradiances on the order of 1200 to 1400 W/m^2-μm in the visible, while the diffuse spectral radiances are on the order of 30 to 100 W/m^2-μm-sr. The differences in importance between these two sources indicates a distinction should be made in processing these for radiative transfer calculations. For example, Zardecki (1995) proposed a separate LOS computation to trace the optical depth of direct illumination reaching the center of each cell in his radiative transfer algorithm.

2.6.1 Cell Face and Volume-Averaged Illuminations

In the surface-based model discussed here, it would not be appropriate to trace lines of sight to a cell center but rather to evaluate the average illumination on each of the three direct radiation input faces to each cell. This can be accomplished by sampling over each of these surfaces and forming an average transmittance between the modeled volume upper boundary (assuming the Sun or Moon are the only direct sources considered) and the specific cell wall. In addition, one can determine the mean illumination provided to the cell by knowing the path length that each sampled pencil of light traces out as it passes through the cell. Integrating over each input surface, one can determine the efficiency of direct radiation entering each face of each volume element. This

indicates the fraction of direct energy scattered at each surface. From these calculations, one may determine the net direct surface scattering source term at each face within the volume.

Let the azimuth and zenith angle to the source of direct radiation be specified by ϕ_0 and θ_0, respectively. Then the direction of propagation of the direct illumination is

$$\widehat{\Omega}_0 = \{-\sin(\phi_0)\sin(\theta_0), -\cos(\phi_0)\sin(\theta_0), -\cos(\theta_0)\}. \tag{80}$$

Here note that the azimuth angle is given in geographical units measured from the North (the Y-axis) and increasing toward the East (X-axis).

For each cell, there will be at most three surfaces exposed to direct radiation (we ignore the finite solid angle subtended by the source and treat it as plane parallel energy). A series of ray traces from different sample points on the surface upward to the volume boundary are made for each of the three faces to determine the average transmittance of direct radiation through the volume to these surfaces.

For each sample point on a cell, i, there will be a net transmittance starting at the overall volume's upper boundary and continuing through the volume to the cell wall of interest. Call this transmittance factor $T_{in,i}$. Secondly, there will also be a distance that unscattered energy arriving at this sampling point would travel to reach an exit side of the cell volume in question (D_i). If the sample volume has an extinction coefficient σ, then the direct radiation exiting the volume through this pencil of light will experience a total transmittance of,

$$T_{out,i} = T_{in,i}\exp(-\sigma D_i). \tag{81}$$

The mean illumination provided to the volume by this pencil of light will depend on the number of samples N taken over the input face, the face area Δ^2, and the cosine of the pencil with the surface normal (call this $|\mu_0|$), $T_{in,i}$, and $T_{out,i}$.

The volume illuminated by the pencil (V_i) will be

$$V_i = D_i\,|\mu_0|\,\Delta^2/N. \tag{82}$$

The average value of the illumination due to this pencil of illumination will then be

$$\overline{A}_{0,i} = \frac{A_0}{|\xi_0|}\,\frac{[T_{in,i} - T_{out,i}]}{\sigma D_i}\,\frac{D_i|\mu_0|\Delta^2/N}{\Delta^3} = \frac{A_0}{N}\,\frac{[T_{in,i} - T_{out,i}]}{\sigma\Delta}\,\frac{|\mu_0|}{|\xi_0|}, \tag{83}$$

where the illumination over each sample is averaged over the full volume (Δ^3), and where A_0 is the boundary irradiance (W/m^2-μm) which has an implicit multiplication by $|\xi_0|$ (the cosine of $\widehat{\Omega}_0$ with the vertical). The total illumination

provided to the cell via this input surface is then found by summing over all sample illumination components:

$$\bar{A}_0 = \sum_{i=1}^{N} \overline{A}_{0,i}. \tag{84}$$

In the computer implementation of this approximation, computations over each input face are made at successively higher N values until the solution settles to a stable result. The results of these calculations are the mean illumination to each cell due to each input surface ($\bar{A}_0$), the mean transmittance to each cell surface,

$$\overline{T}_{in} = \frac{1}{N} \sum_{i=1}^{N} T_{in,i}, \tag{85}$$

and the mean transmittance to the far side of the cell due to energy passing through each input surface,

$$\overline{T}_{out} = \frac{1}{N} \sum_{i=1}^{N} T_{out,i}. \tag{86}$$

Given that the direct radiation is modeled as an irradiance (energy per square area perpendicular to the vertical vector, which we then transform into a result appropriate to a plane perpendicular to the direction of propagation by dividing by ξ_0) with a directionality in the form of a delta function in the direction of propagation, then the scattering into some output stream is proportional to $P(\hat{\Omega}_j, \hat{\Omega}_0)$. Also, similar to the results obtained for the diffuse method, one may integrate over all output streams over every face of the volume element to obtain the net energy scattered due to input direct radiation entering along a given input face. The mathematics of this process are similar to those of the diffuse case and will not be repeated here, but the results are similar. Each face can be assigned a particular efficiency factor (Λ_0) indicating the amount of energy that must be scattered via a surface process proportional to $(1-\Lambda_0)$. We thus have an accounting method for volumetric and surface-based contributions of direct radiation to the diffuse streaming radiances.

2.6.2 Earth Curvature Considerations

One consideration of particular significance to direct radiation calculations is how to account for the Earth's curvature. For highly oblique angles of incidence of direct light (near Sunset/Moonset or Sunrise/Moonrise), the effects of the curved Earth become significant. How does one trace a path through the volume of near-infinite length when the Sun is at nearly 90° zenith angle? In particular, it is advantageous when running the radiative transfer model to impose horizontal periodicity on the modeled volume. This means potentially

tracing through many copies of the same volume in tracing a line of sight toward the Sun.

To avoid the possibility of infinite loops, two steps are taken in the computer model. First, the code is only callable from its front end processing program if the Sun or Moon is above the horizon. Second, a correction is made to account for the curvature of the Earth when ray tracing. This correction is based on a parabolic approximation of the earth's shape where it is assumed that the modeled region dimensions are small with respect to the radius of the Earth.

For this development, we let the nominal radius of a spherical Earth be fixed at $R_E = 6371$ km. To determine the amount of correction to be made at each step in the ray tracing process, one can imagine an observer at height z above sea level observing the Sun in an initial direction $-\widehat{\Omega}_0 = \{-\mu_0, -\eta_0, -\xi_0\}$. This scenario is shown in the diagram in figure 11.
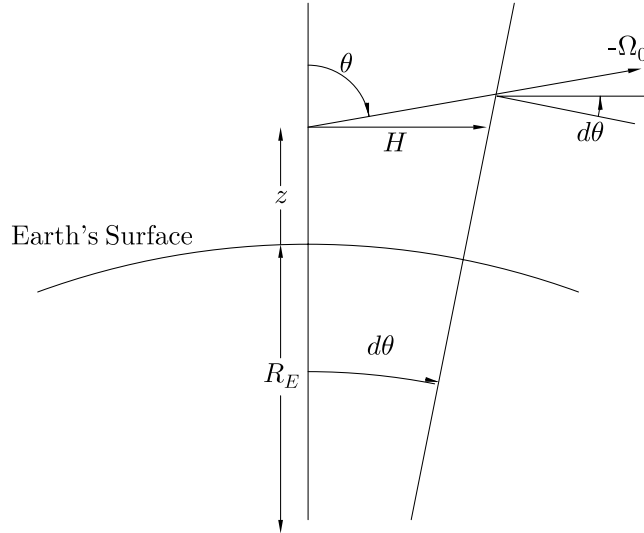
Figure 11. Modification of the solar zenith angle with respect to the gravity vector upon stepping along a path out of the atmosphere in the direction of the direct source.

Let us now place an observer a distance z above the Earth's surface and let us define an Earth centered coordinate system; call it X_0. We can then always draw the x and y axes such that the observer position is at the x-y origin: (0, 0, $z + R_E$). We now step a distance D along a line of sight in the direction of the Sun to point $(-\mu_0 D, -\eta_0 D, -\xi_0 D + z + R_E)$. Now, define the horizontal distance, H, moved across the Earth's surface during this step along the line of sight:

$$H = D\sqrt{\mu^2 + \eta^2}.$$

The new location will be a fraction of an Earth radius away from the original point and thus will have a different direction for its gravity vector.

We have already seen the relationship between $\widehat{\Omega}_0$ and the zenith angle θ_0. At this new point we can again place an observer a height z' above the surface in a new Earth centered coordinate system X'. To first order this new height will be

$$z' = z - \xi_0 D. \tag{87}$$

But, due to the shift in position across the Earth's surface, and the consequent change in the direction of the gravity vector, the zenith angle to the Sun will be modified to

$$\theta_0' = \theta_0 - H/(z + R_E).$$

Therefore, the apparent elevation angle of the Sun must be modified continuously along the line of sight to simulate this change in direction with respect to the gravity vector at each point. Here we assume that over the span of the particular scattering volume of interest the change in the zenith angle is so small that it can be neglected in terms of propagation code accuracy, and that we may begin each trace using the same angle.

The scattering volumes to be studied are actually quite small with respect to this curvature, so the effects of this correction are only truly important when computing $T_{in,i}$ for a scattering model employing horizontally periodic boundary conditions. For example, consider a scattering volume that is 4 km on edge horizontally and 4 km thick vertically. Assume an observer at zero height views the Sun at the horizon (arguably a worst case). Then, for each pass through the scattering volume we would have,

$$d\theta_0 \approx -\frac{4}{6371} = -0.6278 \text{ mrad.}$$

This result, in milliradians, may appear very small, yet the cumulative effect is such that the line of sight is 5 km above the surface within 250 km, and 20 km above the surface within 500 km. This indicates that we have bounded our problem, but improvements can be made.

2.7 Output Face Calculations

The expressions obtained thus far exhibit energy conservation. They also exhibit what is believed to be the proper behavior of the scattered energy in volumetric or surface-based terms in that the modeled energy is distributed according to radiance by direction such that it is proportional to the phase function. But, it remains to cast these results as they relate to the output face diffuse radiances.

To proceed, we formulate an equation set that accounts for all the energy that should contribute to each output stream. The components are: (1) diffuse transmitted energy from each of the three appropriate input faces, (2) volumetric diffuse scattering based on average volume radiance for each stream, (3)

volumetric black body emittance, (4) surface-based scattering of energy from all diffuse streams arriving at the given face, (5) volumetric scattering of direct irradiance energy based on volume averaged irradiance, and (6) surface-based scattering into the given stream. This step is termed the iteration on the scattering source (Zardecki (1995); Lewis and Miller (1984)), where at the nth stage of the process the diffuse energy incident at a cell's boundaries may be viewed as the total diffuse radiance resulting from $(n-1)$ scatterings.

For example, if we consider an output X-type face for stream s propagating into the first octant, we have,

$$I_{out,X,s} = I_{T_{out},X,s} + (1 - \bar{T}_{X,s}) L_s + \delta I_{S,X,s}, \tag{88}$$

where $I_{T_{out},X,s}$ is the transmitted radiance,

$$
\begin{aligned}
I_{T_{out},s} &= W_{X,X,s} T_{-X,+X} I_{in,X,s} \\
&+ W_{Z,X,s} T_{-Z,+X} I_{in,Z,s} \\
&+ W_{Y,X,s} T_{-Y,+X} I_{in,Y,s}.
\end{aligned} \tag{89}
$$

Here the W's are areal weighting factors introduced in table 3. The term $\delta I_{S,X,s}$ represents the surface scattering contributions of both direct and diffuse scattering for an X-type output surface for stream s.

And lastly, the limiting path radiance L_s is

$$L_s = \varpi \frac{\pi}{2} \sum_m w_m \tilde{P}(\mu_{ms}) \bar{I}_m + B + \varpi \tilde{P}(\mu_{0s}) (\bar{A}_{0X} + \bar{A}_{0Y} + \bar{A}_{0Z}), \tag{90}$$

where $\mu_{ms} = \hat{\Omega}_m \cdot \hat{\Omega}_s$, $\mu_{0s} = \hat{\Omega}_0 \cdot \hat{\Omega}_s$ for the direct radiation scattering, and where the $\bar{A}$ terms are the mean volume illuminations due to direct energy entering through the x, y, and z input face for direct radiation. Similar expressions apply for streams travelling in other octants and out other types of faces.

In conclusion, the analysis leading to Eq. (88) began at the end of section 2.5.4, where we were looking simply for an expression for the limiting path radiance, L_s. But, we found that the volumetric method alone could not account for all the energy. Further consideration of the problem led to a surface-based correction and a means of treating direct radiance effects. We thus now have a full theoretical description of the scattering, emission, and absorption process. We then conclude this chapter with a brief description of the computer implementation of this theory.

2.8 The Atmospheric Illumination Module

The Atmospheric Illumination Module (AIM) is a computer implementation that runs the radiative transfer model described in the previous sections to characterize a portion of the lower atmosphere. AIM is thus an interface that runs the RT code at various wavelengths, sets up the input, and postprocesses the code output. The actual RT code which was described previously has been named BLITS (Boundary Layer Illumination and Transmission Simulation). The AIM routine is designed to run BLITS in several different modes. These modes primarily are designed to speed its execution, but also to permit greater flexibility in the setting up of run conditions and scenarios that can be processed.

In the immediate predecessor to the AIM/BLITS modeling system, Zardecki's BLIRB model (Zardecki 1995) combined some features of the AIM preprocessing functions in with the radiative transfer modeling stages. That is, BLIRB mixed aerosol and Rayleigh scattering properties within the model itself. Thus, when aerosol properties were specified, they had to be separately mixed for each vertically different layer since the molecular properties varied with height. Each cell was then characterized by a given scatterer type. This allowed indexing of scattering properties by cell position.

This method had to be improved because BLITS requires more information to run than BLIRB. Notice that the low-density transfer Eqs. (26) and (30) require only values of s and σ. And, since s is a function of the stream direction, it is simply computed and stored, and σ is also a single value per cell. But, the BLITS approach requires storage of information on the surface scattering efficiencies (ϑ), the face-to-face and face-averaged transmission factors (various T terms), and the volumetric scattering source factors (, factors).

By moving the cell characterization processing out of the RT model and into a preprocessing stage, it was possible to improve the characterization of the model volume with fewer scattering types. To achieve this preprocessing step, we began from a Legendre expansion point of view. To completely describe a scattering/absorbing/emitting cell, all the properties of the cell are completely described by the quantities: σ and $\varpi\sigma X_\ell$, $\ell = 0 \ldots L$. (X_ℓ is defined in Eq. (19), as modified by the scaling transformation. In general L is set to N, the order of the stream expansion.) Thus, each cell is completely described (for a given wavelength) by a vector of dimension $L + 2$.

Using this 3D set of vectors, the main AIM processor runs a pattern recognition clustering model that groups these vectors into 'classes' of vectors, each describable by a mean vector. Thus, AIM can transmit the mean vector information for each class to the BLITS code along with an index value which assigns each cell to one of the classes. The scattering properties for a given cell are then indexed to the mean vector associated with that class. To perform the processing, initially, all the vectors are grouped into a single class. The clustering algorithm then iterates such that in each pass the class with the greatest variance in its components is divided along the major axis of its greatest

variance components, and two daughter classes are produced. Each sample is then compared against the centroids of each class, and a new class is assigned based on the distance of that sample to the closest class centroid. Once all samples have been reassigned, new centroids and variances for each class can be recomputed based on the current elements of each class. In each iteration, a new class of aerosol is created. That is, a new centroid vector describing aerosol properties in its vicinity is created. This iteration process continues until a user selected maximum number of classes (centroid vectors) is produced, or until there is no more variance in any of the classes. The class identity of each cell at the end of this procedure is then passed to BLITS in order to populate the scattering volume. The mean vector component values for the class centroids are also passed to characterize each scattering aerosol indexed in the volume population table.

The pattern recognition preprocessing stage of AIM thus optimizes the representation of the scattering volume with respect to a series of aerosol classes. These classes allow for a reduction in the total amount of data that must be stored by limiting the transmittance, illumination coefficients, etc. to only those listed according to aerosol classes. However, additional data storage compression is also possible by exploiting symmetries in each class of stored aerosol data. These symmetries arise because each octant of the angular scattering space will have identical transmittance properties between input and output faces. The difference is in the orientation of the input and output faces. Similarly, within a single octant, due to the discrete ordinate technique, the diffuse streams oriented in primarily x, y, and z directions will exhibit similar characteristics for diffuse scattering and transmittance properties.

To exploit these properties, all internal arrays are computed in terms of the so-called standard conditions. This means that all results are computed for the first octant (stream flowing in the positive x, y, and z directions) and oriented such that the z-axis component, ξ, is greater than or equal to either the $x-$ or y-axis components. Results obtained are then accessed by indirect addressing.

Though this system only exhibits a maximum compression factor of 24 for the representation of cell scattering information, it does represent some savings. However, by far the largest contribution to the data requirements for the model are for holding the positional/directional data. Typical runs on a 64 Mb work station entail a $32 \times 32 \times 16$ x-y-z cell structure with 24-stream angular resolution and a factor 3 multiplication to account for stream values at each X, Y, and Z input walls.

3. Monte Carlo Model Comparisons

The purpose of any RT Monte Carlo model is to generate high-accuracy statistics concerning scattering, since the ability to control the scattering effects is greater than that possible by solving the radiative transfer function directly. That is, the ability to describe the phase function is not limited according to the number of streams that must be represented in the results if we are only concerned with flux outputs. Therefore, an In-house Monte Carlo (IHMC) code has been developed to characterize scattering scenarios under various propagation conditions.

The primary difficulty with a Monte Carlo approach is the time required to generate these statistics to a desired degree of accuracy. Since Monte Carlo methods depend on generating statistics which describe the scattering process, photon noise is the controlling factor in determining the number of iterations necessary to produce a statistical solution to a specified degree of accuracy. But, this implies that we would like to know how accurate a statistic is at any point in the solution process so that we know when to stop iterating. We therefore present a method of computing the solution accuracy in section 3.1. Section 3.2 then provides a short description of the model, and section 3.3 discusses model validation tests.

3.1 Assessing Photon Noise Statistics

Due to the weak law of large numbers (c.f. Stark and Woods 1986), the solution with a given number of samples can be tested to determine whether it exceeds a fixed degree of accuracy. With this knowledge, a Monte Carlo code can be easily written that produces resulting statistics to arbitrary accuracy. Of course, higher degrees of accuracy require longer compute times, proportional to the number of samples. Highly scattering ($\varpi \approx 1$) dense media require increased compute times because the number of collisions per photon prior to exiting the volume is a function of the optical depth. Depending on the medium, the number of collisions may be on the order of hundreds per photon for cloud-type aerosols.

The weak law of large numbers states that for a set of independent and identically distributed (IID) random variables (RVs) X_n with mean μ and variance σ^2, if we do not know the mean of this distribution (μ) a priori, we can know that an estimate of the mean, $\hat{\mu}_N = \sum_{n=1}^{N} X_n / N$, will approach the true mean as the number of samples (N) approaches infinity. In our Monte Carlo propagation model, the X_n variables represent sample fluxes exiting through the six walls of the sample volume. These X_n's are created by producing packets of photons, 1000 in each group. For each packet of 1000 photons, we determine how many

exit each wall and divide by the total to produce six statistics. Each of these six is a different random variable, but multiple packets should have IID RVs for each exit wall. Since the mean fluxes from each exit wall is what we are attempting to find, we can produce a sample mean for each wall by averaging the results of multiple packets as above.

The next step in the analysis involves the use of the Chebyshev inequality. Here, we treat μ_N itself as a random variable. According to the weak law of large numbers, the mean of μ_N should be just μ, and the variance is $\sigma^2_{\mu_N} = \sigma^2/N$. The Chebyshev inequality is then invoked, which furnishes a bound on the probability of a random variable deviating from its mean by an amount δ:

$$P(|\mu_N - \mu| \geq \delta) \leq \sigma^2_{\mu_N}/\delta^2. \tag{90}$$

The term $\sigma^2_{\mu_N}/\delta^2$ thus furnishes an upper bound on the extent of the error in estimating the mean. If we then fix the accuracy (A^2) that we desire in the answer, and evaluate δ relative to the value of the sample mean itself ($\delta = \epsilon\,\mu_N$, where ϵ is a fractional accuracy required, assuming $\mu_N > 0$), then we know that we can ensure a given level of accuracy in our solution by requiring:

$$P(|\mu_N - \mu| \geq \delta) \leq \sigma^2_{\mu_N}/\delta^2 = \frac{\sigma^2}{N\,\epsilon^2\,\mu_N^2} \leq A^2. \tag{91}$$

We know, then, that we can stop acquiring additional samples whenever

$$\frac{\sigma}{\sqrt{N}\,\epsilon\,\mu_N\,A} \leq 1. \tag{92}$$

In the algorithm developed, ϵ was set to 0.02 and A was set to 0.5. Due to the nature of the criteria above, it is the product of these two that is significant. Thus, instead of considering the results as a 2-percent accuracy (100ϵ) to a 75-percent confidence level ($100\,(1 - A^2)$), the results could equally be viewed as a 5-percent accuracy to a 96-percent confidence level ($\epsilon = 0.05$, $A = 0.2$), etc. In other words, the solutions we seek have a probability of less than 25 percent of deviating more than 2 percent from the actual solution, and a probability of less than 4 percent of deviating more than 5 percent from the actual solution. In the implementation these restrictions become even more stringent because we only consider the worst case flux. That is, the smallest flux will usually have the largest fractional error and will require more model iterations to satisfy the convergence criteria than fluxes from the remaining five faces. Thus, the accuracy of the remaining five faces will always exceed the threshold while the accuracy of the sixth surface will at least meet the threshold convergence.

Note finally that σ^2 is not known a priori and is also an estimate, but with the number of samples required under the Monte Carlo method, we generally have a very good estimate for this value as well whenever we have met the above criterion for μ_N accuracy.

3.2 Model Overview

The Monte Carlo model developed to implement the above strategy was written in the C++ language. It was designed to generate statistical fractional energy flux information for photons passing through a scattering volume and out one of the six sides. C++ is an object-oriented programming language (c.f., Lafore 1991), and as such, several different object classes were designed to simulate the various phases of the scattering process. Several different phase function types were programmed into a phase function object class. Options included a Henyey-Greenstein phase function and the Deirmendjian type-C.1 cloud phase function for a wavelength of 0.45 μm. The propagation of photons was handled through the development of a ray object class. In this class, a phase function could be accessed to determine the angle of scattering (deflection) of the photon from its current path at the point of collision. Other classes were developed to handle the bookkeeping of photons passing through various wall sections within the scattering volume, angular information, positional information, etc.

3.3 Model Validation/Comparisons

To verify the validity of the IHMC model, test runs have been compared with the results of McKee and Cox (1974). In figures 12 through 14, the outputs of IHMC are compared with output of the McKee and Cox (M&C) Monte Carlo model, as derived from figures 3 through 5 of their paper. Comparisons are made for incident zenith angles of direct radiation of 0°, 30°, and 60°, respectively. The original data of M&C were modified to include directly transmitted radiation, based on an estimate of the optical depth of the cell for each their data points. These corrections were made using the transmittance equations given in chapter 2 and the zenith angle of the direct radiation relative to the normal to the top of the scattering volume. From their data, it appears that volume single-axis optical depths of 5, 10, 15, 25, 50, and 73.5 were used by M&C.

The M&C scenarios consisted of a cubic volume filled with a uniform conservative scattering material characterized by a phase function obtained from Deirmendjian (1969) for a type C.1 cloud at a wavelength of 0.45 μm. This is a phase function simulating a cumulus-type water cloud. Conservative scattering was assumed in all calculations.

Comparison of the results in the three figures indicates IHMC closely follows the M&C data. Slight differences are seen for the energy exiting the volume sides for the 60° zenith angle case, but here the difference may be in the corrections applied to account for the amount of direct energy passing through the volume. The exact values of the optical depths used by M&C were not reported, except for the maximum optical depth case (73.5). Another explanation is that the M&C data may be slightly in error: Davies (1978) reported small discrepancies when he compared his own results with the M&C calculations and attributed the differences to weaknesses in the M&C algorithm. Note, for example, that in
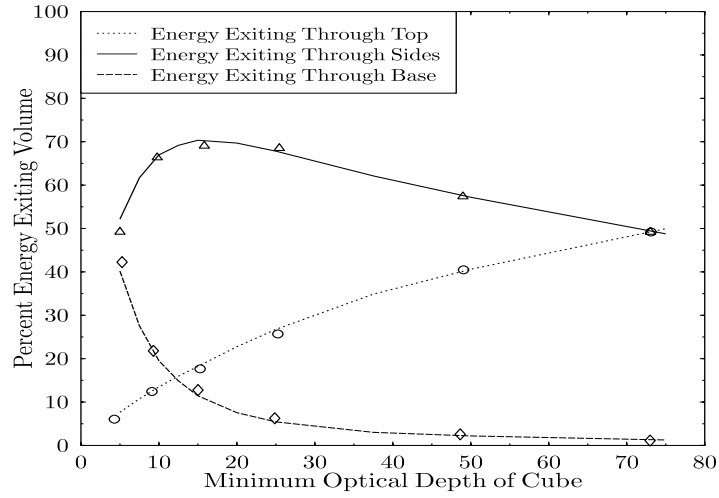
Figure 12. Scattered and transmitted energy exiting from a cubical volume. Symbols represent M&C data modified to include transmitted direct energy. Curves represent IHMC results. Incident energy is a plane parallel beam striking the top of the volume with a normal incidence.
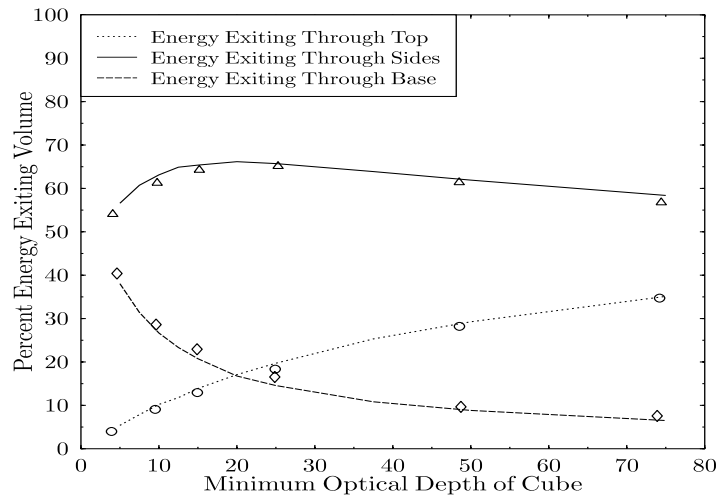
Figure 13. Monte Carlo comparisons similar to previous figure except incident energy strikes the top with a zenith angle of 30° relative to the normal. Incident radiation strikes top and one side of the volume.

figure 14 the geometric result for energy exiting through the sides at zero optical depth should be 63.4 percent. The trend in the corrected M&C data is for less
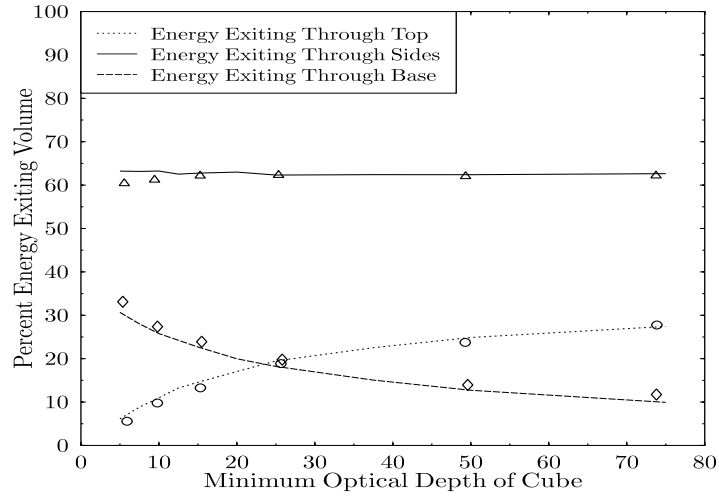
Figure 14. Results similar to previous figure except that incident energy strikes the top with an angle of 60° relative to the normal. Incident radiation strikes top and one side of the volume.

than 60 percent to be flowing out the sides. Similarly the geometric result for energy exiting the volume base should be 36.6 percent. Both of these targets appear consistent with the trends at low optical depth for the in-house model.

From these figures, there is a determination that IHMC achieves a reasonable performance when compared to the M&C results. Further, since we can control the exact model specifications for the cases of comparison, there is no question regarding what optical depths to apply in running the BLITS code. The IHMC model will thus be used henceforth for comparisons with the BLITS code. However, we will restrict the application of IHMC to only those scenarios described by M&C, for which we have direct verification that the code is valid. (Note: we compared results using the BLITS model because M&C dealt with specific uniform density media. AIM generates input data for general atmospheric conditions and would be inappropriate for comparison.)

3.4 Analysis

The results of the BLITS code were compared to those of the IHMC code for each scenario studied by M&C. Results were obtained from the Monte Carlo code using the full Diermendjian C.1 phase function. BLITS results were produced using modified Legendre expansion coefficients of the phase function such that the forward peak was removed via one of two different scaling transformations. The first transformation was the δ-M method proposed by Wiscombe (1977). The second was the log-least-squares (LLS) method described

in the appendix. The second method was developed to suppress higher order Legendre components, thereby avoiding negative values in the phase function approximation. These negative values can lead to erroneous predictions of stream radiances.

Comparisons were made for various levels of resolution of the calculation grid for the cubic scattering volumes used by M&C. These calculations show the overall robustness of the method. The walls of the volume were considered to be bounded by a non-reflecting/non-emitting void. The external illumination consisted of a plane parallel source incident on the top and one side of the volume (virtually a cubical gas in deep space). The cases considered varied the medium's single-axis optical depth and the zenith angle of arriving direct radiation. Results were computed for direct energy incident at the top of the volume and striking the eastern side from $0°$, $30°$, and $60°$ zenith angles. We did not use the M&C data, except for comparison. Instead, we computed results using IHMC and BLITS for single axis optical depths of the medium of 5, 7.5, 10, 12.5, 15, 20, 25, 37.5, 50, and 75.

In figure 15 we compare the $0°$ zenith angle incidence direct source case for flux reflected off the top of the modeled volume using IHMC and BLITS with varying numbers of cells. This figure is based on BLITS runs using the δ-M method, and the results show that, even with a nominal 35 optical depths per cell, the $2\times2\times2$ coarseness calculations produce reasonable results. Figure 16 shows the same output for the LLS method described in the appendix. Note that the LLS method appears not to predict results as well as δ-M at the $2\times2\times2$ resolution, but appears to approach the IHMC results asymptotically as the resolution is increased.

Figures 17 through 20 show details of the fluxes emitted from the sides and bottom of the scattering region at different computation resolutions for the δ-M and LLS methods for the same $0°$ incident scenario. As can be seen, while the performance of the algorithm appears robust and seems to operate efficiently for both the δ-M and LLS methods, the LLS approach appears to slightly outperform the δ-M results at the higher resolutions, which we assume behave in an asymptotic fashion. Similar results were obtained for the M&C cases of $30°$ and $60°$ angles of incidence of the direct radiation beam. In all cases studied, the LLS method appeared to outperform the traditional δ-M approach. The primary factor for this increase in performance is attributed to the nature of the phase function and the limitation imposed that only a 24-stream model was used. For this case, the δ-M corrected Legendre expansion of the phase function produces negative phase function results in 8 out of 24 different scattering directions. These negative values produce negative stream values after the direct radiation scatters into these directions. Once these negative radiances are in place, they then disrupt the overall evaluated flux statistics. Introducing more streams would solve the problem of the negative radiances because a higher order Legendre expansion could be used, but this would require larger system memory and slower model operation.

Figure 15. Comparisons for the δ-M method at varying cell resolutions of the scattering volume for 0° zenith angle incident direct energy for energy exiting volume top.

Figure 16. Comparisons for the LLS method at varying cell resolutions of the scattering volume for 0° zenith angle incident direct energy for energy exiting volume top.
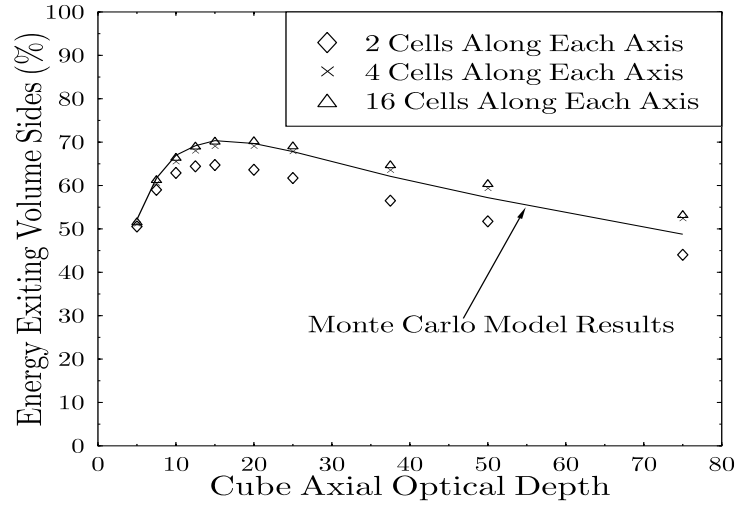
Figure 17. Comparisons for the δ-M method at varying cell resolutions of the scattering volume for 0° zenith angle incident direct energy for energy exiting volume sides.
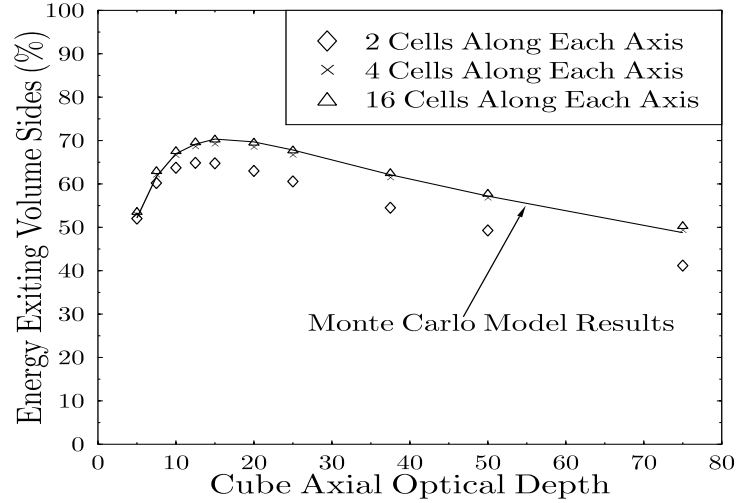
Figure 18. Comparisons for the LLS method at varying cell resolutions of the scattering volume for 0° zenith angle incident direct energy for energy exiting volume sides.
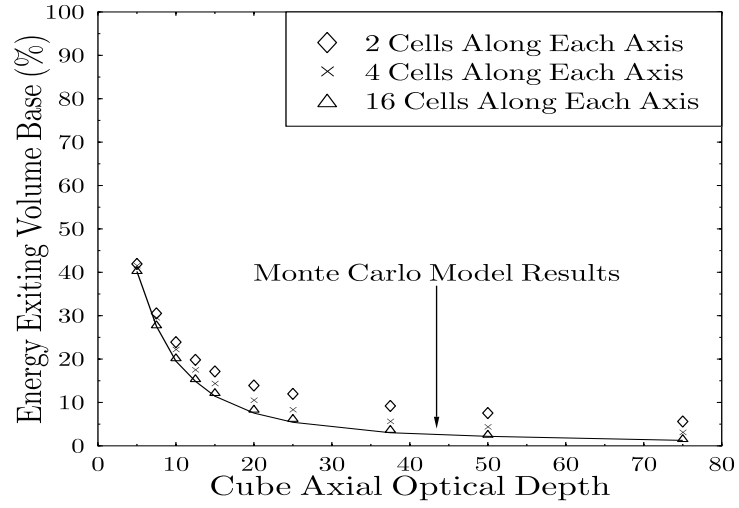
Figure 19. Comparisons for the δ-M method at varying cell resolutions of the scattering volume for 0° zenith angle incident direct energy for energy exiting volume base.
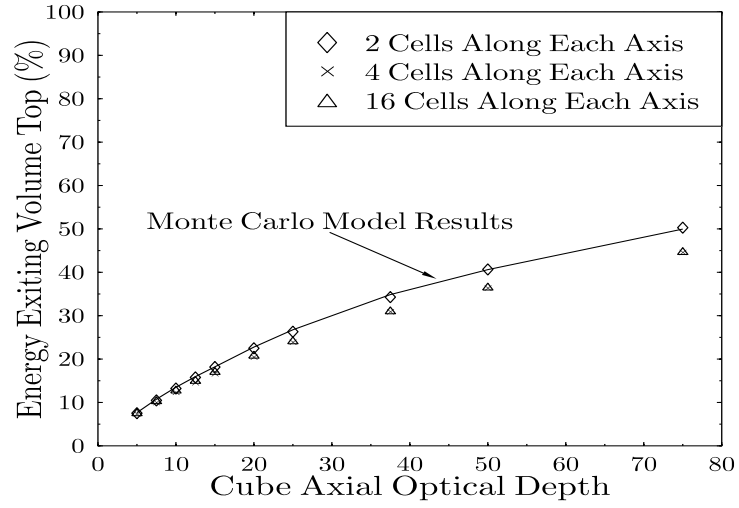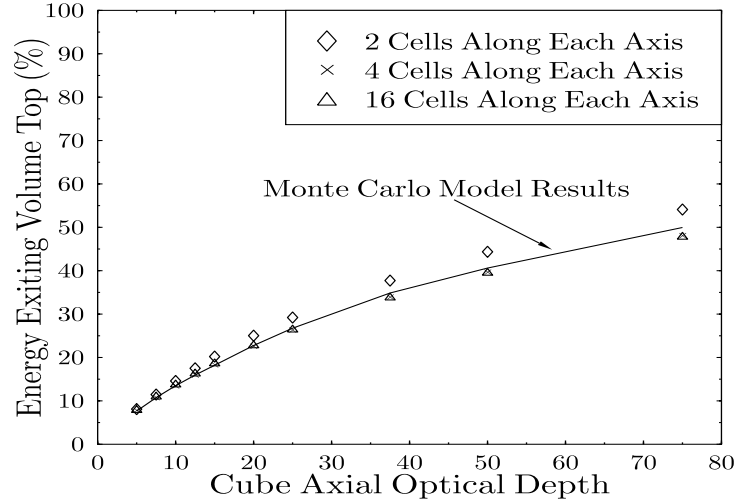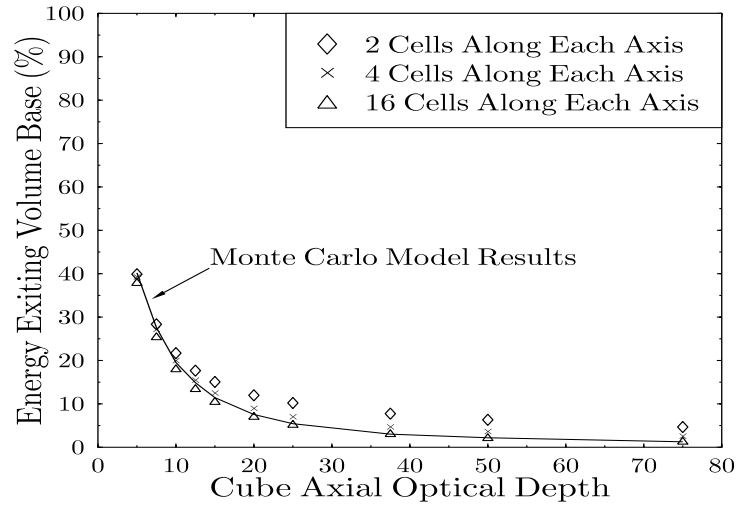

Figure 20. Comparisons for the LLS method at varying cell resolutions of the scattering volume for 0° zenith angle incident direct energy for energy exiting volume base.

However, disregarding for the moment any differences between the LLS and δ-M performances, the primary characteristic of these results is that the `BLITS` scattering algorithm appears to approximate the Monte Carlo model outputs to a high accuracy at all optical depths for the 4^3 and 16^3 cases. The worst case (the $0°$ flux exiting the volume sides) fails at the two-cell approximation simply because two cells per axis are insufficient. Certainly the four-cell case has much better performance at 70 optical depths than does the two-cell model at 17 optical depths, even though these two cases have roughly the same optical depth per cell. This indicates that the overall success of the model seems to depend on the feedback produced by sufficient numbers of lattice walls interior to the modeled volume.

3.5 3D Segmented Cloud Cases

Analysis of the `BLITS` model performance in the M&C cases revealed that two cells per axis was insufficient to fully test the viability of the model, since the model relies on interaction between scattering effects at different interior walls within the modeled volume. But, with the elimination of the single cell and two-cell-per-axis cases, the maximum optical depth per cell that is treated is 75/4=18.75. This number is relatively low when compared to the optical depth of a typical scale cloud puff of 1/4 km on a side. In order to test the model at higher aerosol concentrations, a set of modified scenarios had to be developed. But, these new scenarios should have certain characteristics. It would be possible simply to run uniform volume cases like the M&C scenarios, but at much higher optical depths. And, while this course has some merit, it does not address the issue of multiple scattering interaction between different cloud elements. Further, there is no consistency check on the results obtained to ensure that there is not some flaw in the technique at higher optical depths. Another possibility is to devise a means of concentrating the aerosols into fewer cells, creating gaps between the different cloud elements, and thus permit testing of cloud-to-cloud scattering interactions.

The result of these considerations was a method which conformed to the M&C scenarios in one limit, but which modeled separate cloud sections as a function of a pair of related separation parameters, q and P.

Let the overall modeled volume be described by a cube of unit length (1 km) on each axis. Then, define the quantity q as a fractional length and divide the volume into eight cubes, one each with an outer corner positioned in each corner of the overall volume, as shown in figure 21. The parameter q measures the single-axis fractional length of each of the eight scattering subregions within the overall volume ($0 \leq q \leq 1/2$). The remainder of the overall volume is considered vacuum. The fractional distance along a single axis from center-to-center of two of these cubes is $1 - q$. We then introduce the parameter P as $P = q/(1 - q)$, which varies between 0, where all the scattering material has been compressed into the eight corner regions, and 1, where the scattering material is uniformly distributed over the entire scattering volume. Thus $P = 1$ corresponds to the

M&C scenarios and $P = 0$ corresponds to a vacuum condition. We thus have complete information about the bounding behavior of the scenarios proposed and can investigate the intermediate behavior to see that it smoothly transitions by varying the P parameter.
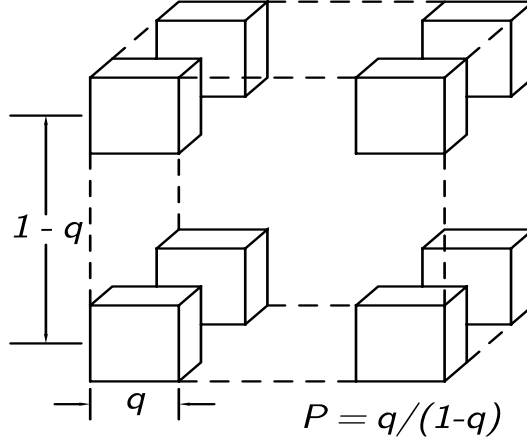
Figure 21. Cloud subregion configuration within the overall scattering volume utilizing q and P parameters.

Figures 22 through 30 illustrate the different fluxes (top, base, and sides) for the three different incident flux zenith angles. The optical depths in each scenario have been normalized to the uniform density scatterer case such that a constant amount of scatterer is present in the overall volume as P varies. This is accomplished by computing a modified extinction coefficient, $\sigma' = \sigma/(8\,q^3)$, which accounts for the concentration of the scattering materials in the eight corner regions. Note that as P decreases from unity more of the incident radiation passes unscattered through the volume. This is significant in the analysis of results.

Using these Monte Carlo results as the baseline, we then proceeded to run the `BLITS` model at a series of resolutions (number of cells per axis) for each scenario. Similar to the previous figures, we ran the model at 1, 2, 4, 8, 16, and 32 cell resolutions, hereafter referred to as the 1^3, 2^3, 4^3, 8^3, 16^3, and 32^3 cases, respectively, in reference to the total number of cells modeled in the volume. We used the same average densities per optical axis as in the previous cases run, and set the P parameter to 1/3, 3/5, and 7/9, corresponding to q values of 1/4, 3/8, and 7/16, respectively. Note that in all three of the new P value cases ($P = 1$ in the original M&C scenarios), the 2^3 model resolution was incapable of resolving the density variations. In terms of the analysis below, these cases are termed

63
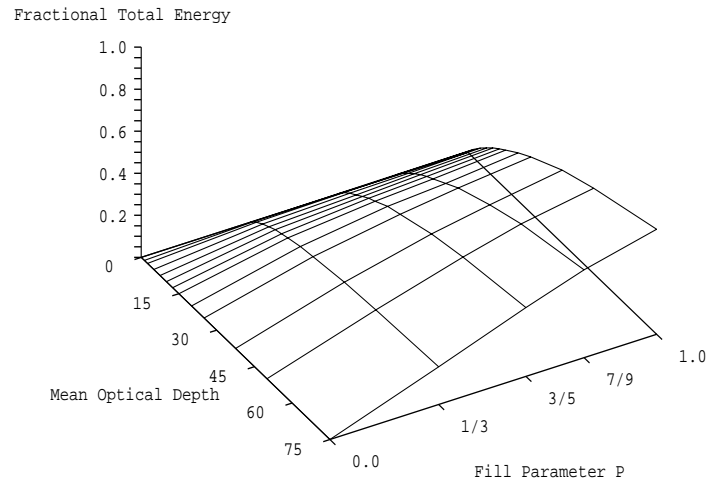
Figure 22. Fractional flux escaping from volume top for 0° incident direct radiation as a function of the P parameter and mean single-axis optical depth.
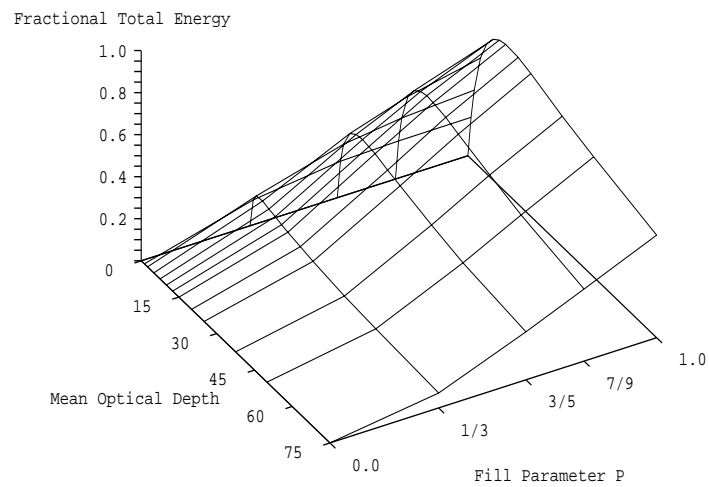
Figure 23. Fractional flux escaping from volume sides for 0° incident direct radiation as a function of the P parameter and mean single-axis optical depth.

64
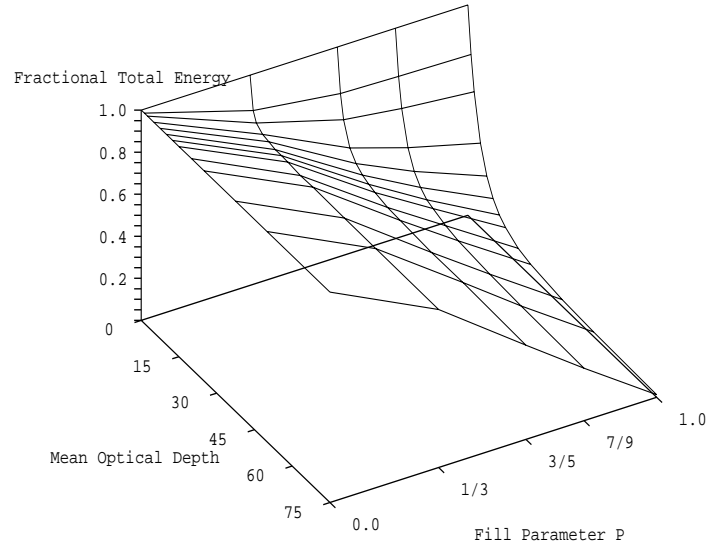
Figure 24. Fractional flux escaping from volume base for 0° incident direct radiation as a function of the P parameter and mean single-axis optical depth.
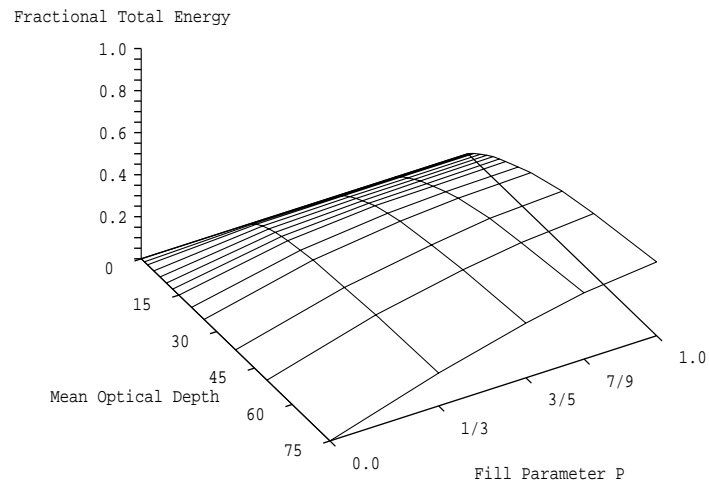
Figure 25. Fractional flux escaping from volume top for 30° incident direct radiation as a function of the P parameter and mean single-axis optical depth.
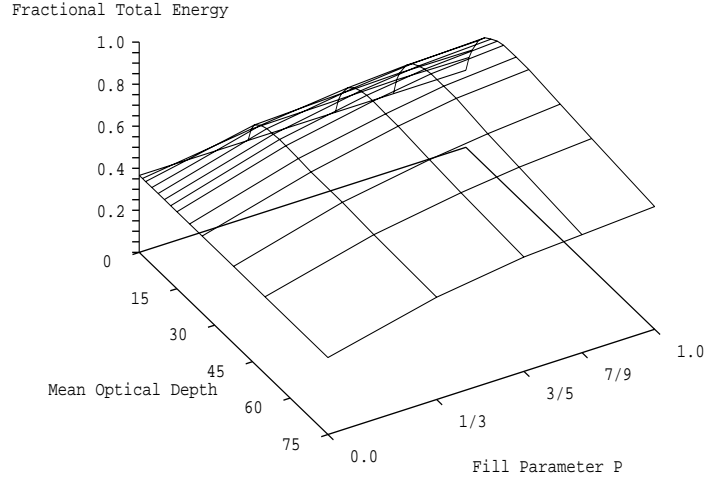
Figure 26. Fractional flux escaping from volume sides for 30° incident direct
radiation as a function of the P parameter and mean single-axis optical depth.
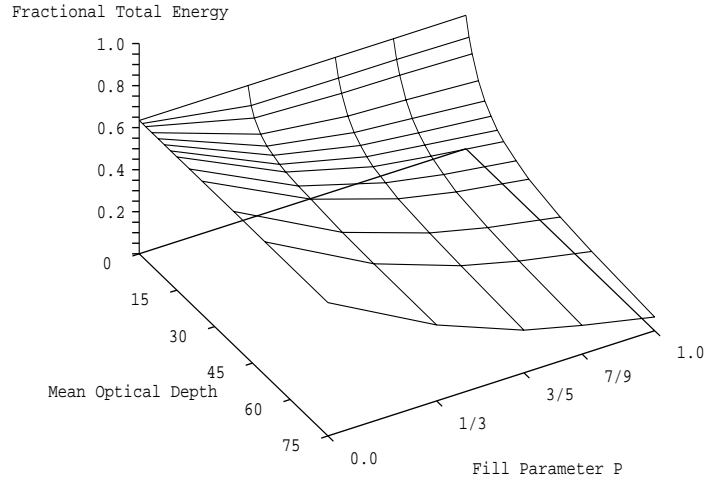
Figure 27. Fractional flux escaping from volume base for 30° incident direct
radiation as a function of the P parameter and mean single-axis optical depth.
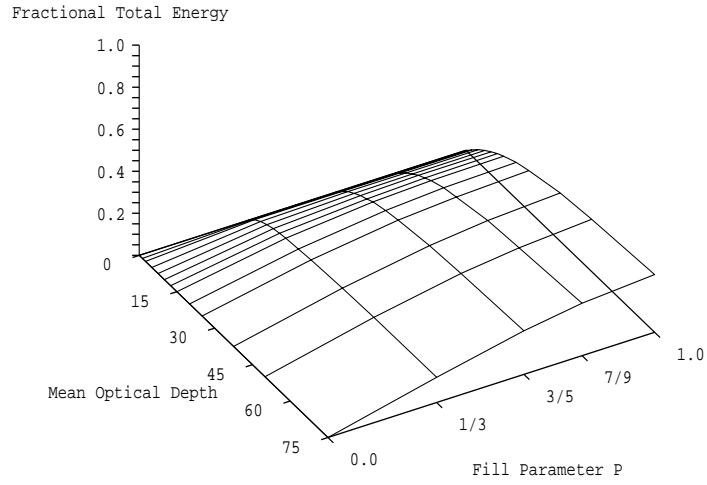
Figure 28. Fractional flux escaping from volume top for 60° incident direct radiation as a function of the P parameter and mean single-axis optical depth.
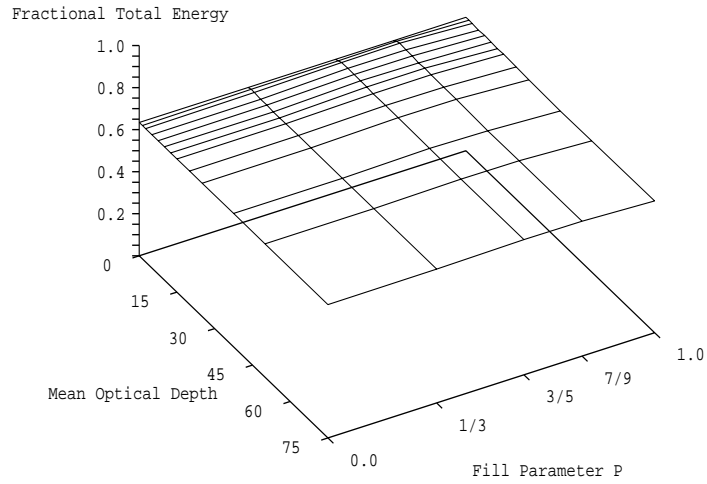
Figure 29. Fractional flux escaping from volume sides for 60° incident direct radiation as a function of the P parameter and mean single-axis optical depth.
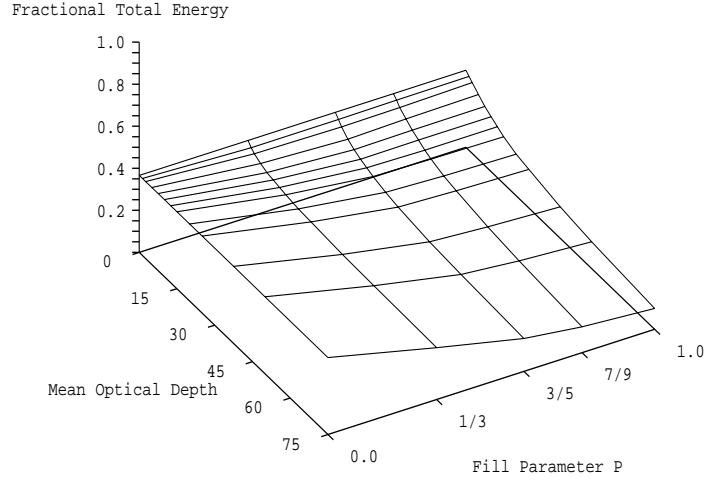
Figure 30. Fractional flux escaping from volume base for 60° incident direct radiation as a function of the P parameter and mean single-axis optical depth.

under-resolved. The 4^3 model, on the other hand, was able to *critically-resolve* the $P = 1/3$ case. That is, in the 4^3 model each cloud segment occupied exactly 1 cell in the corner of the volume. In all other cases, the 4^3 model under-resolved the cloud segments. For the 8^3 model, in the $P = 1/3$ case, each cloud segment occupied a 2^3 cell region in each corner of the volume, and in the $P = 3/5$ case each cloud segment occupied a 3^3 region in each corner. But, the 8^3 model was unable to resolve (under-resolved) the cloud edges in the $P = 7/9$ case. We thus were able to study several conditions: under-resolved cases where the physical model was unable to resolve the density variations, critically-resolved cases where the physical boundaries of the cells could just match the boundaries of the cloud segments (for example, in the $P = 1/3$ case using the 4^3 model), and those cases that were over-resolved (for example, the 32^3 model for the $P = 3/5$ case where both the regions containing the cloud segments and the gaps between the segments were able to be modeled as more than one cell wide). The behavior of BLITS under these various conditions allows the testing of the robustness of the code in providing flux data under various degrees of stressing conditions.

However, following computation of these scenarios, it became apparent that except for the 1^3 and 2^3 models which had already been shown to lack sufficient numbers of cell walls to produce reliable results, the remainder of cases fell decisively into only two groups: a first group containing all the under-resolved cases, and a second group containing both the critically-resolved and over-resolved cases. The under-resolved cases consisted of the 4^3 model results for the

$P = 3/5$ and $P = 7/9$ cases and the 8^3 model results for the $P = 7/9$ case. In all the critically-resolved and over-resolved cases, the model exceeded expectations in producing very close results to the Monte Carlo run outputs for cell optical depths up to 37.5 per cell (pre-scale transform optical depth). Even after the scale transform, which reduced the extinction coefficient by about 60 percent, we were still treating up to 20 optical depths per cell in the worst case (the 4^3 model in the $P = 1/3$ case). For this case, we had an overall RMS error of 1.57 percent of the total flux. The results for all cases are shown in table 5.

Table 5. RMS errors for all cases run; under-resolved in brackets, critically-resolved in parentheses, over-resolved without brackets.

P	% RMSE					
	1^3	2^3	4^3	8^3	16^3	32^3
1/3	[22.8]	[25.3]	(1.57)	0.76	0.638	0.534
3/5	[11.4]	[13.4]	[12.9]	(0.80)	0.714	0.597
7/9	[6.3]	[6.3]	[7.06]	[6.86]	(0.901)	0.858
1	(7.7)	2.5	0.98	0.93	0.857	0.934

To analyze the significance and meaning of these results, we divide the consideration of these results into low-, medium-, and high-resolution cases. Figures 31 through 34 show the low resolution cases of the 1^3 and 2^3 models. Since they are only resolved in the uniform density ($P = 1$) case, they illustrate the situation of a cloud with spatial structure, which, due to the model spatial resolution, nevertheless occupies only a single cell in the modeled space. One interesting feature of the table is a comparison between the 2^3 and the single cell model results for the $P = 1/3$ and $P = 3/5$ cases. Here, the single cell actually outperforms the 2^3 model. The reason appears to be that the 2^3 results do a much better job of characterizing the $P = 1$ case to the extent that they are over-optimized. That is, in a sense, the 1^3 model appears to be doing the job of representing an ensemble of different density conditions that all map onto a uniform density problem when expressed in a single cell model. Of course, the low P cases have the volume almost empty of material and so represent worst case conditions of applying the uniform cube model as a representation of physical reality.

The next several cases consider the various results of the 4^3 and 8^3 characterizations. These cases are interesting because they provide a better insight into the model behavior due to their greater numbers of interior cell walls. They also illustrate critically resolved cases of $P = 1/3$ using the 4^3 model and $P = 3/5$ using the 8^3 model, both of which show excellent response under high-density cell conditions. These results are given in Figures 35 through 40. One of the most interesting features is the similarity between results in the
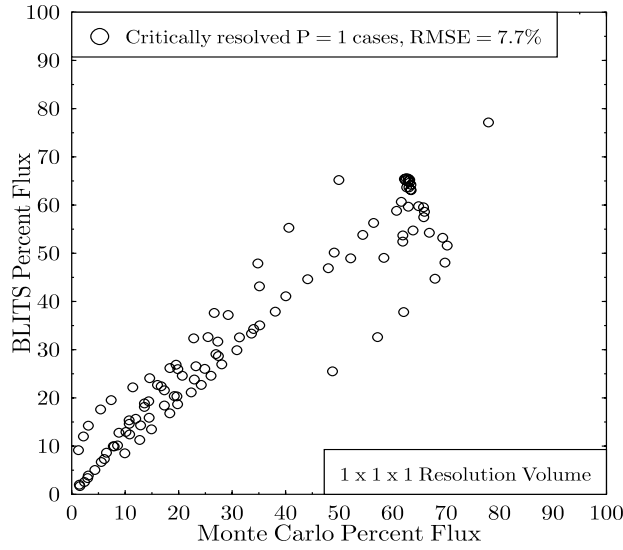
Figure 31. Uniform density media for the one cell model.
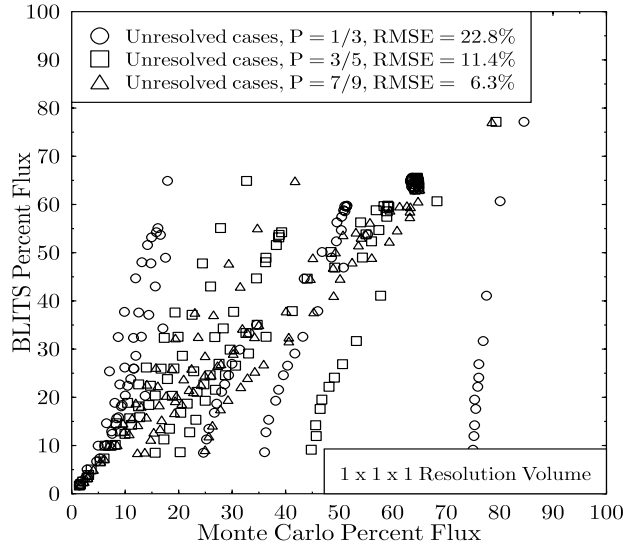
Figure 32. Under-resolved cases for the one cell model.

two cases, for even though the 8^3 model has additional flexibility, the results for the unresolved $P = 7/9$ case are very similar in both examples even though the 8^3 model has a few of its inner cells with somewhat lower optical depths. These results tend to indicate that natural clouds will be so optically thick that their influence will extend outside their volume if too coarse of a grain is used in modeling the geometry of the cloud cellular structure. These extensions might, under unlucky circumstances, result in inappropriate fluxes reaching the surface.
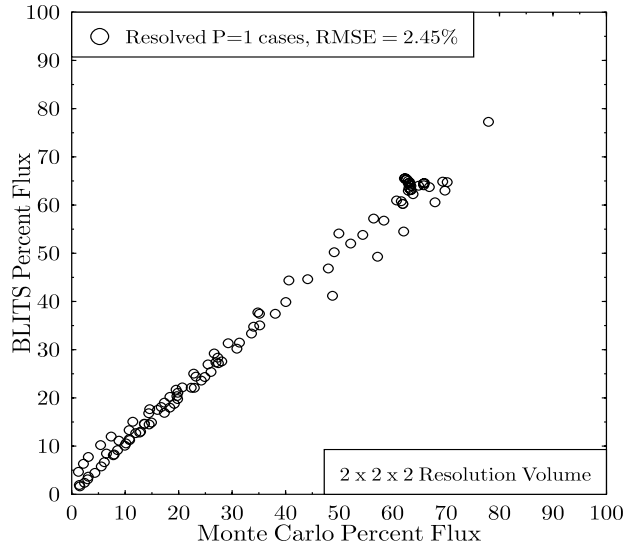
Figure 33. Uniform density media case for the 2^3 cell model.
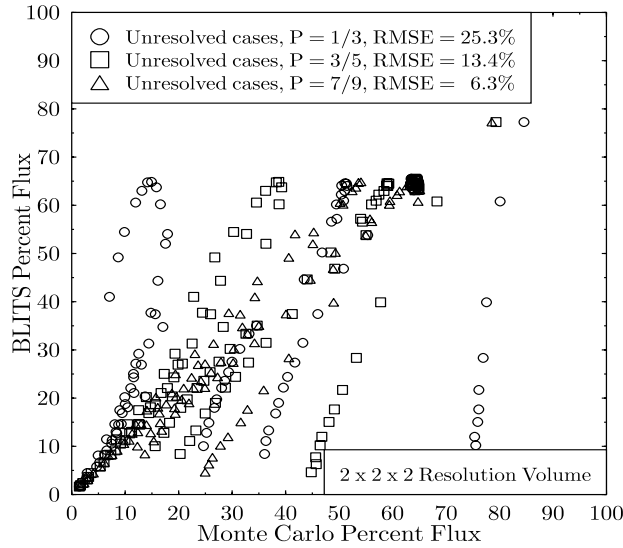
Figure 34. Under-resolved cases for the 2^3 cell model.

In most cases, then, the effects of coarse grids will be an increase in estimated cloud layer reflectivity and a decrease in estimated net layer transmittance. These observations have obvious implications beyond the domain of our present problem because they indicate some of the weaknesses of 1D RT models, in that these models will tend to underestimate the net solar loading to the ground and thus may influence global energy balance estimates.

The final group of cases are the high resolution 16^3 and 32^3 cell models. Here,
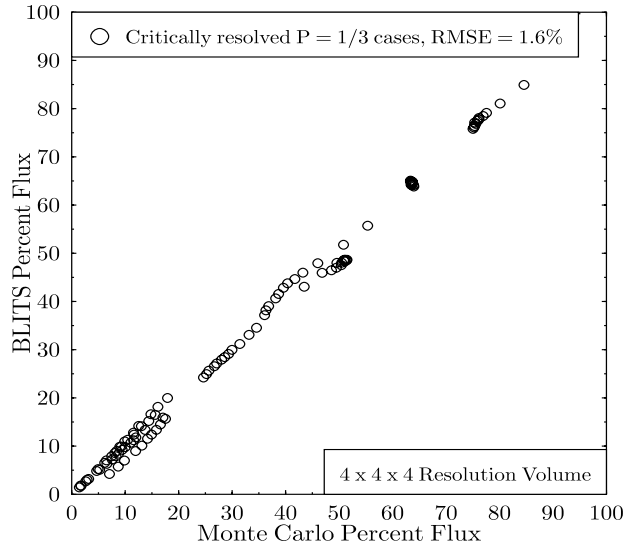
Figure 35. Critically-resolved cases for the 4^3 cell model.
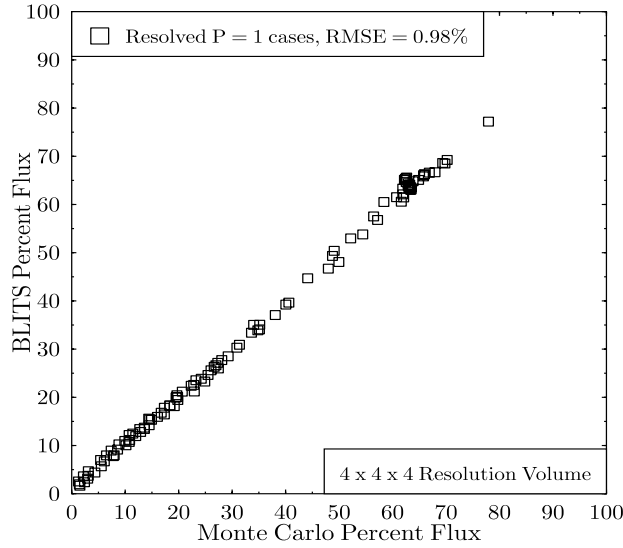
Figure 36. Resolved cases for the 4^3 cell model.

there is only one critically-resolved scenario ($P = 7/9$ for the 16^3 model), with the remainder over-resolved. As anticipated, these results all show a high correlation to the Monte Carlo results. Here, we also note that it would be difficult to actually produce results that are much closer to the Monte Carlo model outputs regardless of the number of cells we used unless we were to rerun the Monte Carlo cases. Since we only used 2 percent accuracy in the Monte Carlo runs, it is unlikely we could improve much on the approximately
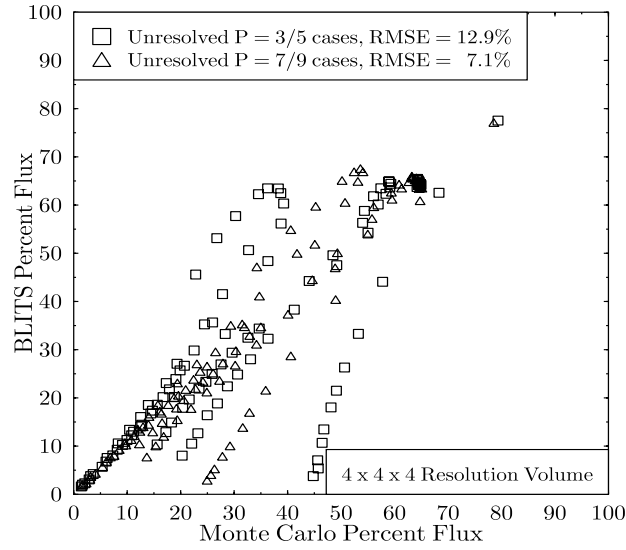
Figure 37. Under-resolved cases for the 4^3 cell model.
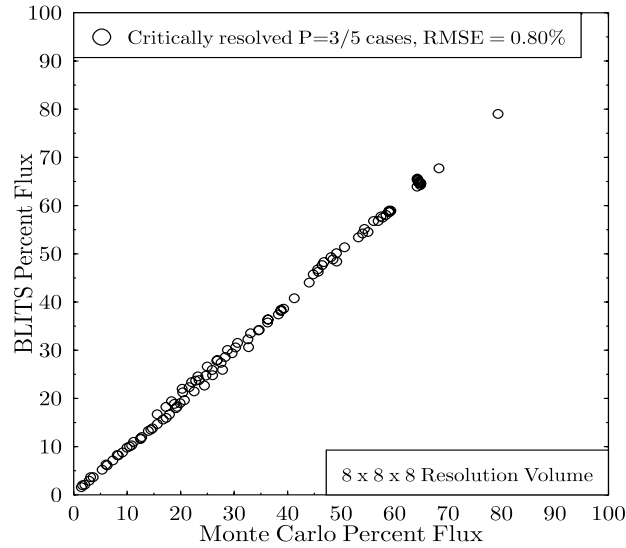
Figure 38. Critically-resolved cases for the 8^3 cell model.

1 percent accuracy of the RMSE. Note further that in all the 16^3 and 32^3 results, the correlation to the Monte Carlo results was 0.999 or greater, which validates both the Monte Carlo approach followed as well as the BLITS model results. The results for these comparisons are found in figures 41 through 43.
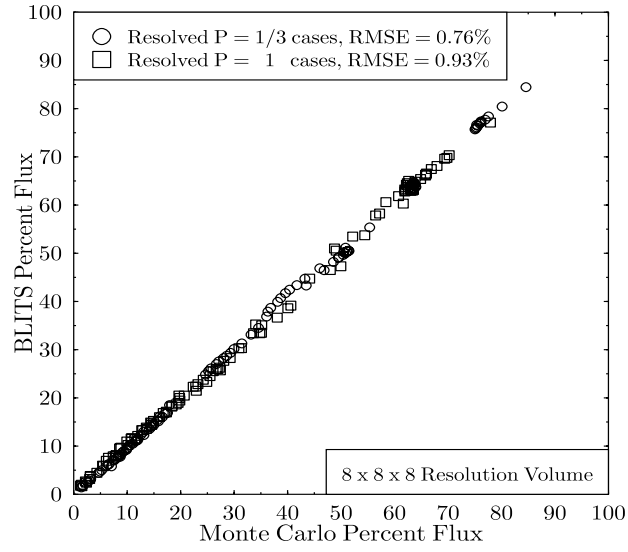
Figure 39. Resolved cases for the 8^3 cell model.
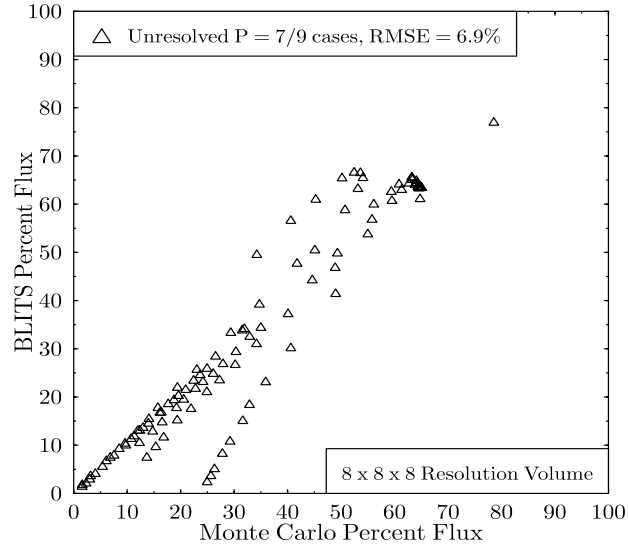
Figure 40. Under-resolved case ($P = 7/9$) for the 8^3 cell model.
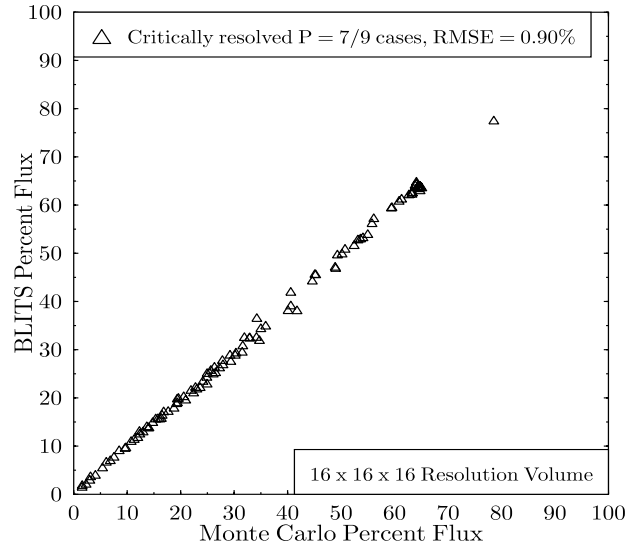
Figure 41. Critically-resolved case ($P = 7/9$) for the 16^3 cell model.
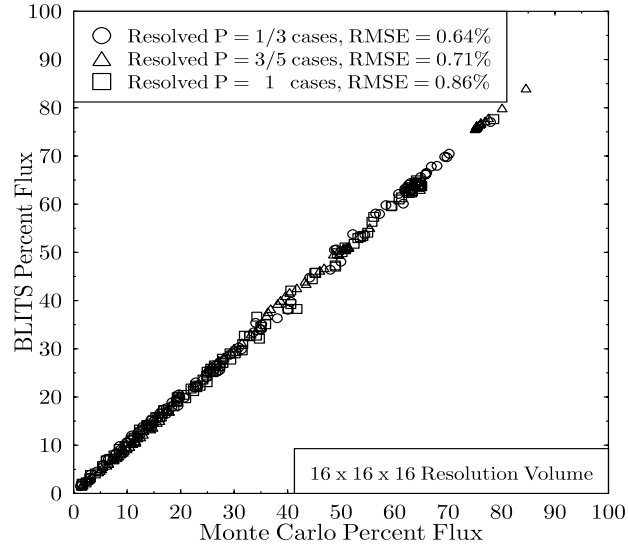
Figure 42. Resolved cases for the 16^3 cell model.
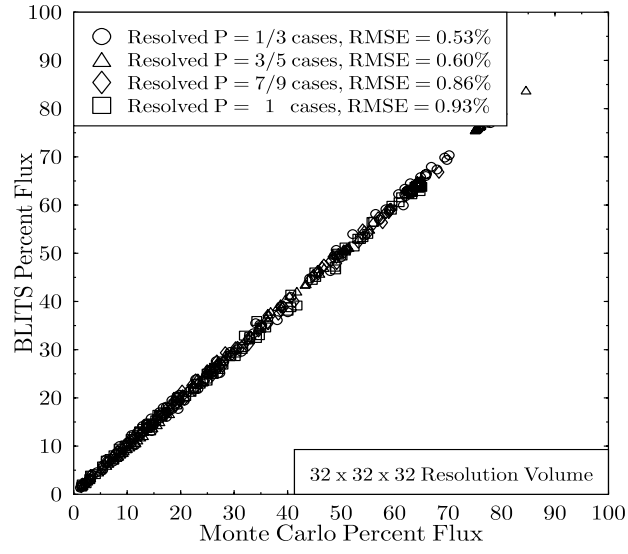
Figure 43. All cases for the 32^3 cell model.

4. Using AIM Output

The primary purpose of the RT codes discussed in this report is to facilitate the radiometrically correct rendering of the appearance of natural cloud scenes. This task encompasses several related subtasks. For example, one may be interested in the appearance of a simulated surface below a broken cloud field. One may wish to render objects (trees, buildings, bridges, vehicles) that are either attached to or moving on or near the terrain. One may wish to determine the atmosphere's appearance (fog, haze, or precipitation) under clouds. Or, one may wish to characterize the appearance of the cloud field itself.

Each of these subtasks entails a sequence of different processing steps. However, this chapter focuses on the rendering of components of the atmosphere. For this set of tasks, one must perform integrations over specified lines of sight. Each LOS will have an initial radiance value plus path integrated properties. These path properties entail transmittance and path radiance characteristics. The path radiance requires interpolations over direction and position of RT code results obtained in a set of specific directions at regularized positions. Positional interpolation can be accomplished any number of ways, though the process is generally based on distance to nearest neighbor points. Directional interpolation depends on the Gaussian quadrature method chosen to simulate the scattering. This chapter ends with a description of a cloud rendering methodology and several output file formats useful for input to visualization routines.

4.1 Line of Sight Calculations

For any medium we have a standard technique for representing the effects of the volume for a given LOS through the volume. This technique is related to the equation of radiative transfer (22), and its solution, Eq. (24). Since any image to be rendered can be considered composed of a series of pixels, and each pixel can be thought of as representing a particular LOS through the medium, determining the atmospheric effects for a particular image becomes a matter of tracing a large number of lines of sight through the simulated atmosphere. Each LOS is characterized by an origin, a direction, and a distance, and effects are determined by tracing through a sequence of adjacent cells in the scattering volume.

4.2 Integration Procedure

For the moment, let us assume that we know the original value for the scene radiance at the far end of each LOS associated with each image pixel. All that remains then is to evaluate the transmittance and integrated path radiance associated with the intervening atmosphere. Call the initial radiance associated with a pixel I_0. Let S represent the path length of the intervening atmosphere. Let $\tilde{T}_S$ be the transmittance, and L_S be the integrated path radiance of that atmosphere. Then, if I_S is the radiance presented at the terminus of that atmospheric path as the energy enters the imaging optics, we have,

$$I_S = I_0\,\tilde{T}_S + L_S. \tag{93}$$

The entire effect of the atmospheric path can thus be represented by $\tilde{T}_S$ and L_S.

While some simplistic models compute $\tilde{T}_S$ and L_S from single values of extinction coefficient and limiting path radiance (as in the Introduction), these are actually integrated quantities. Normally, atmospheric path effects are evaluated by dividing the LOS into a series of small increments from the observed object to the observer. But these equations can also be evaluated outward from the observer, and we shall show why this method has certain advantages during the rendering process.

First, we consider the traditional method running the LOS from the object to the observer. Let n be an index that runs from 1 to N, and let s_n be the length of a given path increment along a line from the object to the observer. We then define $\tilde{t}_n$ as the transmittance over the path increment s_n and l_n as the limiting path radiance over that increment. Since we have now converted a continuous calculation into a series of increments, let us define $\tilde{T}_N = \tilde{T}_S$ as the total transmittance over the entire LOS, and,

$$\tilde{T}_n = \tilde{T}_{n-1}\,\tilde{t}_n; \qquad \tilde{T}_0 = 1. \tag{94}$$

Similarly, let us define S_n as

$$S_n = S_{n-1} + s_n; \qquad S_0 = 0. \tag{95}$$

This implies $S_N = S$. Lastly, we have a recursive definition for L_n,

$$L_n = L_{n-1}\,\tilde{t}_n + l_n\,(1 - \tilde{t}_n); \qquad L_0 = 0, \quad L_N = L_S. \tag{96}$$

Here, T_0, S_0, and L_0 are initial values. However, it is often more valuable to determine the path characteristics from the observer's perspective by integrating the path effects beginning at the observation point and proceeding out along the LOS. For this consideration, let us define a new index variable $m = 1 + N - n$.

We can then define a new set of transmittance and path radiance variables, $s'_m = s_{1+N-m}$, $\tilde{t}'_m = \tilde{t}_{1+N-m}$, and $l'_m = l_{1+N-m}$. Then,

$$S'_m = S'_{m-1} + s'_m; \qquad S'_0 = 0. \tag{97}$$

$$\tilde{T}'_m = \tilde{T}'_{m-1}\,\tilde{t}'_m; \qquad \tilde{T}'_0 = 1. \tag{98}$$

$$L'_m = L'_{m-1} + \tilde{T}'_{m-1}\,l'_m\,(1 - \tilde{t}'_m); \qquad L'_0 = 0. \tag{99}$$

This second path description has the advantage that objects at different ranges along the same LOS can be interpolated using results at different m indices. These results thus would work well for moving objects as they change ranges and possibly position within the field of view, assuming a stationary observer. A further advantage of this approach is that if there is some threshold transmittance below which we are essentially viewing only atmosphere, then the path integration can be truncated, saving computer resources. In contrast, the disadvantage of the former approach is that even if the observer is moving, there will only be at most a single LOS that obtains the advantage that results can be reused for the observer at different ranges from the object. All other lines of sight must be continually recomputed. It therefore appears that the second approach is more versatile.

To evaluate the quantities $\tilde{t}'_m$ is relatively routine. Over each path segment, there will be a given extinction coefficient, k'_m, associated with the cell in the modeled domain being traversed. The transmittance over that path segment will then be $\tilde{t}'_m = \exp(-k'_m\,s'_m)$. The distances traversed in each cell can be determined through a ray tracing algorithm. For cubical cell shapes, the computation of s'_m is relatively straightforward. However, due to the computer-intensive computation of $\tilde{t}'_m$, it may be more efficient to use less exact means whereby the path is sampled in evenly spaced increments. This latter method allows for more rapid simulation of the path geometry but could lead to difficulties when the observer is in motion with respect to the cloud features.

The computation of the l'_m terms is somewhat more complicated. We treat this in two phases. First, volumetric limiting path radiances must be derived from the surface based radiance results of the RT code. This first stage produces results at the specific discrete ordinate directions for which the code was run. These results must then be interpolated by direction to produce a limiting path radiance for the specific direction leading into the observer's sensor. These topics are treated in the next two sections.

4.3 Evaluating Limiting Path Radiance

The extraction of limiting path radiance from the RT code results requires some reorientation in viewpoint, since the RT code output is surface averaged radiances, while the integrated path radiance calculation requires volume-based information.

In order to evaluate this information, we consider the energy of a single stream (index i) as it enters the volume. For this computation we return to the notation used in section 2.1, where χ_{ik} represents the components of stream i with respect to the x, y, and z axes, indexed by variable $k = 1, 2, 3$, respectively. Similarly, let I_{ik} be the average radiance predicted for stream i entering through the x, y, and z input walls of the volume, again indexed by variable k. And let $\bar{T}_{ik}$ be the mean transmittances through the cell for energy entering through the kth input face for stream i (same as the $\bar{T}$ statistics described in Eqs. (43) through (45), except that the 'standard' orientation results have been transformed to correspond to the correct walls for the stream in question).

For diffuse stream i we may determine the total flux entering the cell as:

$$E_{in,i} = \frac{\pi}{2} w_i \sum_{k=1}^{3} \chi_{ik}\, I_{ik}\, \Delta^2, \tag{100}$$

where Δ is again a cubical cell edge length, and where we weigh the energy according to the solid angle associated with the stream ($\frac{\pi}{2} w_i$) and the mean cosine of incidence across the cell wall (χ_{ik}). The total energy transmitted across this cell for stream i will similarly be

$$E_{tran,i} = \frac{\pi}{2} w_i \sum_{k=1}^{3} \chi_{ik}\, I_{ik}\, \bar{T}_{ik}\, \Delta^2. \tag{101}$$

If we then assumed a conservative scattering condition, we would expect that the scattered energy emitted from the volume element would account for the remaining energy. Call this amount $E_{cs,i}$ for the conservative scattered energy. The actual energy scattered under a single scattering assumption would be $\varpi\, E_{cs,i}$, where ϖ is again the single scattering albedo. Let

$$E_{cs,i} = \frac{\pi}{2} w_i\, \bar{I}_i \sum_{j=1}^{M} \frac{\pi}{2} w_j\, \tilde{P}(\mu_{ji}) \sum_{k=1}^{3} \chi_{jk}\, (1 - \bar{T}_{jk})\, \Delta^2 = C\, \bar{I}_i, \tag{102}$$

where the result is a linear function of $\bar{I}_i$, the j summation is over all output directions from the cube, $\bar{I}_i$ is the appropriate volume averaged radiance for stream i that produces the correct amount of emitted energy in the conservative scattering limit. The k summation is over the output faces, and thus χ_{jk} is the appropriate cosine of the jth stream with the kth output face; similarly, $\bar{T}_{jk}$ is

the mean transmittance of energy exiting the kth face via the jth stream, and μ_{ji} is the cosine of the angle between incident $(\hat{\Omega}_i)$ and exiting $(\hat{\Omega}_j)$ directions.

Using Eqs. (100) through (102), we may write

$$\bar{I}_i = \frac{(E_{in,i} - E_{tran,i})}{C} = \frac{\sum\limits_k \chi_{ik}\left(1 - \bar{T}_{ik}\right) I_{ik}}{\sum\limits_{j=1}^{M} \frac{\pi}{2} w_j\, \tilde{P}(\mu_{ji}) \sum\limits_{k=1}^{3} \chi_{jk}\left(1 - \bar{T}_{jk}\right)}. \tag{103}$$

Using this value for the volume averaged radiance for stream i, the total limiting path radiance for all streams in the standard discrete ordinates directions $\hat{\Omega}_l$ may then be determined as,

$$\bar{l}_l = \varpi \sum_{i=1}^{M} \frac{\pi}{2}\, w_i\, \tilde{P}(\mu_{li})\, \bar{I}_i. \tag{104}$$

However, this value accounts for only the diffuse scattering component of the limiting path radiance. To this value we must add the black body component and the direct component. The black body component is simply the B term previously described. For the direct component, we must follow a similar procedure to that described for the diffuse component, but the derivation must consider the delta scattering property of the direct radiance. The integration over output faces for the conservative scattering calculation involves terms $\tilde{P}(\hat{\Omega}_0, \hat{\Omega}_j)$, where $\hat{\Omega}_0$ is again the unit vector indicating the direction of propagation of the direct energy component. Second, instead of describing effects by scattering cell class, each cell must be individually assessed to determine the incident flux on each input face and the fractional transmitted energy for energy that entered through each face. Lastly, since the direct energy is either converted completely into diffuse stream energy, transmitted through the cell, or absorbed, there is no additional effect of direct radiation for path radiance purposes.

We thus have a complete procedure for evaluating the limiting path radiance for any cell in any direction, and thus we can determine the apparent brightness of any path through the scattering volume.

4.4 Directional Interpolation

The remaining step in evaluation of the limiting path radiance is a directional interpolation. The reasoning behind this step is that instead of computing l'_m directly based on Eq. (104), this equation requires an interpolation over all incident directions each time it is invoked. An alternative method of evaluating l'_m would be to translate the results produced at the discrete ordinates directions into some other, higher order representation. In this representation, more efficient methods, using a smaller set of nearest neighbor points, could be used. One such possibility is to generate a series of points at equally spaced meridians.

81

A splined fit can then be performed along each meridian, and results at different meridians can then be further splined. Other methods are possible as well; for example, one may desire to transform from the set of discrete ordinate directions to a separate set of new directions which also span the unit sphere. To make this transformation, a spherical harmonics method is invoked.

Let us define a set of orthonormal functions on the unit sphere which shall be referred to as even and odd spherical harmonic functions:

$$Z_{\ell m}^e(\mu,\,\phi) = \sqrt{\frac{2\ell+1}{4\pi}\,(2-\delta_{m0})\,\frac{(\ell-m)!}{(\ell+m)!}}\,P_\ell^m(\mu)\,\cos(m\phi), \qquad (105)$$

$$Z_{\ell m}^o(\mu,\,\phi) = \sqrt{\frac{2\ell+1}{4\pi}\,2\,\frac{(\ell-m)!}{(\ell+m)!}}\,P_\ell^m(\mu)\,\sin(m\phi), \qquad (106)$$

where μ is the cosine of the zenith angle, ϕ is an azimuthal angle, $\ell \geq m \geq 0$, and where $P_\ell^m(\mu)$ is the associated Legendre polynomial, which can be given in terms of Rodrigues' formula as (Jackson 1975),

$$P_\ell^m(\mu) = \frac{(-1)^m}{2^\ell\,\ell!}\,(1-\mu^2)^{m/2}\,\frac{d^{\ell+m}}{d\mu^{\ell+m}}(\mu^2-1)^\ell. \qquad (107)$$

These functions have the properties of orthogonality when integrated over 4π steradians:

$$\int_{4\pi} d\Omega\,Z_{\ell' m'}^e(\mu,\,\phi)\,Z_{\ell m}^e(\mu,\,\phi) = \delta_{\ell'\ell}\,\delta_{m'm}; \qquad (108)$$

$$\int_{4\pi} d\Omega\,Z_{\ell' m'}^o(\mu,\,\phi)\,Z_{\ell m}^o(\mu,\,\phi) = \delta_{\ell'\ell}\,\delta_{m'm}\,(1-\delta_{m0}); \qquad (109)$$

$$\int_{4\pi} d\Omega\,Z_{\ell' m'}^o(\mu,\,\phi)\,Z_{\ell m}^e(\mu,\,\phi) = 0, \qquad (110)$$

where δ_{ij} is a kronecker delta function of indices i and j.

These functions are similar to those used by Zardecki (1995), but contain different normalization factors, which tend to somewhat simplify the mathematics. Note that these spherical harmonics functions are always real valued. This is significant because we want to exclude imaginary results, since we are dealing with strictly real valued radiances.

Because of these properties, a function of direction may be expanded as:

$$I(\mu,\,\phi) = \sum_{\ell=0}^{\infty} \sum_{m=0}^{\ell} A_{\ell m}^e\,Z_{\ell m}^e(\mu,\,\phi) + A_{\ell m}^o\,Z_{\ell m}^o(\mu,\,\phi); \qquad (111)$$

where the $A_{\ell m}$ coefficients are determined using,

$$A_{\ell m}^e = \int\limits_{4\pi} d\Omega \, Z_{\ell m}^e(\mu, \, \phi) \, I(\mu, \, \phi); \tag{112}$$

$$A_{\ell m}^o = \int\limits_{4\pi} d\Omega \, Z_{\ell m}^o(\mu, \, \phi) \, I(\mu, \, \phi). \tag{113}$$

However, due to the characteristics of the discrete ordinates approach, these coefficients can be determined using the summation results:

$$A_{\ell m}^e = \frac{\pi}{2} \sum_{i=1}^{M} w_i \, Z_{\ell m}^e(\mu_i, \, \phi_i) \, I_i; \tag{114}$$

$$A_{\ell m}^o = \frac{\pi}{2} \sum_{i=1}^{M} w_i \, Z_{\ell m}^o(\mu_i, \, \phi_i) \, I_i, \tag{115}$$

where we recall from section 2.2 that M (equals $N(N+2)$) is the number of streams in a discrete ordinates model.

If one, therefore, desired to determine the radiance results (I_j) in a series of directions $\hat{\Omega}_j$, the transform mechanism for converting from the sampled directions I_i to the output directions I_j could be expressed as a matrix multiplication:

$$I_j = \sum_{i=1}^{M} X_{ji} \, I_i, \tag{116}$$

where

$$X_{ji} = \frac{4\pi w_i}{8} \sum_{\ell=0}^{L} \sum_{m=0}^{\ell} \left[Z_{\ell m i}^e \, Z_{\ell m j}^e + Z_{\ell m i}^o \, Z_{\ell m j}^o \right] \tag{117}$$

is obtained by rearranging the order of the summations in Eqs. (111), (114), and (115), and $Z_{\ell m i}^e = Z_{\ell m}^e(\mu_i, \, \phi_i)$, $Z_{\ell m i}^o = Z_{\ell m}^o(\mu_i, \, \phi_i)$. The only restriction placed on this method is that the value of the summation limit L used in Eq. (117) must be chosen such that all equations of form (108) through (110) integrate properly under the stream expansion chosen. That is, we require,

$$\frac{4\pi}{8} \sum_{i=1}^{M} w_i \, Z_{\ell' m'}^e(\mu_i, \, \phi_i) \, Z_{\ell m}^e(\mu_i, \, \phi_i) \approx \delta_{\ell' \ell} \, \delta_{m' m}; \tag{118}$$

$$\frac{4\pi}{8} \sum_{i=1}^{M} w_i \, Z_{\ell' m'}^o(\mu_i, \, \phi_i) \, Z_{\ell m}^o(\mu_i, \, \phi_i) \approx \delta_{\ell' \ell} \, \delta_{m' m} \, (1 - \delta_{m0}); \tag{119}$$

83

$$\frac{4\pi}{8} \sum_{i=1}^{M} w_i \, Z_{\ell' m'}^{o}(\mu_i, \, \phi_i) \, Z_{\ell m}^{e}(\mu_i, \, \phi_i) \approx 0. \tag{120}$$

This requirement leads to the interesting conclusion that, while we have assumed that if $M = N(N+2)$, our phase function expansion was valid to $L = N$, direct calculations show that the interpolation criteria above are only valid through $L = N/2$.

Using the above technique, the radiance data produced by the radiative transfer code may be interpreted for any desired direction.

In summary, we may conclude that transmittances and limiting path radiances for individual path segments can be computed along any path within the modeled scattering volume, leading to a constructive method for evaluating path transmittances and integrated path radiances for arbitrary geometries. The remaining aspects of propagating information for image rendering purposes are relating the image geometry to a given path within the scattering volume and relating the radiances produced by the scattering model to pixel data placed in the image file. These aspects are discussed in the next two sections.

4.5 Viewing Geometries

In perspective viewing, the origin point for each pixel is some image plane within the observer's optical system. The simplest such system, and the one adopted here for our case study, is a pinhole camera where the image plane is placed perpendicular to the primary viewing axis, and each LOS is viewed as passing out of the camera through the center of the lens into the modeled volume. In orthographic rendering, the origin of each LOS can be a point in a plane from which parallel lines of sight are drawn through the volume of interest. In perspective viewing, the lines of sight naturally diverge after passing through the 'lens' to span a particular solid angle view of the volume of interest.

Regardless of this distinction, each LOS will trace its way through a unique sample of the modeled scattering volume until it either exits the volume through the top of the modeled region (the 'roof'), impacts the modeled surface (the 'floor'), or reaches some preselected maximum range after which the computation is truncated. This latter step is usually necessary to control computation time in an application.

Any LOS that crosses upward through the roof is assumed to see only background atmosphere with a brightness characterized by a directionally dependent background sky color. An LOS which strikes the surface, on the other hand, can be represented using any of a series of possible models to include a constant reflectivity surface, user-designed surface objects, reflectivity mappings, etc.

4.6 Radiance to Pixel Value Conversions

Once means of representing the upper and lower bounding surfaces have been chosen, it will be necessary to convert path radiance values given in physical units into image related pixel values. This process involves the use of conversion factors.

To understand where `AIM` derives its radiance information, we begin with another `AIM` model input. To initialize the radiance information `AIM` runs an Electro-Optical Systems Atmospheric Effects Library (Shirkey *et al.* 1987) (EOSAEL) configured version of the Air Force's `MODTRAN` model (Berk *et al.* 1989) to determine the direct (solar) irradiance and directionally dependent diffuse radiances of the sky background at the top of the modeled volume in each of the downward welling stream directions. Using these values along with the interpolation technique described in section 4.4, one can determine the sky radiance in any direction. Call this amount $R_U(\hat{\Omega})$. Due to the nature of `MODTRAN`, R_U will **only** be a function of direction, not position. Once an LOS crosses upward out of the volume, using the integration convention described in section 4.2, we would simply add in a final step to the path integration procedure (call it $N + 1$), where $s'_{N+1} = \infty$, $\tilde{t}'_{N+1} = 0$, and $l'_{N+1} = R_U$. Thus there is no transmission beyond this final step, and R_U becomes the background radiance. Depending on how high above the surface one wanted to simulate embedded (flying) objects, other options are also available but might involve running larger simulation volumes.

For downward directed LOS, we need to consider lines that pass through the ground plane. To accomplish this task, we need to know the properties of the surface to be modeled as well as the simulated ambient illumination at each surface point. To evaluate this ambient illumination, consider that at each surface point there will be a set of downward directed streams which can be integrated over solid angle and cosine weighted to produce a net diffuse flux. The direct irradiance can be computed as well, resulting in a net irradiance at the base of the modeled volume beneath the last layer of modeled cells. Currently we assume the surface is a Lambertian reflector. Thus the reflected radiance can be evaluated by dividing the net incident flux by π and multiplying by a surface reflectivity α.

The `BLITS` model can accept positionally varying surface reflectivity, but this is not the general usage of the model. Instead, an average surface reflectivity is usually applied to the entire surface. Using this approach, the radiance fields produced can be translated across the terrain, reflecting the first order effects of wind motion of the cloud field. Most terrain variations will average out over the 250 m cell lengths involved in the RT calculations.

Taking this approach, assume for a given region of the surface that there is a known mean reflectivity $\bar{\alpha}$. Assume also that there is an image of the surface available. Define α_m as the reflectivity of the zero pixel value and α_M as the reflectivity of the maximum possible pixel value. Also assume the image has not

been distorted in some way, such as by a gamma correction. Thus the image brightness is considered to vary linearly according to pixel value, and that this linearity is related to pixel reflectivity.

We have thus discussed means of representing the upper and lower boundaries of the rendered scene using previously available image data and radiance information from MODTRAN. The following section completes the information on rendering techniques.

4.7 Cloud Rendering Algorithm

In previous sections we described the means of tracing paths through the scattering volume. However, as is often the case, this technique is not without difficulties. These difficulties arise due to the level of complexity of the problem addressed. For a tactically significant scenario, we would like to treat a volume on the order of several kilometers in each horizontal direction. In addition, we need to extend the modeled scattering volume from the surface, where the majority of tactically significant (from an Army point of view) lines of sight exist, up through a level that encompasses the majority of significant cloud features. This extension vertically is necessary because cloud shadowing can have significant effects on the illumination of the target and also the LOS, significantly affecting path radiance.

The difficulty with extending the scenario to encompass a tactically significant volume is that once it has been sufficiently extended, the small feature data in the clouds themselves often cannot be adequately characterized during the radiative transfer calculation. In our typical scenario a volume with 8 km horizontal by 4 km vertical dimensions is modeled using $\Delta =1/4$ km per cell. But, this cell size is often the size of actual clouds. Thus, a cloud may be modeled by only a single cell. This can lead to significant problems when attempting to visualize such a cloud. Without additional information the cloud will appear as a cube.

To avoid this problem, an observation made by Hoock and Giever (1989) was utilized. This observation was that limiting path radiance varies more slowly than path radiance, since path radiance depends on the specific density structure of the medium, but limiting path radiance reflects the presence of available illumination. In most clouds, the illumination is due to scattered energy, which becomes rather uniform due to the highly scattering nature of most cloud aerosols. This suggests that the radiance calculations in the radiative transfer model can be run at a coarser resolution than is needed by the density map of the medium.

To generate the 3D extinction mapping of the scattering medium, the AIM preprocessing stage runs the Air Force's Cloud Scene Simulation Model (CSSM). At its heart this model contains a fractal density generator and fractal statistics for various cloud types. From the AIM input interface, a user can select characteristics of the cloud field to be generated, including the base heights,

layer thicknesses, cloud types, and cloud fractions of up to three layers of non-cumulus clouds and one cumulus cloud layer. `AIM` then runs `CSSM` at four times the resolution of that required by the `BLITS` RT code. The full resolution data generated by `CSSM` are then transformed to extinction information which can be used in visualizations. The data are then also coarsened using a spatial averaging function for use by `BLITS`.

A rendering code was then developed to access the output from the RT code and the 3D extinction mapping. The various techniques for generating pixel modifications, angular interpolation, and point-to-point integrations were employed. The model developed was tailored to generate orthographic renderings of the scattering volume. The model entails two separate calculation stages. In the first, a series of lines of sight are traced through the volume. In the second, these results are used as interpolation points for generating values at every pixel position.

In the first phase, the 1/16 km resolution `CSSM` output is used in combination with the 1/4 km resolution `BLITS` model output. For a given observer location on the outside of the modeled volume, there will be at most three outside walls of the volume that are visible. Normally, these walls cover a simulated 8 km×8 km footprint on the ground and are 4 km high. They are sampled at the same 1/16 km resolution as output from the `CSSM` code. Thus, on a vertical side wall 8 km wide and 4 km high, there are 128×64 sample lines of sight traced through the volume. On a top or bottom wall there will be 128×128 sample points. Each LOS is traced to determine net transmission and path radiance for each of three color channels.

Following these LOS calculations, the program uses this data set to evaluate the results for each pixel. A given pixel will be characterized by a path through the volume. A Gaussian weighting scheme is used to interpolate the results for pixels falling between LOS calculations made in the previous phase. This technique provides a smooth transition between effects calculated for the sample points, as characterized by the width of the Gaussian blending functions. Care must be taken in selecting an appropriate width parameter, since a width parameter that is too small will produce grainy results where only the closest sample LOS calculation can influence the result. A width parameter which is too large will cause clouds to appear too smooth and can greatly slow down the interpolation algorithm.

For a rendering algorithm, one must also describe the appearance of the surface or sky backgrounds. We have created a separate file that lists the incident direct and diffuse radiances present at each point beneath the scattering volume for each sensor color channel. Let us call the combined channel irradiance $V_{i,j,k}$, where i and j represent the horizontal position across the terrain, and k represents the color channel index. As an example, a color sensor receiving data on red, green, and blue channels has k values of 1, 2, and 3. Let us also define surface color channel reflectivities ($\alpha_{i,j,k}$), resulting in reflected energy, $\alpha_{i,j,k}V_{i,j,k}$ at each (i, j) point along the surface and for each color channel k.

For upward directed paths, there are corresponding values to be applied for sky radiance color channel based on the description given in section 4.6. The last step is then to apply the transmittance and path radiance effects interpolated from the initial data set to the background pixel values just determined.

The results of these processing stages are a full set of real number results at each pixel position for the color channel radiance results. The final step necessary is to rescale these results such that they are remapped into a range that does not exceed the maximum pixel value possible in any color channel. To accomplish this step requires two passes through the pixel-based data set. The first step involves determining the maximum pixel value at any channel and then using this as a normalizing factor in the second stage.

Sample outputs from this algorithm are seen in figures 44 through 46. The scenario modeled uses a green, 20-percent reflective, terrain surface for the base of the volume. The cloud field is that for a 35 percent cumulus cloud cover. The cloud field has been computed such that it is horizontally periodic. Thus clouds that begin on one side or corner of the volume wrap around to the opposite edge. This technique was deemed preferable to either (a) modeling very large volumes or (b) modeling clouds which simply cut off at the boundaries of the volume.

Orthographic views of the scattering volume are shown in figures 44 through 46 as seen from the top, side, and below. An afternoon time is modeled, resulting in illumination on the western side of the clouds. Dark regions appear on some clouds because the horizontal periodicity results in some clouds on the eastern edge shading clouds near the western edge. In particular, note the shadowed cloud tops in the center of figure 44. Figure 45 reveals that the cloud tops of the clouds on the eastern edge (in the background in figure 45) are actually taller than the clouds in the center. They thus shadow the clouds in the center due to the horizontal periodicity. Cloud shadows also result in surface brightness variations, which show up better on the computer screen than on hard copy.

4.8 FastVIEW Data Formats

The `AIM` codes utilize a data formatting and compression technique developed, but not formally documented, in 1994 for the Defense Modeling and Simulation Office's (DMSO) Environmental Effects for Distributed Interactive Simulations (E^2DIS). In that effort, an attempt was made to generate common, useable, yet compact data sets. The name established for these data sets was FastVIEW, reflecting the relationship between their source, the Weather and Visualization Effects for Simulations' (WAVES) model `VIEW` and an attempt to utilize data output by that model in a rapid manner. We now provide the documentation formally for that format in this section in hopes that others can design uses that provide faster rendering of images using these sets. Originally, these formats consisted of only two data set types. We have expanded these to three here
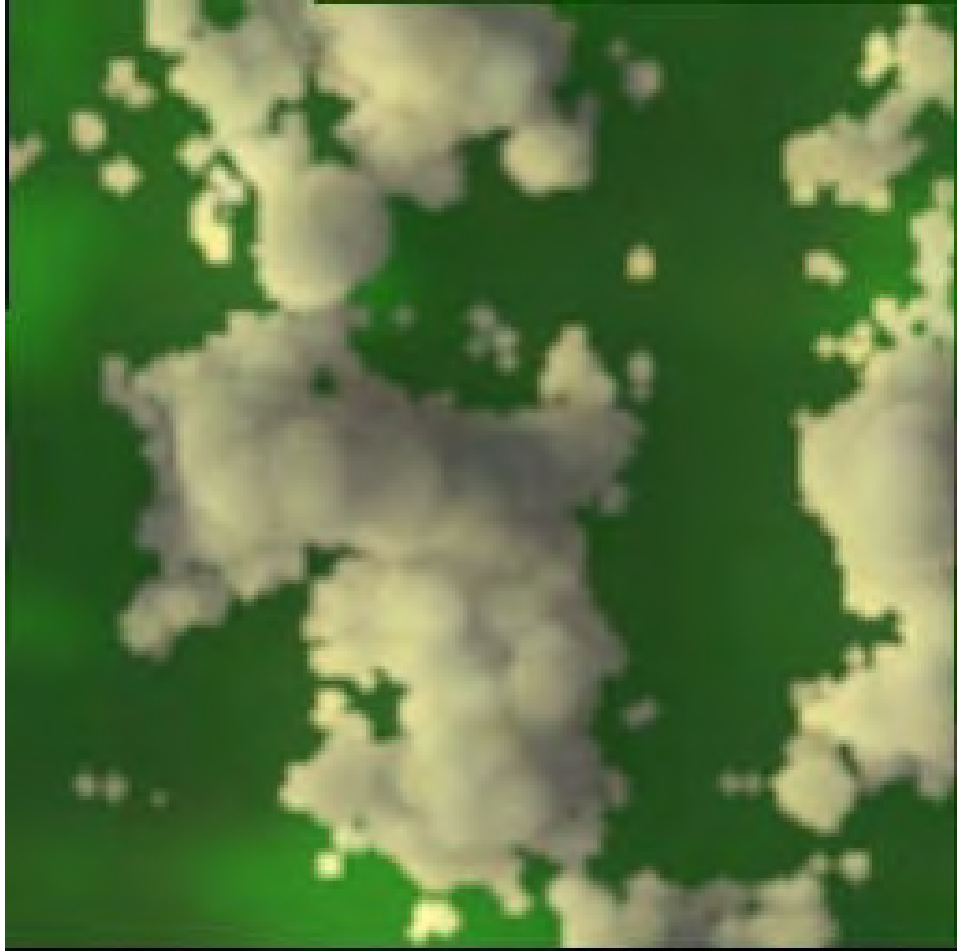
Figure 44. Visualization of a 35 percent cloud cover cumulus layer. View is from directly above using an orthographic rendering technique. North is at the top of the figure.

Figure 45. Visualization of a 35 percent cloud cover cumulus layer. View is from the western side of the volume looking east using an orthographic rendering technique.
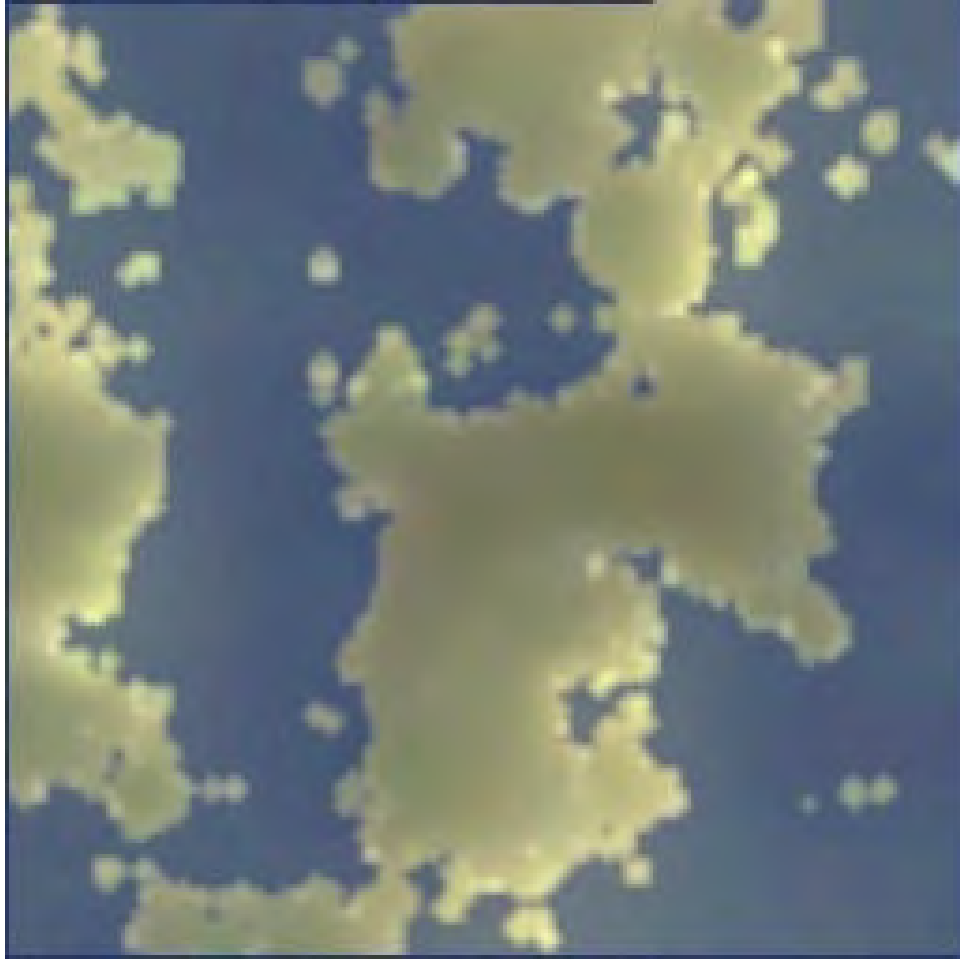
Figure 46. Visualization of a 35 percent cloud cover cumulus layer. View is from directly below using an orthographic rendering technique. North is at the top of the figure.

to reflect the need for a higher density extinction map useable by a rendering engine.

These data types now consist of the file types: EX.OUT, IL.OUT, and FV.CPD. The first provides information on the density map of the volume. The second is a surface illumination map. The third provides volumetric, directional, and spectral radiance information.

4.8.1 EX.OUT

The extinction file, EX.OUT, provides a 3D spectral mapping of the scattering volume's extinction coefficient mapping. As explained in the previous section, the RT code is run on a coarse grid to conserve memory and time. This information is then coupled to a higher resolution map of the extinction. The EX.OUT file provides that map.

The EX.OUT file itself consists of two sections, a header containing information about the volume and spectral resolutions, and the data itself. A typical header

is seen below:

```
EXTC              1.0000
XDIS              0.0625
NNXX            128.0000
YDIS              0.0625
NNYY            128.0000
ZDIS              0.0625
NNZZ             64.0000
NNCC              1.0000
```

These lines represent the following information: The first line merely identifies the file type as an `EX.OUT` file; the second, fourth, and sixth lines indicate the cell resolutions in kilometers; the third, fifth, and seventh lines indicate the number of cells in the three directions; and the last line indicates the number of spectral channels. The data body which follows the header section is listed according to spectral channel, x, y, and z in order from most to least rapidly varying cell index. In our convention, x is always increasing toward the east, y increases toward north, and z is a vertical variable measured as height above the surface.

4.8.2 IL.OUT

The surface illumination file type, `IL.OUT`, is similar to the extinction file except that there are only two dimensions in the data and there is more than one data element per line in the body of the output. Here is a listing of a typical header:

```
ILUM              1.0000
XDIS              0.2500
NNXX             32.0000
YDIS              0.2500
NNYY             32.0000
NNCC              3.0000
DZEN             49.7397
DAZI            173.8699
```

The data listed for this file are the direct and diffuse fluxes for each surface region. The data are organized in the same format as the `EX.OUT` results: spectral channel, x, and y in order of nesting from deepest to outer (y). Note that these results are produced in some cases by weighing the computed radiances at the surface according to their incident cosine, solid angle for diffuse quantities, and spectral weighting function.

As an example of a spectral weighting function, consider the human eye. Middleton (1952) discusses the characteristics of the eye's photopic and color spectral response curves. Let these be characterized by functions $S_c(k)$, where k is the wavenumber and c is the color channel index. These curves are normalized

such that $\int_0^\infty S_c(k)\,dk = 1$. Hence, an input signal of $E(x, y, k)$ in either diffuse or direct flux produces

$$I_c = \int\limits_0^\infty S_c(k)\, E(x, y, k)\, dk. \tag{121}$$

To tailor these responses for use with image rendering products, we typically convert the I_c values to NTSC RGB metrics using the transform $R = NI$, where N is the matrix,

$$N = \begin{pmatrix} 1.910 & -0.533 & -0.288 \\ -0.985 & 2.000 & -0.028 \\ 0.058 & -0.118 & 0.896 \end{pmatrix}. \tag{122}$$

Users should note that in this form the effects of sensor weighting have already been accounted for once. In using these results for color scene rendering, one needs to use terrain reflectance coefficients that do not themselves also contain sensor weighting factors or the sensor effects would be applied twice.

4.8.3 FV.CPD

The final output form is the FastVIEW compressed file type. This file consists of three main sections: a header, a series of directional templates, and the main data listing. Of these, the first section is virtually identical to the EX.OUT style header. An example is given below:

FSVU	1.0000
XDIS	0.2500
NNXX	32.0000
YDIS	0.2500
NNYY	32.0000
ZDIS	0.2500
NNZZ	16.0000
STDR	0.0625
NNCC	3.0000
NDCL	128.0000

Note that the differences include the file type identifier (FSVU in this case), the STDR identifier, and the NDCL identifier. The STDR identifier defines the standard range used in the computations of the transmission factors contained in the general output section. The NDCL identifier defines the number of directional templates included in the template section.

Each template currently consists of 43 items of data: the template index number followed by 42 directional values. These values range from zero to 32767 ($2^{15} - 1$) and describe the directionally varying nature of the limiting path radiance. To use these results an accessing algorithm has been written in C++. In this

algorithm, the set of templates is described by a matrix D_{ij}, where i is the template index and j is the direction. In the main positional data listing, for each location and sensor spectral channel, a single number is used to indicate the template to use to describe limiting path radiance directional variability, $i(x, y, z, c)$. Also, a single number is used to define the maximum limiting path radiance in any direction at that point, $L_m(x, y, z, c)$. To determine the actual limiting path radiance in one of the canonical directions j, one evaluates $L_m(x, y, z, c) D[i(x, y, z, c), j]/32767$. Intermediate directions can be evaluated by any of a number of interpolation techniques. The C++ routine mentioned has the full description of each of the 42 directions and means of interpolation.

Following the template listing is the main section of the data. This listing consists of data in a different order from the EX.OUT listing: x, y, z, color channel, in order from outer to inner loops. Each data line contains four elements: the spectral extinction coefficient, a transmittance factor, a maximum limiting path radiance, and a directional template index number. The transmittance factor is generated based on the path length value (in km) given in the header, which can be used to step through the cloud field. In the current implementation, STDR is always set at 0.0625 km.

5. Discussion and Conclusions

In the previous sections we have shown a method for producing radiometrically correct three-dimensionally inhomogenous cloud scenes using a cell-surface-based DOMRT code. This code has the advantage that energy conservation is imposed automatically. Also, interpretation of diffuse radiance and scattering in any direction is obtained using spherical harmonics expansions and the discrete ordinates choices of stream directions. Diffuse, direct, and blackbody-emitted energies are all treated in a consistent manner. This method does not share the disadvantages of Fourier methods regarding memory, nor does it share the limitations of the original DOM in regard to treating only low-density media, nor the diffusion approximation's limitation to dense and isotropically scattering media. Finally, physically realistic cloud scene rendering is possible using results determined by the RT routine.

The performance of these models using current computer resources is hopeful. Using an R4400 chip SGI, the runtime for the radiative transfer routine spanning seven wavebands across the visible spectrum is on the order of 1 hour. Postprocessing of the outputs to compress the information to color channels and allow for rapid directional interpolation requires about 1 additional hour. Rendering of images currently takes approximately 3 to 5 min per frame. However, considering that no parallelization has been attempted on these codes and much faster machines are becoming available, it is possible that true 3D color simulations of radiometrically correct cloud fields are possible in the near future. The compression techniques employed are also useful in that they tend to limit the amount of memory that must be dedicated to running such LOS calculations.

This method has been integrated with an intuitive scenario generator within `AIM`. This section of the code allows the characterizing of a particular scenario using a minimum of parameters while automatically processing all the needed information to allow the rendering of the scenario volume by the rendering engine. Intermediate output files needed to render the volume from different directions are archived to facilitate additional simulation tasks. We have implemented a version of this software within the DoD DMSO-sponsored Master Environmental Library program (`http://www-mel.nrlmry.navy.mil/`), permitting the on-line access and delivery of such files. We have also established a web site providing color examples of the images that can be created using this technique (`http://www-mel.arl.mil/MEL/rad/r0.html`).

AIM allows a user to produce any number of different cloud scenarios for visualization purposes and provides choices in terms of cloud representation within the RT code. This code accesses databases of MODTRAN horizontally homogeneous background aerosols profiles. The EOSAEL configured version of MODTRAN is itself run several times to initialize the volume upper boundary with information regarding downwelling diffuse stream radiance and direct illumination as well as being used to compute vertical components of background molecular absorption coefficients. It also calls the Air Force CSSM code to generate a cloud density field.

AIM uses a solar/lunar calculation routine to determine whether the Sun or the Moon is the source of direct illumination. Whenever the Sun is above the horizon it is used as the direct source. If the Sun is below the horizon and the Moon is above the horizon, then the Moon is used as the direct source. Appropriate changes to inputs parameters used in the calls to the MODTRAN routine are used to reflect the conditions to be simulated.

AIM also uses information gleaned from the PFNDAT series of aerosols contained in EOSAEL. This series of aerosols covers the majority of surface-based precipitation types (not treated under the current version of AIM), hazes, fogs, and munition smokes. In addition to these aerosols, a sequence of upper-level cloud aerosols were run through the AGAUS Mie scattering phase function calculation routine to produce PFNDAT-clone outputs. The PFNDAT files and the clone results were then processed through a routine to analyze the optimal Legendre polynomial representation for the 24-stream model using the technique described in the appendix.

The issue of cloud and haze visualization is a field of intense current interest. Though many current and planned simulations attempt to treat cloud effects, these seldom treat clouds in radiometrically correct fashion or consider fully three-dimensional influences. More often than not, the appearance of clouds are handled as merely pictures that have been artificially embedded in a scene, without regard to their feedback interactions with scene features such as via cloud shadow effects or via limiting path radiance variations produced by shafts of sunlight extending through gaps in the cloud layers.

The codes described here are far more robust. In the future, the processing speed of these codes can be greatly enhanced using parallel processing techniques, novel rendering techniques, and increased computer memory.

References

Berk, A., L. S. Bernstein, and D. C. Robertson, *MODTRAN: A Moderate Resolution Model for LOWTRAN 7*, GL-TR-89-0122, U.S. Air Force Geophysics Laboratory, Hanscom Air Force Base, MA, 1989.

Byrne, R. N., R. C. J. Somerville, and B. Subasilar, "Broken-Cloud Enhancement of Solar Radiation Absorption," *J. Atmos. Sci.*, **53**, p. 878-886, 1996.

Carlson, B. G., and K. D. Lathrop, "Transport Theory: the Method of Discrete Ordinates," in *Computing Methods in Reactor Physics* edited by H. Greenspan, C. H. Kelber, and D. Okrent, Gordon and Breach, New York, pp. 171-266, 1968.

Chai, J. C., H. S. Lee, and S. V. Patankar, "Improved Treatment of Scattering Using the Discrete Ordinates Method," *Transactions of the ASME*, **116**, p. 260-263, 1994.

Chandrasekhar, S., *Radiative Transfer*, Dover Publications, New York, 1960.

Davies, R., "The Effect of Finite Geometry on the Three-Dimensional Transfer of Solar Irradiance in Clouds," *J. Atmos. Sci.*, **35**, p. 1712-1725, 1978.

Davis, J. M., "Azimuthal Variability in the Sky-to-Ground Ratio," *Proceedings of the Sixth Annual EOSAEL/TWI Conference*, p. 377-386, Las Cruces, NM, 1986.

Davis, J. M., "The Role of Surface Reflectance Functions in Visible Contrast Calculations," *Proceedings of the Seventh Annual EOSAEL/TWI Conference*, p. 403-416, Las Cruces, NM, 1987.

Deirmendjian, D., *Electromagnetic Scattering on Spherical Poly-dispersions*, Elsevier, New York, 1969.

El Wakil, N., and J. F. Sakadura, "Some Improvements of the Discrete Ordinates Method for the Solution of the Radiative Transfer Equation in Multidimensional Anisotropically Scattering Media," *Developments in Radiative Heat Transfer*, ASME, **HTD-203**, p. 119-127, 1992.

Fiegel, R. P., *Natural Aerosol Extinction Module, XSCALE92 User's Guide*, ARL-TR-273-1, U.S. Army Research Laboratory, White Sands Missile Range, NM, 1994.

Fiveland, W.A., "Discrete-Ordinates Solutions of the Radiative Transport Equation for Rectangular Enclosures," *ASME-J. of Heat Transfer*, **106**, p. 699-706, 1984.

Fiveland, W. A., "Discrete Ordinates Methods for Radiative Heat Transfer in Isotropically and Anisotropically Scattering Media," proceedings of the *23th National Heat Transfer Conference*, Denver, CO, August 4-7, 1985, *ASME*, NY 1985.

Fiveland, W. A., "Three-Dimensional Radiative Heat Transfer Solutions by the Discrete-Ordinates Method," proceedings of the *24th National Heat Transfer Conference and Exhibition*, Pittsburgh, PA, August 9-12, 1987, *ASME*, NY, 1987.

Fiveland, W. A., "The Selection of Discrete Ordinate Quadrature Sets for Anisotropic Scattering," *HTD,* **160**, *Fundamentals of Radiation Heat Transfer,* *ASME*, NY, pp. 89-96, 1991.

Gerhart, G., T. Meitzler, E. Sohn, G. Witus, G. Lindquist, and R. Freeling, "Verification and Validation Status of the TARDEC Visual Model (TVM)," *Proceedings of the Sixth Annual Ground Target Modeling and Validation Conference*, p. 228-238, Houghton, MI, 1995.

Gerstl, S. A. W., and A. Zardecki, "Discrete-ordinates finite-element method for atmospheric radiative transfer and remote sensing," *Appl. Opt.*, **24**, p. 81-93, 1985a.

Gerstl, S. A. W., and A. Zardecki, "Coupled atmosphere/canopy model for remote sensing of plant reflectance features," *Appl. Opt.*, **24**, p. 94-103, 1985b.

Gube, M., J. Schmetz, and E. Raschke, "Solar radiative transfer in a cloud field," *Contr. Atmos. Phys.*, **53**, p. 23-34, 1980.

Haferman, J. L., W. F. Krajewski, T. F. Smith, and A. Sánchez A., "Radiative Transfer for a Three-Dimensional Raining Cloud," *Appl. Opt.*, **32**, p. 2795-2802, 1993.

Hoock, D. W., and R. A. Sutherland, "Obscuration Countermeasures," chapter 6 of *The IR & EO Systems Handbook, Volume 7, Countermeasure Systems*, D. Pollock, ed., ERIM and SPIE Press, Ann Arbor, MI, 1993.

Jackson, J. D., *Classical Electrodynamics*, J. Wiley & Sons, New York, 1975.

Joseph, J.H., W.J. Wiscombe, and J.A. Weinman, "The delta-Eddington Approximation for Radiative Flux Transfer," *J. Atmos. Sci.*, **33**, p. 2452-2459, 1976.

Kobayashi, T., "Reflected Solar Flux for Horizontally Inhomogeneous Atmospheres," *J. Atmos. Sci.*, **48**, p. 2436-2447, 1991.

Lafore, R., *The Waite Group's object-oriented programming in Turbo C++*, Waite Group Press, Mill Valley, CA, 1991.

Lathrop, K. D., and B. G. Carlson, "Discrete Ordinate Angular Quadrature of the Neutron Transport Equation," *Los Alamos Scientific Laboratory Report 3186,* Los Alamos, NM, 1965.

Lee, M. A., and S. J. LaMotte, "Loss Exchange Ratio Sensitivity to Variations of Sky-to-Ground Radiance in a Combat Simulation," *Proceedings of the Eleventh Annual EOSAEL/TWI Conference,* p. 187-196, Las Cruces, NM, 1991.

LeNoble, J., ed., *Radiative Transfer in Scattering and Absorbing Atmospheres: Standard Computational Procedures,* A. Deepak Pub., Hampton, VA, 1985.

Lentz, W. J., "Generating Bessel Functions in Mie Scattering Calculations Using Continued Fractions," *Applied Optics,* **15**, p. 668-671, 1976.

Lewis, E. E., and W. F. Miller, *Computational Methods of Neutron Transport,* Wiley Interscience, New York, 1984.

Li, J., D. J. W. Geldart, and P. Chylek, "Perturbation Solution for 3D Radiative Transfer in a Horizontally Periodic Inhomogeneous Cloud Field," *J. Atmos. Sci.,* **51**, p. 2110-2122, 1994a.

Li, J., D. J. W. Geldart, and P. Chylek, "Solar Radiative Transfer in Clouds with Vertical Internal Inhomogeneity," *J. Atmos. Sci.,* **51**, p. 2542-2552, 1994b.

Liou, K.N., *Radiation and Cloud Processes in the Atmosphere,* Oxford University Press, New York, p. 127, 1992.

Low, R. D. H., and S. G. O'Brien, *EOSAEL 87, Cloud Transmission Module, CLTRAN,* ASL-TR-0221-9, U.S. Army Atmospheric Sciences Laboratory, White Sands Missile Range, NM, 1987.

McKee, T. B., and S. K. Cox, "Scattering of Visible Radiation by Finite Clouds," *J. Atmos. Sci.,* **31**, p. 1885-1892, 1974.

McKellar, B. H. J., and M. A. Box, "The scaling group of the radiative transfer equation," *J. Atmos. Sci.,* **38**, p. 1063-1068, 1981.

Middleton, W. E. K., *Vision through the Atmosphere,* Univ. of Toronto Press, Toronto, CA, 1952.

Miller, A., *Mie Code AGAUS 82,* ASL-CR-83-0100-3, U.S. Army Atmospheric Sciences Laboratory, White Sands Missile Range, NM, 1983.

Myneni, R. B., G. Asrar, and S. A. W. Gerstl, "Radiative transfer in three dimensional leaf canopies," *Trans. Theory Stat. Phys.,* **19**, p. 205-250, 1990.

Myneni, R. B., A. Marshak, Y. Knyazikhin, and G. Asrar, "Discrete ordinates method for photon transport in leaf canopies," in *Photon-Vegetation Interactions,* edited by R. B. Myneni and J. Ross, Springer-Verlag, New York, pp. 45-110, 1991.

Nakajima, T., and M. Tanaka, "Algorithms for Radiative Intensity Calculations in Moderately Thick Atmospheres Using a Truncation Approximation," *J. Quant. Spectrosc. Radiat. Trans.,* **40**, p. 51-69, 1988.

Potter, J., "The delta Function Approximation in Radiative Transfer Theory," *J. Atmos. Sci.*, **27**, p. 943-949, 1970.

Preisendorfer, R. W., and G. L. Stephens, "Multimode Radiative Transfer in Finite Optical Media. I: Fundamentals," *J. Atmos. Sci.*, **41**, p. 709-724, 1984.

Schaller, E., "A delta-Two-Stream Approximation in Radiative Flux Calculations," *Contrib. Atmos. Phys.*, **52**, p. 17-26, 1979.

Shettle, E. P., and R. W. Fenn, *Models for the Aerosols of the Lower Atmosphere and the Effects of Humidity Variations on Their Optical Properties*, AFGL-TR-79-0214, U.S. Air Force Geophysics Laboratory, Hanscom Air Force Base, MA, 1979.

Shirkey, R. C., L. D. Duncan, and F. E. Niles, *EOSAEL 87, Executive Summary*, ASL-TR-0221-1, U.S. Army Atmospheric Sciences Laboratory, White Sands Missile Range, NM, 1987.

Stamnes, K., and R. A. Swanson, "A New Look at the Discrete Ordinate Method of Radiative Transfer Calculations in Anisotropically Scattering Atmospheres," *J. Atmos. Sci.*, **38**, p. 387-399, 1981.

Stamnes, K., S-C. Tsay, W. Wiscombe, and K. Jayaweera, "Numerically stable algorithm for discrete-ordinate-method radiative transfer in multiple scattering and emitting layered media," *Appl. Opt.*, **27**, p. 2502-2509, 1988.

Stark, H., and J. W. Woods, *Probability, Random Processes, and Estimation Theory for Engineers*, Prentice-Hall, Englewood Cliffs, NJ, 1986.

Stephens, G. L., "Radiative Transfer in Spatially Heterogeneous, Two-Dimensional, Anisotropically Scattering Media," *J. Quant. Spectrosc. Radiat. Trans.*, **36**, p. 51-67, 1986.

Stephens, G. L., "Radiative Transfer through Arbitrarily Shaped Optical Media. Part I: A General Method of Solution," *J. Atmos. Sci.*, **45**, p. 1818-1836, 1988.

Tofsted, D. H., B. T. Davis, A. E. Wetmore, J. Fitzgerrel, R. C. Shirkey, and R. A. Sutherland, *EOSAEL92, Aerosol Phase Function Data Base PFNDAT*, ARL-TR-273-9, U.S. Army Research Laboratory, White Sands Missile Range, NM, 1997.

van de Hulst, H. C., *Multiple Light Scattering, Tables, Formulas, and Applications, Volumes 1 and 2*, Academic Press, New York, 1980.

Welch, R. M., and B. A. Wielicki, "Stratocumulus Cloud Field Reflected Fluxes: The Effect of Cloud Shape," *J. Atmos. Sci.*, **41**, p. 3085-3103, 1984.

Weiss, R. A., and R. K. Scoggins, "Light and Shadow Effects in Rough Terrain," *Proceedings of the Seventh Annual EOSAEL/TWI Conference*, p. 363-380, Las Cruces, NM, 1987.

Wetmore, A. E., and A. Zardecki, "The Boundary Layer Illumination and Radiative Balance Model (BLIRB)," *Proceedings of CIDOS-93*, p. 201-206, Ft. Belvior, VA, 1993.

Wiscombe, W. J., "The delta-M method: rapid yet accurate radiative flux calculations for strongly asymmetric phase functions," *J. Atmos. Sci.*, **34**, p. 1408-1422, 1977.

Zardecki, A., S. A. W. Gerstl, and J. F. Embury, "Application of the 2-D discrete-ordinates method to multiple scattering of laser radiation," *Appl. Opt.*, **22**, p. 1346-1353, 1983.

Zardecki, A., S. A. W. Gerstl, and R. E. DeKinder, "Two- and three-dimensional radiative transfer in the diffusion approximation," *Appl. Opt.*, **25**, p. 3508-3515, 1986.

Zardecki, A., and R. Davis, *Boundary Layer Illumination Radiation Balance Model: BLIRB*, Technical Report 6211, STC, Hampton, VA, 1991.

Zardecki, A., "Modification and Evaluation of the Weather and Atmospheric Visualization Effects for Simulation (WAVES) Suite of Codes," Interim Report, *Los Alamos Consulting*, 137 Monte Rey Dr., Los Alamos, NM 87544, 1995.

Acronyms and Abbreviations

1D	One-dimensional
3D	Three-dimensional
AIM	Atmospheric Illumination Module
ASL	U.S. Army Atmospheric Sciences Laboratory
AFGL	U.S. Air Force Geophysics Laboratory
ARL	U.S. Army Research Laboratory
AGAUS	August Miller's Mie Scattering Code
AGSNOW	Special version of AGAUS for treating SNOW cases
BLIRB	Boundary Layer Illumination and Radiance Balance model
BLITS	Boundary Layer Illumination and Transmission Simulation
BRDF	Bi-directional Reflectance Distribution Function
CSSM	Air Force's Cloud Scene Simulation Model
DISORT	DIScrete Ordinates Radiative Transfer routine
DOM	Discrete Ordinate Method
DOMRT	Discrete Ordinate Method approach to Radiative Transfer
DMSO	Defense Modeling and Simulation Office
DoD	Department of Defense
E^2DIS	Environmental Effects for Distributed Interactive Simulations
EOSAEL	Electro-Optical Systems Atmospheric Effects Library
EOSAEL92	1992 Release of EOSAEL
FE	Finite Element Technique within DOM
HGPF	Henyey-Greenstein Phase Function
IHMC	In-House Monte Carlo
IID	Independent Identically Distributed
LLS	Log Least Squares
LOS	Line of Sight
M&C	McKee and Cox
MODTRAN	Air Force Moderate Resolution RT Model
RMS	Root Mean Square
RMSE	Root Mean Square Error
RT	Radiative Transfer
RVs	Random Variables
SAA	Small Angle Approximation
WAVES	Weather and Atmospheric Visualization Effects for Simulations

Appendix A
The Scaling Transformation

In this appendix, we describe the approach used to make a scaling transformation on the form of the phase function used in the radiative transfer (RT) code. This transform modifies the coefficients used to describe the extinction, single scattering albedo, and Legendre polynomial expansion coefficients of a phase function, in the process removing the effects of the aerosol forward scattering peak from the radiative transfer equation.

These modifications are necessary because phase functions often have forward peak values on the order of hundreds or thousands. It is impossible to adequately simulate these peaks with low order Legendre expansions. Thus, it is a common practice to model the forward peak region with a δ phase function. By introducing this approximation, some of the energy is treated as unscattered.

The method developed here consists of a log-least-squares (LLS) approach to evaluate the forward scatter fraction (f) and an empirical model for modifying the Legendre expansion coefficients, c_ℓ. The LLS approach models the phase function's forward peak using a Gaussian phase function adding to the low order Legendre expansion used to characterize the remainder of the angular dependence.

In developing the empirical form for the c_ℓ, we consider several forms for the least squares approach. It is shown that the δ-M solution for the c_ℓ, as a function of f and the Legendre expansion coefficients of the phase function derives, from a standard least squares analysis. We then show the similarity between actual phase functions and the Henyey-Greenstein single-parameter phase function. This similarity is used to argue that a further correction is needed to the c_ℓ equation, leading to the empirical form. The results of using this technique have previously been shown in figures 17 through 20 in chapter 3, which reveal that we are able to outperform the δ-M technique in most cases.

A.1 Background

As described in the main contents of this report, the discrete-ordinates approach to solving the radiative transfer equation is a valuable tool in studying scattering in three-dimensional media. A main feature of this technique involves representing phase function scattering in a way that is compatible with the discrete ordinates methods. To accomplish this representation we first produces estimates of the scattering phase functions of various natural aerosols. Tofsted *et al.* (1997) generated a series of such functions for near surface haze and precipitation aerosols based on the Mie scattering algorithm developed by Miller (1983), that incorporated the improved forward peak handling technique of Lentz (1976). Upper air cloud aerosols were also treated using the Khrgian-Mazin particle size distribution parameterizations adopted by Low and O'Brien (1987).

These phase functions must then be represented as Legendre expansions, and often for greater accuracy these expansions are modified according to the delta correction, also known as a scale transformation (Potter (1970), Joseph et al. (1976), Wiscombe (1977), Schaller (1979), McKellar and Box (1981), LeNoble (1985)). Techniques developed under these previous applications normally only considered 1D RT codes where large order stream models could be instituted. In these applications little consideration was given to ensuring that the phase function remained nonnegative at all scattering angles (with the exception of Fiveland (1984) when he limited the asymmetry parameter g to the range $0 \leq g \leq 1/3$ in his two-term expansion) because in most situations the scattering model order was high enough that it would automatically be nonnegative. Except for Fiveland, previous studies never even considered that the order of the stream model would be too low. But since our abilities are already being taxed due to CPU time, memory, spectral, spatial resolution, and spatial domain concerns, it only makes sense that we should have to implement our model under particularly stressful conditions. We therefore require a model which is more robust at low order expansions than has been available heretofore.

To avoid the problems of negative radiance calculations, the traditional delta correction approach has been revised. In the past, various empirical arguments were made for determining the value of the parameter f. Joseph et al. (1976) used $f = g^2$. Liou (1992) proposed using a constant f for a given scattering order. McKellar and Box (1981) recommended various functions of the Legendre coefficients. Most of these recommendations depend on the number of coefficients selected. Wiscombe (1977) set f to the next Legendre expansion coefficient beyond the range of coefficients modified in the expansion. But, in each of these cases, f is defined based on an empirical rule. In what follows we base f on a LLS analysis, but determine the c_ℓ expansion coefficients based on an empirical rule.

To help define the degree of success possible with this method we have selected one of the Shettle and Fenn (1979) advection fog aerosols as our sample case to model. This aerosol has a modified gamma particle size distribution with mode radius of $r_0 =$ 10 μm and α and γ parameters of 1 and 6, respectively. The scattering properties of this phase function at different wavelengths are modeled using a Mie scattering code.

A.2 Phase Function Representation

As in the main section, the phase function $P(\mu)$ is represented as a function of the cosine of the scattering angle (μ) only. This presupposes that the aerosol droplets are either spherical in shape or exhibit random orientation. $P(\mu)$ is normalized according to

$$\int\limits_0^{2\pi} d\phi \int\limits_0^\pi P[\cos(\theta)]\, \sin(\theta) d\theta = 2\pi \int\limits_{-1}^1 P(\mu)\, d\mu = 1. \qquad (A.1)$$

This phase function can be exactly represented by an infinite Legendre series,

$$P(\mu) = \sum_{\ell=0}^{\infty} \alpha_\ell \, X_\ell \, P_\ell(\mu), \quad X_\ell = 2\pi \int_{-1}^{1} P(\mu) \, P_\ell(\mu) \, d\mu, \quad \alpha_\ell = \frac{2\ell+1}{4\pi}, \quad (A.2)$$

where $P_\ell(\mu)$ is the Legendre polynomial of order ℓ. Unfortunately we do not have an infinite number of streams by which to characterize the scattering effects, so we must find some suitable way to truncate this expansion.

Under the delta correction approach (Joseph et al. (1976), Wiscombe (1977)), the phase function is normally approximated by a δ function in the forward direction and a Legendre expansion of order L,

$$P_E(\mu) = f \, \frac{\delta(\mu-1)}{2\pi} + (1-f) \sum_{\ell=0}^{L} \alpha_\ell \, c_\ell \, P_\ell(\mu). \quad (A.3)$$

Here the δ is divided by 2π after van de Hulst (1980b), which assumes the full peak falls within the integral bounds.

Under the classic δ-M approach (Wiscombe 1977), one assumes $f = X_{L+1}$. Since the Legendre expansion of $\delta(\mu-1)/(2\pi)$ has coefficients $X_\ell = 1$, for all ℓ, if one equates the first $L+2$ terms of the Legendre expansion of $P(\mu)$, in Eq. (A.2), to those of $P_E(\mu)$, in Eq. (A.3), one obtains the equations,

$$\alpha_\ell \, X_\ell = \alpha_\ell \, f \times 1 + \alpha_\ell \, (1-f) c_\ell, \qquad \ell = 0, ..., L+1, \quad (A.4)$$

whence,

$$c_\ell = \frac{X_\ell - f}{1 - f}, \qquad \ell = 0, ..., L+1. \quad (A.5)$$

Of course, since $X_0 \equiv 1$ by definition, we will always have $c_0 \equiv 1$. And, as noted, since under the δ-M approach $f = X_{L+1}$, $c_{L+1} = 0$. This expansion is thus purported to apply to an order $L+1$ expansion, although one only retains terms out to L.

Using the model of $P_E(\mu)$ above, we can determine its effect on the overall equation of transfer. Let us rewrite the equation of transfer using the phase function estimate, as

$$\hat{\Omega} \cdot \nabla I(\vec{r}, \hat{\Omega}) + \sigma \, I(\vec{r}, \hat{\Omega}) = \sigma \varpi \int_{4\pi} I(\vec{r}, \hat{\Omega}') \, P_E(\hat{\Omega} \cdot \hat{\Omega}') \, \hat{\Omega}' + \sigma \, B(\vec{r}, \lambda). \quad (A.6)$$

Due to the δ function in $P_E(\mu)$, the original scattering source term can be written as,

$$J(\hat{\Omega}, \vec{r}) = f \, \sigma \varpi \, I(\vec{r}, \hat{\Omega}) + (1-f) \, \sigma \varpi \int_{4\pi} I(\vec{r}, \hat{\Omega}') \, P'(\hat{\Omega} \cdot \hat{\Omega}') \, \hat{\Omega}', \qquad (A.7)$$

where $P'(\mu)$ is the modified Legendre expansion:

$$P'(\mu) = \sum_{\ell=0}^{L} \alpha_\ell \, c_\ell \, P_\ell(\mu). \qquad (A.8)$$

The RT equation can then be rewritten as,

$$\hat{\Omega} \cdot \nabla I(\vec{r}, \hat{\Omega}) + \sigma' \, I(\vec{r}, \hat{\Omega}) = \sigma' \varpi' \int_{4\pi} I(\vec{r}, \hat{\Omega}') \, P'(\hat{\Omega} \cdot \hat{\Omega}') \, \hat{\Omega}' + \sigma' \, B', \qquad (A.9)$$

which has the same form as the original equation of transfer, except that we have introduced the variables

$$\sigma' = \sigma \, (1 - f \, \varpi), \qquad (A.10)$$

$$\varpi' = \frac{(1 - f) \, \varpi}{(1 - f \, \varpi)}, \qquad (A.11)$$

and

$$B' = (1 - \varpi')b, \qquad (A.12)$$

where we note that $\sigma'(1 - \varpi') = \sigma(1 - \varpi)$ such that the emittance term is unaffected by this transformation.

This new equation simulates the forward scattered radiation not by directly calculating the results, but rather by treating forward scattered energy as unscattered. That is, the angular resolution achieved by using a smaller number of streams is insufficient to resolve the difference between forward scattered and unscattered radiation. The resulting transfer equation must be treated as an equivalent result, but it can never be related directly back to the original problem, because we have removed any distinctions between forward scattered and unscattered energy. Beyond this distinction, the new problem conserves energy in the same degree as the original problem.

A.3 Least Squares Derivation

In this section, we consider alternate methods for evaluating f and c_ℓ based on a least squares approach. We can then compare results obtained using this new approach with the $f = X_{L+1}$ approach proposed by Wiscombe (1977). Let us begin by defining a least squares metric,

$$Z^2 = 2\pi \int_{-1}^{1} \{P(\mu) - P_E(\mu)\}^2 \, d\mu. \qquad (A.13)$$

Using this form of a least squares equation requires that all arguments of $P_E(\mu)$ be square integrable. Obviously, the δ component is not, so it will need to be

replaced by a function which operates nearly like a delta function. That is, with respect to the component Legendre polynomials, it will have to act with sifting properties almost like a δ function. As a simple mathematical device, in this analysis, the δ is approximated by a Gaussian form

$$\delta(\mu - 1)/2\pi \approx \frac{N(\varrho)}{2\pi \varrho^2} \exp(-\theta^2/2\varrho^2), \tag{A.14}$$

where

$$N^{-1}(\varrho) = \varrho^{-2} \int\limits_0^\pi \exp(-\theta^2/2\varrho^2)\sin(\theta)d\theta. \tag{A.15}$$

$N(\varrho)$ is a normalization term accounting for the fact that, while we expect the angular width of the distribution about the zero peak (ϱ) to be narrow, we are nonetheless integrating over a unit sphere (not over a planar surface) such that $N(\varrho)$ must be slightly greater than unity to compensate. By this approximation of a δ phase function, we are saying that its width is small with respect to the width of the Legendre components in the expansion. In order to ensure this feature, we restrict ϱ to values below some maximum, R, which we have arbitrarily set at 0.15 radians.

Using this approximation for the δ peak, Z^2 can be written as a series of six terms: $Z^2 = \sum_{i=0}^5 C_i$, which represent the squaring of the original phase function, the δ term, and the Legendre terms with themselves, and cross-terms between these 3 basic types of terms. Of course, the Legendre terms of different indices are orthogonal and integrate to zero. After some manipulation, we obtain the following results:

$$C_0 = 2\pi \int\limits_{-1}^1 P^2(\mu)\,d\mu, \qquad C_1 = -2fN(\varrho)\,Q_P(\varrho), \tag{A.16}$$

$$C_2 = -2(1-f)\sum_{\ell=0}^L \alpha_\ell\,c_\ell\,X_\ell, \qquad C_3 = f^2 N^2(\varrho)Q_\delta(\varrho), \tag{A.17}$$

$$C_4 = 2(1-f)f\,N(\varrho)\sum_{\ell=0}^L \alpha_\ell\,c_\ell\,Q_\ell(\varrho), \qquad C_5 = (1-f)^2\sum_{\ell=0}^L \alpha_\ell\,c_\ell^2, \tag{A.18}$$

where

$$Q_\ell(\varrho) = \int\limits_0^{\pi/\varrho} \exp(-u^2/2)\,P_\ell[\cos(\varrho u)]\,\frac{\sin(\varrho u)}{\varrho}du, \tag{A.19}$$

$$Q_P(\varrho) = \int\limits_0^{\pi/\varrho} \exp(-u^2/2)\,P[\cos(\varrho u)]\,\frac{\sin(\varrho u)}{\varrho}du, \tag{A.20}$$

111

$$Q_\delta(\varrho) = \frac{1}{2\pi\varrho^2} \int\limits_0^{\pi/\varrho} \exp(-u^2) \frac{\sin(\varrho u)}{\varrho} du. \tag{A.21}$$

Of these, terms C_0, C_3, and C_5 represent the squaring of the original phase function, the Gaussian peak, and the Legendre terms with themselves, respectively. C_1 represents the correlation between the Gaussian peak and the original phase function, C_2 represents the correlation between the Legendre terms and the original phase function, and C_4 represents the correlation between the Gaussian peak and the Legendre terms. Because ϱ is small compared to π, it will rarely be necessary to carry the Q integrations out over their complete range.

Z^2 is minimized by taking its derivative with respect to the individual variables. Setting $\partial Z^2/\partial c_\ell = 0$, one obtains results from the derivatives of the sum of components C_2, C_4 and C_5. Dividing by the common factor $2(1-f)\alpha_\ell$ and solving for c_ℓ, one obtains,

$$c_\ell = \frac{X_\ell - f\,N(\varrho)\,Q_\ell(\varrho)}{1-f}. \tag{A.22}$$

Notice that $Q_0(\varrho) = N^{-1}(\varrho)$, so as expected the c_0 term, which carries all the energy continues to evaluate to unity.

In the limit as $\varrho \to 0$, N and the Q_ℓ both approach unity and the same equation is obtained for c_ℓ as was obtained by the δ-M method [Eq. (A.5)]. This confirms that a basic least squares approach is similar to the δ-M method. But, this method also provides information about f and ϱ, while δ-M only provided an empirical formula for f.

We thus continue by substituting the expression for c_ℓ in the equation for Z^2 to yield,

$$Z^2 = C_0 - 2f\,N(\varrho)\,Q_P(\varrho) + f^2 N^2(\varrho)\,Q_\delta(\varrho) - \sum_{\ell=0}^{L} \alpha_\ell \left\{ X_\ell - f\,N(\varrho)\,Q_\ell(\varrho) \right\}^2. \tag{A.23}$$

Taking $\partial Z^2/\partial f = 0$ yields,

$$f\,N(\varrho) = \frac{S_n(\varrho)}{S_d(\varrho)} = \frac{Q_P(\varrho) - \sum\limits_{\ell=0}^{L} \alpha_\ell X_\ell Q_\ell(\varrho)}{Q_\delta(\varrho) - \sum\limits_{\ell=0}^{L} \alpha_\ell Q_\ell^2(\varrho)}, \tag{A.24}$$

where S_n and S_d are numerator and denominator quantities, respectively. Introducing this new form once again to the Z^2 equation, one obtains,

$$Z^2 = C_0 - K_0 - \frac{S_n^2(\varrho)}{S_d(\varrho)}, \qquad K_0 = \sum_{\ell=0}^{L} \alpha_\ell X_\ell^2, \tag{A.25}$$

where we note that both C_0 and K_0 are constants with respect to the phase function parameter ϱ. Z^2 can thus be minimized by varying ϱ alone.

Note that we require $S_n(0) = P(1) - \sum \alpha_\ell X_\ell > 0$ for the method to predict any forward peak at all. Otherwise, f is set to zero and $c_\ell = X_\ell$. For phase functions which pass the first criterion, ϱ can be determined, followed by f, and finally the c_ℓ's.

To see the properties of a typical phase function when characterized by the parameters f and ϱ, we evaluated the test particle size distribution at different wavelengths and have plotted various functions of the results combined with the mode radius property of the size distribution, the single scattering albedo ϖ, and the wavelength λ, in figure A.1.

As expected, we found that the ratio of ϱ to λ/r_0 is roughly constant, indicating that the forward peak represents a diffraction effect. And second, the fraction f of energy in the forward peak is related to ϖ, because ϖ is only reduced due to energy absorbed within the particles. As more energy is absorbed inside, ϖ decreases. But, at the same time, f increases as the amount of diffracted energy remains the same, but increases as a proportion of the total scattering.
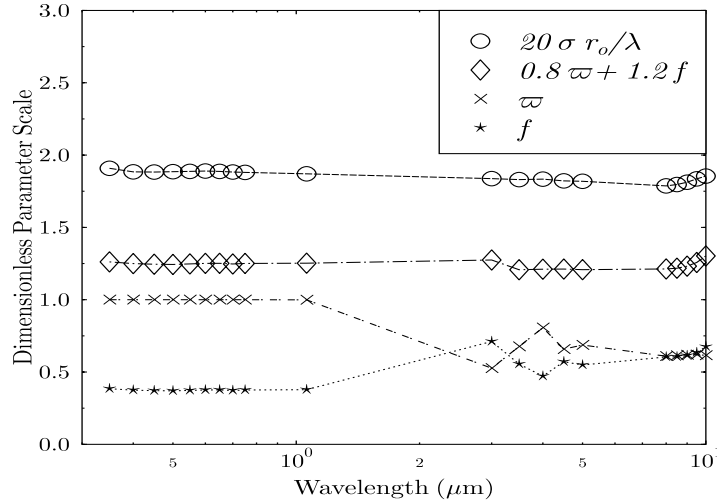
Figure A.1.   Comparison of forward scattering parameters ϱ and f and propagation parameters ϖ, r_0 and λ.

This analysis gave us considerable confidence in the least squares approach in that (1) it was able to characterize properties of the forward peak region that are consistent with theory of scattering, and (2) that it produced calculation equations for the c_ℓ that correspond to previous theory. However, there is a

deficiency in this approach due to its failure to produce positive definite phase functions for low order expansions. A sample case is shown in figure A.2, in which the predicted least squares curve for $L = 2$ resulting from an optimal $f = 0.54$, produced a wide negative phase function estimate region from $\pi/2$ to $3\pi/4$. The need for a nonnegative requirement was shown with respect to the scattering results presented in the Monte Carlo chapter of the main text. We must still look for some representative value of f which avoids negative values.
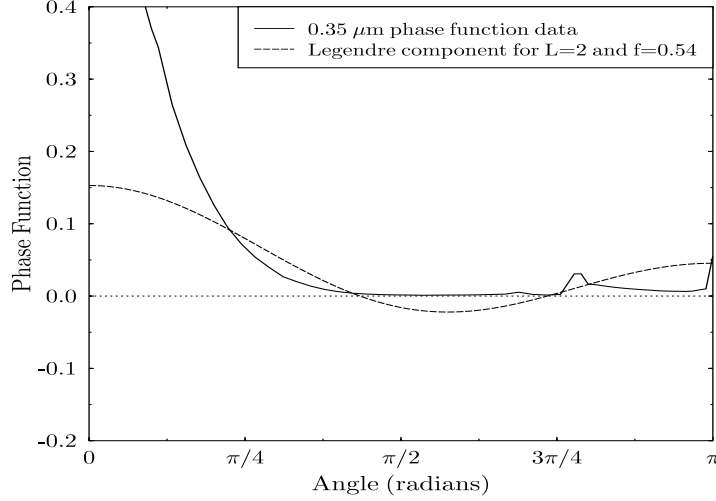
Figure A.2. Results of preliminary least squares approach produce negative phase function estimates at scattering angles between $\pi/2$ and $3\pi/4$.

We chose to work with the $L = 2$ (8-stream) case, since it can be solved in a closed form. The Legendre expansion for this case is

$$P'(\mu) = (4\pi)^{-1}[1 + 3c_1\mu + 5c_2(3\mu^2 - 1)/2], \qquad (A.26)$$

which is a quadratic equation in the scattering cosine μ. We can thus solve for values of μ which produce $P'(\mu) = 0$, as

$$\mu_{0\pm} = -\frac{c_1}{5c_2} \pm \left(\frac{1}{3} + \frac{c_1^2}{25c_2^2} - \frac{2}{15c_2}\right)^{1/2}. \qquad (A.27)$$

The requirement to avoid phase function zeros is:

$$3c_1^2 + (5c_2 - 1)^2 < 1. \qquad (A.28)$$

114

If we then introduce the δ-M form for the c_ℓ, we find that valid f values will lie in a range Δf about a mean value $\bar{f}$, defined as,

$$\bar{f} = \frac{3X_1 + 20X_2 - 5}{18}, \qquad\qquad (A.29)$$

$$\Delta f = \frac{[25 + 15X_1(8X_2 - 3X_1 - 2) - 10X_2(5X_2 + 2)]^{1/2}}{18}. \qquad (A.30)$$

The sample fog phase function data were analyzed on the basis of Eqs. (A.29) and (A.30) and plotted in figure A.3. This figure reveals a section around 10 μm where only the mean value is plotted because Δf has become imaginary over this range. This indicates that there is no valid range of f about the mean for which the phase function remains nonnegative.
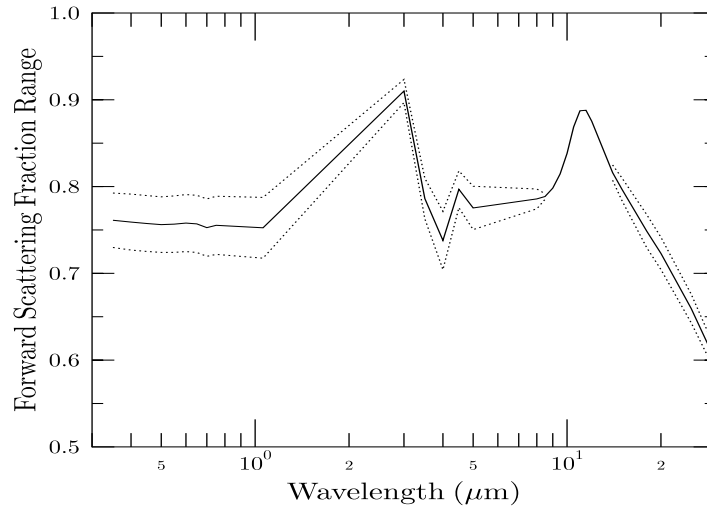
Figure A.3. Evaluated range of f values (maximum, minimum, and mean) for which phase function remains nonnegative.

We are thus led to the conclusion that the traditional equation for evaluating the c_ℓ's was insufficient to maintain a positive definite status. Since this equation is based on a standard least squares analysis, doubt is thus placed on this method. An analysis of this method and the nature of standard phase functions reveals where the problem arises: the least squares is attempting to match the value of a function which exhibits a *very* high peak at $\mu = 1$ and very small values over the rest of its range. But, since the least squares approach merely attempts to minimize the distance of the estimate to the curve, the large values in the peak region will receive maximum attention, and there is no penalty for 'crossing the line' into negative phase function values at large scattering angles.

To solve this situation we can use a LLS optimization:

$$\underline{Z}^2 = 2\pi \int\limits_{-1}^{1} d\mu \, \left\{ \ln'[P(\mu)] - \ln'[P_E(\mu)] \right\}^2, \qquad (A.31)$$

where

$$\ln'(x) = \begin{cases} \ln(x), & x > P_{min} \\ \ln(P_{min}) + 10^6 (x - P_{min}), & x \le P_{min} \end{cases}, \qquad (A.32)$$

where P_{min} is chosen at some level below the minimum value of the tabulated phase function data. For example, $P_{min} = \min(P(\mu))/10$. Since most phase functions have minima in the range 10^{-2}-10^{-3}, a P_{min} around 10^{-4} should be sufficient to result in only the natural log function being accessed near the end of the optimization process, but avoid evaluating negative arguments during the intermediate stages.

To be compatible with the DOM we must still describe our phase function estimate using Eq. A.3 since using a LLS approach leads to the complications. But then, it becomes impossible to analyze the least squares equation to produce analytical solutions for the different coefficients. Without these analytical equations we end up with a multidimensional search over the c_ℓ which could produce local minima making the search process very difficult and time consuming. Considering this complication, the Henyey-Greenstein phase function (HGPF) model was considered as a model in guiding the development of an empirical method of determining the c_ℓ values while simultaneously imposing a positive definite conditioning through the use of the LLS equation.

A.4 The Henyey-Greenstein Phase Function

The Henyey-Greenstein model for the phase function is well known and has been adopted by several authors (LeNoble (1985), van de Hulst (1980), Liou (1980)) who view it as a model of the typical behavior of aerosols, in spite of the fact that the HGPF has no backscatter peak when the asymmetry parameter is positive.

The use of HGPF is widespread because it has a relatively simple analytical form and because its expansion in terms of Legendre polynomials is particularly simple. The HGPF is written under our normalization scheme as,

$$P_{HG}(\mu) = \frac{1}{4\pi} \frac{(1 - g^2)}{(1 + g^2 - 2g\mu)^{3/2}}, \qquad (A.33)$$

where g is the asymmetry parameter, often set to the value of X_1, and varies between -1 and 1. Legendre coefficients of this distribution are

$$X_{HG,\ell} = g^\ell. \qquad (A.34)$$

Thus, at $g \equiv 1$ the HGPF is a δ phase function.
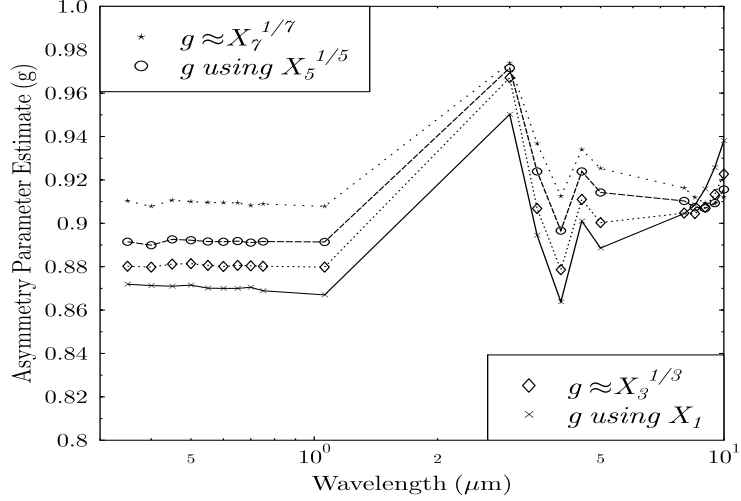
Figure A.4. Estimates of the g parameter based on the Henyey-Greenstein model. X_ℓ for $\ell = 1, 3, 5, 7$ were used to estimate g for the sample fog aerosol type.

Most aerosols exhibit X_ℓ values that can be approximated by some g value between 0.85 and 1.00, as illustrated in figure A.4. There, we used the X_ℓ to compute g estimates using the equation $g \approx X_\ell^{1/\ell}$. The resulting estimates seen in this figure show some dispersion yet reveal that the HGPF is a realistic model.

This resemblance between the HGPF and aerosol phase function coefficients is useful in providing some insights into problems encountered when finite expansions of this form are needed. We identify this truncated form using the function $\tilde{P}_{HG}(\mu)$,

$$P_{HG}(\mu) \approx \tilde{P}_{HG}(\mu) = \sum_{\ell=0}^{L} \alpha_\ell \, g^\ell \, P_\ell(\mu). \qquad (A.35)$$

The family of truncated HGPF functions behaves very differently from the full HGPF. For example, figure A.5 shows the behaviors of several approximations to a delta function for different even orders of expansion ($L = 2, 4, 6, 8$). From the figure we see a ringing behavior similar to the Gibbs phenomenon observed in Fourier series expansions around functional discontinuities. These are particularly severe when modeling a δ function, and since most aerosols exhibit highly forward scattering behaviors similar to δ's, we should expect ringing there as well.

To remove these artifacts and yet maintain the HGPF form, we find that we must reduce the g value down to some threshold maximum value that cannot be exceeded without producing a negative phase function. Figure A.6 shows plots
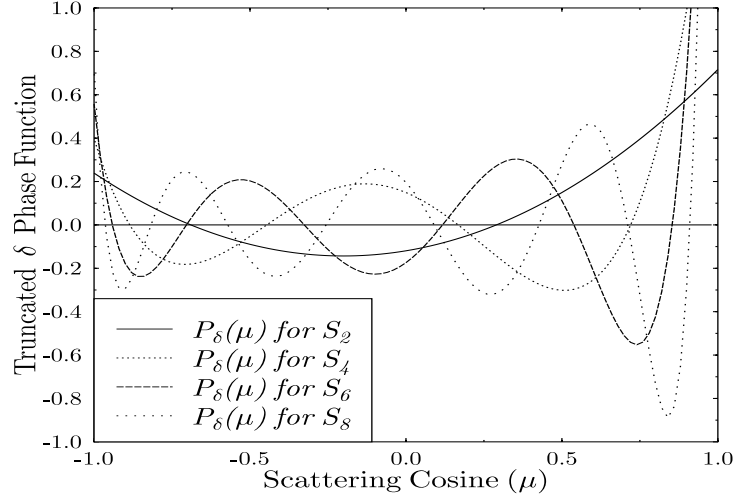
Figure A.5. Legendre expansion approximations to the δ phase function at different orders of expansion, showing zero crossings for orders $L = 2$, 4, 6, and 8.

of a few of these truncated HGPF forms at maximum g values. We have plotted these maximum g values out in figure A.7. In this same figure, we have also plotted out the results of a second investigation where we asked the question: What if we perform a δ-M correction on a truncated HGPF representation? This correction involves setting $f = g^{L+1}$, leading to,

$$c_\ell = \frac{g^\ell - g^{L+1}}{1 - g^{L+1}}.$$

This second curve indicates that when we impose a δ-M forward peak truncation, we increase the effective maximum g that can be treated within the model. But, comparing these new maxima with characteristic g values of a real aerosol (figure A.4) reveals that we cannot adequately characterize these aerosols at L values less than about 16 or 18 using the δ-M.

Since using an L of 16 or 18 would impose heavy memory burdens on the RT computations, some form for the c_ℓ computation was needed that provided a system similar to that originally developed, yet avoided the negative phase function problem. As an initial solution, it was observed that if one started with an HGPF characterized by a value g, then this value must be corrected downward to a value g_L, corresponding to the value of g for order L which is the maximum g parameter that produces a positive definite expansion at that order. To obtain this reduction, one would need to multiply expansion coefficient ℓ by a factor e^ℓ, where $e < 1$. But if we started with the expansion coefficients $c_\ell = (X_\ell - f)/(1 - f)$, these coefficients could be viewed as a series of values
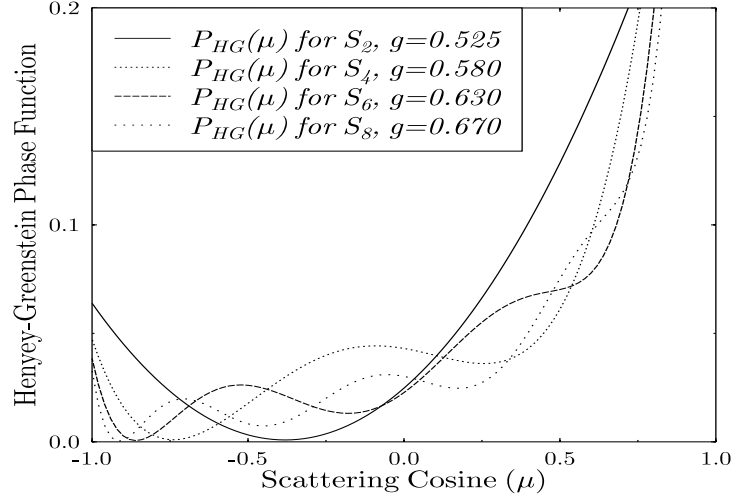
Figure A.6. Legendre expansion approximations to the maximum positive-definite HGPF's at different orders of expansion. Amplified region shows curves approach zero due to local minima closest to $\mu = -1$.
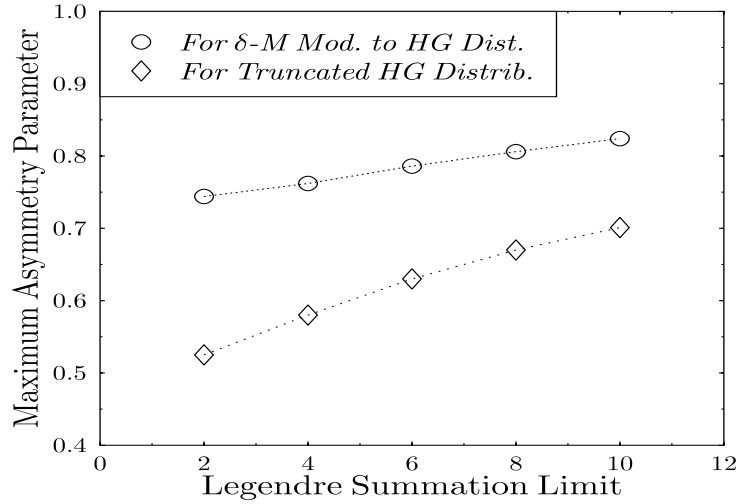
Figure A.7. Limiting maximum value allowable for g when imposing a positive definite condition on an order L Legendre approximation of the Henyey-Greenstein phase function, and when using the δ-M correction method.

which decrease *like* a Henyey-Greenstein set, which leads to the proposition of

119

a new empirical relationship for the c_ℓ of

$$c_\ell = \frac{[X_\ell - f\, N(\varrho)\, Q_\ell(\varrho)]}{[1 - f]}\, e^\ell. \qquad (A.36)$$

Here we have used the standard least squares results and augmented them by the appended e^ℓ factor. Since $X_0 = 1$ and $N(\varrho)\, Q_\ell(\varrho) = 1$, we still have $c_0 \equiv 1$, which conserves scattered energy.

To understand this solution somewhat better, consider the approximation that the δ-M is making: the goal under the δ-M is to exactly match the Legendre expansion coefficients from the original series expansion in the new expansion,

$$X_\ell = f\, \delta_\ell + (1 - f)\, c_\ell. \qquad (A.37)$$

Then, by using values for $\delta_\ell \equiv 1$, the standard equation is obtained for c_ℓ. In our method we have Eq. (36) for the c_ℓ's and wish to work backwards to compute the coefficients δ_ℓ:

$$X_\ell = f\, \delta_\ell + e^\ell\, [X_\ell - f\, N(\varrho)\, Q_\ell(\varrho)], \qquad (A.38)$$

which leads to,

$$\delta_\ell = \frac{X_\ell}{f}(1 - e^\ell) + N(\varrho)Q_\ell(\varrho)\, e^\ell. \qquad (A.39)$$

Obviously, Eq. (39) produces $\delta_\ell \equiv 1$ whenever $e \equiv 1$ and $\varrho \equiv 0$. And these two parameters approach these limiting values as the order L of the expansion increases. Thus, the δ-M technique can be seen to model the δ function using a truncated expansion of the exact δ function coefficients. Our method models the δ using optimized coefficients based on the order of the expansion. The difference is that the current solution uses coefficients that minimize the ringing behavior in the truncated series results.

We show the results of the LLS analysis in figures A.8 and A.9. In figure A.8, the optimal value of e and the resulting $Z_{\log}^2$ are plotted for an $L = 2$ case. Note that e is a maximum when the sum of squares is a minimum, indicating that there appears to be some sense in which the parameterization of e produces maximum values near the solution point, leading us to conclude that (1) the method is stable, and (2) the method attempts only to remove the negative effects rather than abnormally reducing the influence of higher Legendre terms.

In figure A.9, the expansion resulting from this choice of e-f pair is plotted for $L = 2$ and for a set of results for $L = 4$. In the $L = 4$ case, $f = 0.58$ and $e = 0.93$. As seen, the $L = 4$ expansion captures the forward hemisphere behavior better than the $L = 2$ expansion.
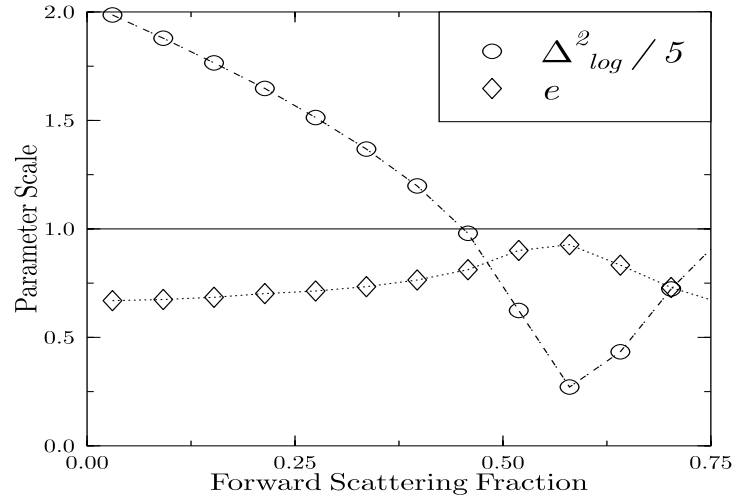
Figure A.8. The minimum error value of e is plotted along with the scaled squared error associated with that value as a function of the forward scatter fraction f.
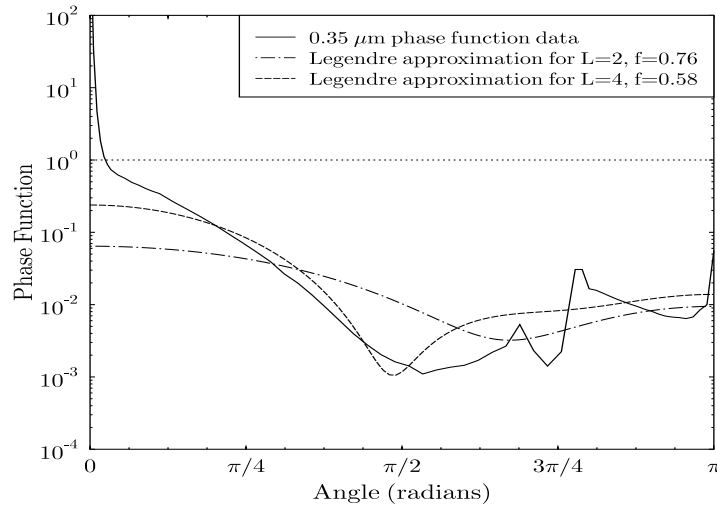
Figure A.9. Comparison of Legendre expansions for $L = 2$ and $L = 4$ using positive definite choices for f and e against calculated phase function data.

A.5 Conclusions

From figure A.3 it was shown that a simple rule of thumb for modifying the c_ℓ coefficients, based on the forward scattering fraction f alone, can lead to negative phase function evaluations at some angles. We thus introduced an empirical equation for c_ℓ that employed the modification by the factor e^ℓ. This new form attenuates higher order Legendre coefficients to ensure a positive-definite phase function and remove the forward peak.

The method developed here results in a much more robust means of obtaining an optimal approximate phase function including the forward scattering correction, while simultaneously avoiding the problems inherent with negative phase function predictions. Chapter 3 illustrated that these new techniques produce better flux predictions than the δ-M technique of Wiscombe.

In treating scattering problems, once an order of expansion has been chosen for a simulation, the phase function properties can be preprocessed to derive appropriate f, ϱ, and e values that lead to modifications to the extinction coefficient σ, the single scattering albedo ϖ and the modified Legendre coefficients c_ℓ that describe that aerosol.

Distribution

NASA MARSHAL SPACE FLT CTR   1
ATMOSPHERIC SCIENCES DIV
E501
ATTN DR FICHTL
HUNTSVILLE AL 35802

NASA SPACE FLT CTR   1
ATMOSPHERIC SCIENCES DIV
CODE ED 41 1
HUNTSVILLE AL 35812

ARMY STRAT DEFNS CMND   1
CSSD SL L
ATTN DR LILLY
PO BOX 1500
HUNTSVILLE AL 35807-3801

ARMY MISSILE CMND   1
AMSMI RD AC AD
ATTN DR PETERSON
REDSTONE ARSENAL AL 35898-5242

ARMY MISSILE CMND   1
AMSMI RD AS SS
ATTN MR H F ANDERSON
REDSTONE ARSENAL AL 35898-5253

ARMY MISSILE CMND   1
AMSMI RD AS SS
ATTN MR B WILLIAMS
REDSTONE ARSENAL AL 35898-5253

ARMY MISSILE CMND   1
AMSMI RD DE SE
ATTN MR GORDON LILL JR
REDSTONE ARSENAL AL 35898-5245

ARMY MISSILE CMND   1
REDSTONE SCI INFO CTR
AMSMI RD CS R DOC
REDSTONE ARSENAL AL 35898-5241

ARMY MISSILE CMND   1
AMSMI
REDSTONE ARSENAL AL 35898-5253

CMD (420000D(C0245))   1
ATTN DR A SHLANTA
NAVAIRWARCENWPNDIV
1 ADMIN CIR
CHINA LAKE CA 93555-6001

PACIFIC MISSILE TEST CTR   1
GEOPHYSICS DIV
ATTN CODE 3250
POINT MUGU CA 93042-5000

```
NAVAL OCEAN SYST CTR                                         1
CODE 54
ATTN DR RICHTER
SAN DIEGO CA 52152-5000


METEOROLOGIST IN CHARGE                                      1
KWAJALEIN MISSILE RANGE
PO BOX 67
APO SAN FRANCISCO CA 96555


DEPT OF COMMERCE CTR                                         1
MOUNTAIN ADMINISTRATION
SPPRT CTR LIBRARY R 51
325 S BROADWAY
BOULDER CO 80303


DR HANS J LIEBE                                              1
NTIA ITS S 3
325 S BROADWAY
BOULDER CO 80303


NCAR LIBRARY SERIALS                                         1
NATL CTR FOR ATMOS RSCH
PO BOX 3000
BOULDER CO 80307-3000


DEPT OF COMMERCE CTR                                         1
325 S BROADWAY
BOULDER CO 80303


DAMI POI                                                     1
WASHINGTON DC 20310-1067


MIL ASST FOR ENV SCI OFC                                     1
OF THE UNDERSEC OF DEFNS
FOR RSCH & ENGR R&AT E LS
PENTAGON ROOM 3D129
WASHINGTON DC 20301-3080


ARMY INFANTRY                                                1
ATSH CD CS OR
ATTN DR E DUTOIT
FT BENNING GA 30905-5090


AIR WEATHER SERVICE                                          1
TECH LIBRARY FL4414 3
SCOTT AFB IL 62225-5458


USAFETAC DNE                                                 1
ATTN MR GLAUBER
SCOTT AFB IL 62225-5008


HQ AWS DOO 1                                                 1
SCOTT AFB IL 62225-5008


PHILLIPS LABORATORY                                          1
PL LYP
ATTN MR CHISHOLM
HANSCOM AFB MA 01731-5000
```

124

```
ATMOSPHERIC SCI DIV                                              1
GEOPHYISCS DIRCTRT
PHILLIPS LABORATORY
HANSCOM AFB MA 01731-5000


PHILLIPS LABORATORY                                             1
PL LYP 3
HANSCOM AFB MA 01731-5000


ARMY MATERIEL SYST                                             1
ANALYSIS ACTIVITY
AMXSY
ATTN MR H COHEN
APG MD 21005-5071


ARMY MATERIEL SYST                                             1
ANALYSIS ACTIVITY
AMXSY AT
ATTN MR CAMPBELL
APG MD 21005-5071


ARMY MATERIEL SYST                                             1
ANALYSIS ACTIVITY
AMXSY CR
ATTN MR MARCHET
APG MD 21005-5071


ARL CHEMICAL BIOLOGY                                          1
NUC EFFECTS DIV
AMSRL SL CO
APG MD 21010-5423


ARMY MATERIEL SYST                                            1
ANALYSIS ACTIVITY
AMSXY
APG MD 21005-5071


ARMY RESEARCH LABORATORY                                     1
AMSRL D
2800 POWDER MILL ROAD
ADELPHI MD 20783-1145


ARMY RESEARCH LABORATORY                                     1
AMSRL OP SD TP
TECHNICAL PUBLISHING
2800 POWDER MILL ROAD
ADELPHI MD 20783-1145


ARMY RESEARCH LABORATORY                                     1
AMSRL OP CI SD TL
2800 POWDER MILL ROAD
ADELPHI MD 20783-1145


ARMY RESEARCH LABORATORY                                     1
AMSRL SS SH
ATTN DR SZTANKAY
2800 POWDER MILL ROAD
ADELPHI MD 20783-1145
```

ARMY RESEARCH LABORATORY   1
AMSRL
2800 POWDER MILL ROAD
ADELPHI MD 20783-1145

NATIONAL SECURITY AGCY W21   1
ATTN DR LONGBOTHUM
9800 SAVAGE ROAD
FT GEORGE G MEADE MD 20755-6000

ARMY RSRC OFC   1
ATTN AMXRO GS (DR BACH)
PO BOX 12211
RTP NC 27009

DR JERRY DAVIS   1
NCSU
PO BOX 8208
RALEIGH NC 27650-8208

US ARMY CECRL   1
CECRL GP
ATTN DR DETSCH
HANOVER NH 03755-1290

ARMY ARDEC   1
SMCAR IMI I BLDG 59
DOVER NJ 07806-5000

ARMY COMMUNICATIONS   1
ELECTR CTR FOR EW RSTA
AMSEL EW D
FT MONMOUTH NJ 07703-5303

ARMY COMMUNICATIONS   1
ELECTR CTR FOR EW RSTA
AMSEL EW MD
FT MONMOUTH NJ 07703-5303

ARMY DUGWAY PROVING GRD   1
STEDP MT DA L 3
DUGWAY UT 84022-5000

ARMY DUGWAY PROVING GRD   1
STEDP MT M
ATTN MR BOWERS
DUGWAY UT 84022-5000

PL WE   1
KIRTLAND AFB NM 87118-6008

USAF ROME LAB TECH   1
CORRIDOR W STE 262 RL SUL
26 ELECTR PKWY BLD 106
GRIFFISS AFB NY 13441-4514

AFMC DOW   1
WRIGHT PATTERSON AFB OH 45433-5000

ARMY FIELD ARTILLERY SCHOOL   1
ATSF TSM TA
FT SILL OK 73503-5600

NAVAL AIR DEV CTR   1
CODE 5012
ATTN AL SALIK
WARMINISTER PA 18974

ARMY FOREIGN SCI TECH CTR   1
CM
220 7TH STREET NE
CHARLOTTESVILLE VA 22448-5000

NAVAL SURFACE WEAPONS CTR   1
CODE G63
DAHLGREN VA 22448-5000

ARMY OEC   1
CSTE EFS
PARK CENTER IV
4501 FORD AVE
ALEXANDRIA VA 22302-1458

ARMY CORPS OF ENGRS   1
ENGR TOPOGRAPHICS LAB
ETL GS LB
FT BELVOIR VA 22060

ARMY TOPO ENGR CTR   1
CETEC ZC 1
FT BELVOIR VA 22060-5546

SCIENCE AND TECHNOLOGY CORP   1
101 RESEARCH DRIVE
HAMPTON VA 23666-1340

ARMY NUCLEAR CML AGCY   1
MONA ZB BLDG 2073
SPRINGFIELD VA 22150-3198

USATRADOC   1
ATCD FA
FT MONROE VA 23651-5170

ARMY TRADOC ANALYSIS CTR   1
ATRC WSS R
WSMR NM 88002-5502

ARMY RESEARCH LABORATORY   1
AMSRL IS EW
BATTLEFIELD ENVIR DIV
WSMR NM 88002-5501

ARMY RESEARCH LABORATORY   1
AMSRL IS ES
BATTLEFIELD ENVIR DIV
ADELPHI MD 20783-1145

DTIC   1
8725 JOHN J KINGMAN RD
STE 0944
FT BELVOIR VA 22060-6218

ARMY MISSILE CMND   1
AMSMI
REDSTONE ARSENAL AL 35898-5243

ARMY DUGWAY PROVING GRD   1
STEDP3
DUGWAY UT 84022-5000

USTRADOC   1
ATCD FA
FT MONROE VA 23651-5170

WSMR TECH LIBRARY BR   1
STEWS IM IT
WSMR NM 88002

US MILITARY ACADEMY   1
MATHEMATICAL SCI CTR EXCELLENCE
DEPT OF MATHEMATICAL SCIENCES
ATTN MDN A (MAJ DON ENGEN)
THAYER HALL
WEST POINT NY 10996-1786

ARMY RESEARCH LABORATORY   15
ATTN D TOFSTED
AMSRL IS EW
BATTLEFIELD ENVIR DIV
WSMR NM 88002-5501

Record Copy   1

TOTAL   83